An Investigation of Unsteady Aerodynamic Multi-axis State-Space Formulations as a Tool for Wing Rock Representation

Pedro Jose de Oliveira Neto

Dissertation submitted to the Faculty of the Virginia Polytechnic Institute and State University in partial fulfillment of the requirements for the degree of

Doctor of Philosophy

In

Aerospace Engineering

Dr. William H. Mason, Advisor, Chair

Dr. Eugene M. Cliff

Dr. Wayne C. Durham

Dr. Christopher D. Hall

Dr. Craig Woolsey

August 2007

Blacksburg, Virginia

Keywords: High Angle of Attack, Nonlinear Dynamics, Stability Derivatives, Unsteady Aerodynamics, Wing Rock

An Investigation of Unsteady Aerodynamic Multi-axis State-Space Formulations as a Tool for Wing Rock Representation

By

Pedro J. de Oliveira Neto

Committee Chairman: Dr. William H. Mason

Aerospace Engineering

(ABSTRACT)

The objective of the present research is to investigate unsteady aerodynamic models with state equation representations that are valid up to the high angle of attack regime with the purpose of evaluating them as computationally affordable models that can be used in conjunction with the equations of motion to simulate wing rock. The unsteady aerodynamic models with state equation representations investigated are functional approaches to modeling aerodynamic phenomena, not directly derived from the physical principles of the problem. They are thought to have advantages with respect to the physical modeling methods mainly because of the lower computational cost involved in the calculations. The unsteady aerodynamic multi-axis models with state equation representations investigated in this report assume the decomposition of the airplane into lifting surfaces or panels that have their particular aerodynamic force coefficients modeled as dynamic state-space models. These coefficients are summed up to find the total aircraft force coefficients. The products of the panel force coefficients and their moment arms with reference to a given axis are summed up to find the global aircraft moment coefficients. Two proposed variations of the state space representation of the basic unsteady aerodynamic model are identified using experimental aerodynamic data available in the open literature for slender delta wings, and tested in order to investigate their ability to represent the wing rock phenomenon. The identifications for the second proposed formulation are found to match the experimental data well. The simulations revealed that even though it was constructed with scarce data, the model presented the expected qualitative behavior and that the concept is able to simulate wing rock.

Acknowledgments

All that I struggled to accomplish in my academic life was also part of a tentative effort to honor all of my former teachers. The first of them was my retired uncle Dermeval, who taught me how to read by patiently reading comics for me. Among the others, I would like to mention the devoted Chemistry Professor Adauto de Oliveira, my father, who was the first person to bring the beauty of Science to my attention. Another person that I should mention my gratitude to is schoolteacher Laudelina, my mother, who took her own life as an example and taught me to persevere and never give up, no matter how adverse the situation could be.

The times that I spent working on this research certainly are among the most challenging of my life in many ways. During these tough times of my Ph.D. program, I certainly received support from God, Who helped me through several individuals. Very important support came from the remaining members of my family, especially from Aurea, the two Estellas, Maria, and Priscila. They helped me in so many ways that it is impossible to list everything here. I would like at least to thank them for always keeping my positive attitude toward the end of this program. Fundamental support gave me the late Dr. Frederick Lutze, my first advisor in this research. He introduced me to this problem and gave me the initial guidelines to solve it. He also provided the grant that funded most of my stay in Blacksburg and made it possible for me to pursue the Ph.D. program. Very important guidelines were also given to me by my committee Chair, Dr. William Mason, who kindly lent me his multidisciplinary experience and advised me since Dr. Lutze passed away. I would like to thank all the committee members for the revision of this dissertation and valuable suggestions. I shall acknowledge the excellent job that the Graduate Program Coordinator in the Aerospace and Ocean Engineering Department, Ms. Hannah Swiger, did when she put everything together for my final examination. My stays in Blacksburg were possible also because of the leaves of absence granted by my employer, the Brazilian Air Force's Institute of Aeronautics and Space (IAE), after the

kind intercessions of Lt. Col. Paulo Garcia Soares, and of Col. Olympio Achilles de Faria Mello, Ph.D., to whom I am also indebted. Dr. Mello also helped me to get the grant that funded the last part of this research. This grant came from the Brazilian research agency FUNCATE, and from the IAE.

To all my teachers.

Contents

List of Figures

List of Symbols

Latin Alphabet

a_i, b_i, c_i	coefficients of the quadratic polynomials that represent the stability derivatives in function of the internal state variables.
b	wing span.
C_N	normal force coefficient.
C_l	rolling moment coefficient
$C_{L\max}$	maximum lift coefficient
D	switching function for the right hand side of the internal state equations. It assumes value 0 when the airplane motion variable is going up, and 1 when is going down. It also stands for drag force.
I_{xx}, I_{yy}, I_{zz}	airplane moments of inertia with respect to the body axes
I_{xy}, I_{xz}, I_{yz}	airplane products of inertia with respect to the body axes
L, M, N	components of the airplane aerodynamic resulting moment along body axes. L also stands for lift force.
p, q, r	components of the airplane angular velocity vector along body axes.
$\bar{q}$, q_∞	dynamic pressure of the undisturbed flowfield.
u, v, w	components of the airplane linear velocity vector along body axes.
U	switching function for the right hand side of the internal state equations. It assumes value 1 when the airplane motion variable is going up, 0 when is going down.
V, V_T	airspeed of the undisturbed flowfield.
X, Y, Z	components of the airplane aerodynamic resulting force along body axes.
$\bar{x}$	internal state variable that represents the non-dimensional distance from the trailing edge to either the position of the separation point or the position of the vortex breakdown, measured from the trailing edge and divided by the chord.

$\bar{x}_0(\alpha)$ static dependence function between the position of the point where the flow separates and the angle of attack.

$\bar{y}$ internal state variable related to the non-dimensional spanwise position of the leading edge vortex core.

$\bar{y}_0(\phi)$ function that represents the static dependence function between the spanwise position of the leading edge vortex core and the roll angle.

$\hat{t}$ convective time

Greek Alphabet

α angle of attack

α^* angle of attack value at which the separation reaches half of the chord, and used to position the logistic function that represents the static dependence of the separation point coordinate with the angle of attack.

β sideslip angle

θ pitch angle

$\bar{v}$ internal state variable related to both the vortex core vertical position and vortex strength.

$\bar{v}_0(\phi)$ function that represents the static dependence between the internal state variable $\bar{v}$ and the roll angle.

ϕ roll angle

ϕ^* roll angle value that gives the position of the logistic function that represents the static dependence of either the vortex core spanwise position or the combination of vertical position and vortex strength.

σ slope of the logistic function

τ_1 transient time of flow adjustment

τ_2 time-delay for flow adjustment

ξ airplane side of the lifting surface panel considered.

ψ head angle

List of Tables

1 Introduction

The atmospheric flight dynamics study of a vehicle is the study of the interaction of the equations of motion and the equations of the airflow around the vehicle. The equations of motion are given by Newton's laws and depend on the forces and moments acting on the vehicle. Among these forces are the aerodynamic ones that are functions of the airflow around the vehicle, which in turn depend on the previous motion history. The aerodynamic forces can be fully described by a set of nonlinear partial differential equations known as the Navier-Stokes equations. At the present time computational methodology and computer power are not adequate to provide time accurate solutions to the Navier-Stokes equations in the flight dynamics simulation environment. Even if the methodology existed, the cost of the computations would be very high. Recently, computational fluid dynamics methods based on Navier-Stokes equations have been increasingly used to predict control and stability derivatives in the early phase of the aircraft design, but a lot has yet to be done [1]. For this reason, more practical and simpler methods for the determination of the aerodynamic forces that could be used in conjunction with the equations of motion have been constantly sought. These methods can be divided into physical and functional modeling methods. Physical modeling methods for the aerodynamic forces are those directly derived from the very first physical principles. One example of a physical method is the unsteady vortex lattice method and its reduced order model [2]. The physical methods may have the advantage of not being derived from test data, but they usually are too computationally expensive for use either in simulation or in global stability analysis. The functional modeling methods are those that use mathematical expressions or equations to reproduce input/output response. In this work, we evaluate functional modeling methods that in previous research have shown the ability to reproduce the dynamic behavior of unsteady aerodynamics in longitudinal motion.

The conventional quasi-steady functional modeling techniques – the idea of making the equations linear by taking Taylor series expansion of the aerodynamic forces in terms of the vehicular velocity, angular rates, and their derivatives with respect to time - has been used for most flight dynamics studies since 1911 [3]. For the years that followed, the aerodynamic functions were approximated by linear expressions leading to a concept of stability and control derivatives. As modern fighters reached high angles of attack and performed maneuvers at high angular rates, the linearized methods became insufficiently accurate for analysis. The addition of nonlinear terms, expressing, for example, changes in stability derivatives with the angle of attack, extended the range of flight conditions to high-angle-of-attack regions and/or high-amplitude maneuvers. In both approaches, using either linear or nonlinear aerodynamics, it is assumed that the parameters appearing in polynomial or spline approximations are time invariant. However, high-performance fighters have the capability to operate not only at high angles-of-attack but also with high angular rates, situations where severely separated flow conditions prevail. Under these conditions, the aerodynamic loads may be not only highly nonlinear but also time dependent. We shall remember that future combat air vehicles will probably be uninhabited. Without the pilot's physiological limitations, they will be capable of performing more agile maneuvers, also will take advantage of dynamic lift, and experience higher load factors, thus increasing the importance of capturing nonlinear unsteady aerodynamic phenomena and performing nonlinear stability analyses.

Some of the functional models that have been previously proposed to simulate unsteady aerodynamic behavior are described in this chapter. Also reviewed is the previous work done in the research of the phenomenon called wing rock.

1.1 Previous Work in Aerodynamic Functional Modelling

Bryan [3], who published the first complete analysis of the pitch stability of an aircraft at the very beginning of heavier-than-air flight, was probably the first to introduce modeling of the aerodynamic forces acting on the aircraft, and his model was linear. Since then, the idea of making the equations linear by taking Taylor series expansions of the

aerodynamic forces in terms of the vehicular velocity, aerodynamic angles, angular rates, and their time-derivatives has been used for most flight conditions. The linear terms associated with these expansions are known as *aerodynamic stability derivatives* [4] and an important fraction of the total effort in aerodynamic research in the past has been dedicated to find a methodology for their determination, by theoretical, semi-empirical and experimental means. The range of usefulness of this method can be extended to higher angles of attack by adding higher order nonlinear terms. However, the parameters appearing in conventional applications are assumed to be time-invariant.

This time-invariance does not correspond to results of studies in unsteady aerodynamics that started in the nineteen-twenties with Wagner [5]. He studied the unsteady lift on an airfoil due to abrupt changes in the angle of attack. His work was extended by Theodorsen [6] to compute forces and moments on an oscillating airfoil, whereas Kussner [7] studied the lift on an airfoil as it penetrates a sharp-edge gust. Cicala [8] and Jones [9] started to investigate the unsteady aerodynamics of finite wings.

The concern with modeling the unsteady aerodynamic effects is present in other works of Jones [9]-[12], who introduced the concept of the *indicial functions approach*. In [12], he extended the work in unsteady aerodynamics from wings to airplanes, by studying the effect of the wing wake on the lift of the horizontal tail. The formulation of linear, unsteady aerodynamics in the aircraft longitudinal equations in terms of indicial functions was further developed by Tobak in [13]. Later, in [14]-[17], Tobak et al expressed the longitudinal aerodynamic forces and moment as functionals of the angle of attack and the dimensionless pitch angular rate, free of the dependence on a linearity assumption. The indicial functions approach is considered the most systematic and rigorous functional way of representing unsteady aerodynamics, and it is currently applied [18]-[21],[22],[23],[24], but it is more difficult to combine this functional representation with the equations of an aircraft motion, which are written in the form of differential equations.

A nonlinear, lifting line procedure with unsteady wake effects was developed and studied for predicting wing-body aerodynamic characteristics up to and beyond stall by Levinsky [25] and Hreha [26]. In this *nonlinear lifting line formulation*, a discrete vortex lattice representation is used for the time-dependent wake, whereas the wing load distribution is assumed concentrated along the 25% chord line. Each chordwise section is assumed to act aerodynamically (including stall) like a 2D airfoil in steady flow at effective angle of attack, which may also be time dependent. Three-dimensional unsteady aerodynamic effects were included by allowing shed vortices in the wake to vary in strength with distance and time. The strengths of the shed vortices are related to those of the corresponding bound elements at an earlier time, based on the convective time delay at free stream velocity between the bound vortex and the particular wake station. Although the theory is unsteady from the point of view of wake-induced effects, it is assumed that the two-dimensional airfoil chordwise loadings and sectional characteristics in stall are steady state. The method is also limited to incompressible flow, and to wings of moderate sweep and from moderate to large aspect ratio. Some further applications of this formulation are shown in [27].

A functional approach to include unsteady aerodynamics in aircraft equations of motion was introduced by Goman et al in [28],[29], which consisted of a *state-space representation* of additional *internal state variables* that are used in the functional relationships for the aerodynamic forces and moments. Fan and Lutze [30] took their idea and combined it with the idea of extending the range of applicability to higher angles of attack by adding higher order nonlinear terms in the Taylor's series expansion. In addition to that, they defined the aerodynamic coefficients and derivatives as quadratic polynomials of an internal state variable related to the flow separation point position. The state-space representation is convenient for solving problems of flight dynamics because the inclusion of unsteady aerodynamics in the above form leads only to an increase in problem dimension and retains the possibility of investigating motion stability by means of classical methods. Nevertheless, this model, as it was originally proposed, is not capable of simulating multi-valued aerodynamic characteristics for quasi-static motion (static hysteresis). Later, Abramov, Goman, Khrabrov, and Kolinko [31] presented

another state-space representation of aerodynamic characteristics that included nonlinear terms and that was capable of describing static hysteresis. An additional state-space approach that could do this with fewer model parameters is the one presented by De Oliveira and Lutze [32].

Next, some functional unsteady aerodynamic models of more interest, selected among the ones mentioned before, are described in more detail.

1.1.1 Stability Derivatives Approach

In this method, the problem of airplane dynamics is formulated and the equations for six-degree-of-freedom motion are derived through Newton's laws. Because these equations are coupled and nonlinear, it is difficult to obtain analytical solutions. In view of this, it is assumed that the motion following a disturbance has small amplitudes in all the disturbed variables. With this assumption, it is possible to linearize the equations of motion about the chosen flight condition. If the airplane configuration allows the definition of a vertical plane of symmetry, it is possible to decouple the equations of motion into two sets: one for the longitudinal motion and another for lateral-directional motion. Nevertheless, there are cases where the decoupling is not possible, like for example, those whose mass distribution is not symmetric. Even in such cases, the linear equations of motion can be used in the stability analysis [33]. After linearization, it is assumed that the aerodynamic forces and moments in the disturbed state depend only on the instantaneous values of motion variables. This allows them to be evaluated by using the method of Taylor series expansion. With these approximations, the equations of motion become linear in all the motion variables. The aerodynamic coefficients appearing in the Taylor series expansion are called *stability and control derivatives*.

For flight conditions where massively separated flow conditions prevail, the linearized methods become insufficiently accurate for the analysis and more accurate aerodynamic models are required.

1.1.2 Indicial Approach

The concept of indicial aerodynamic functions may be defined briefly as "the aerodynamic response of the airfoil as a function of time to an instantaneous change in one of the conditions determining the aerodynamic properties of the airfoil in a steady flow" [13]. Recent developments and applications of the indicial approach to the representation of unsteady aerodynamics can be found in references [18], [19], and [22]. A short summary based on these references follows.

In this approach, the combined vector of the total aerodynamic coefficients $\vec{C} = \begin{bmatrix} C_D & C_Y & C_L & C_l & C_m & C_n \end{bmatrix}^T$ of an aircraft undergoing an arbitrary motion is the indicial response obtained in conjunction with the superposition principle [15], [16] or Duhamel's integral theorem (Appendix A.1). This indicial response is given by

$$\vec{C} = \int_0^t \mathbf{A}(t-\tau)\dot{\vec{h}}\,d\tau \qquad \textbf{(1-1)}$$

Where $\mathbf{A} = \left\{ A_{C_j}^{h_i} \right\}$ is a matrix of indicial response functions for stepwise variations of kinematic parameters and control surfaces deflections combined in the vector $\vec{h} = \begin{bmatrix} \alpha & \beta & p & q & r & \delta_a & \delta_e & \delta_r \end{bmatrix}^T$. That means that, in this approach, the variations with time of the aircraft kinematic variables such as angle of attack and angular velocity are replaced by a large number of small instantaneous step changes. The transient aerodynamic reactions to these step changes are named "indicial functions", and the total response is obtained by their superposition.

Even though this approach is considered a good representation of unsteady aerodynamics, it is difficult to combine it with the differential equations of motion. The indicial concept was originally conceived for linear time-invariant systems, but it has been generalized to

a nonlinear indicial response theory [22], leading to a much more complicated description.

1.1.3 State-Space Representation – The First Ideas

In the indicial approach, the aerodynamic coefficients are represented by integral-differential equations, which are neither easy nor suitable to combine with the airplane differential equations of motion. To overcome this difficulty, a state-space approach to represent unsteady aerodynamics was proposed in 1990 [28],[29], which added internal variables describing the state flow in the functional relationships for the aerodynamic coefficients for forces and moments. The values of the total aerodynamic force and moment depend on the kinematic parameters of the motion and on either the position of the flow separation or the position of the vortex breakdown. Thus the separation point position and the vortex burst point position were taken as internal dynamical variables in the original formulation of this type of representation. In this approach, an internal state variable $x(t)$ associated with the state of the flow was used to represent the unsteady aerodynamic effect. It can be associated either with the distance between the airfoil trailing edge and the position of the point of separation, in predominantly two-dimensional type of flows (Figure 1-1), or to the position along the chord of the vortex burst point, in predominantly vortical type of flows (Figure 1-2).

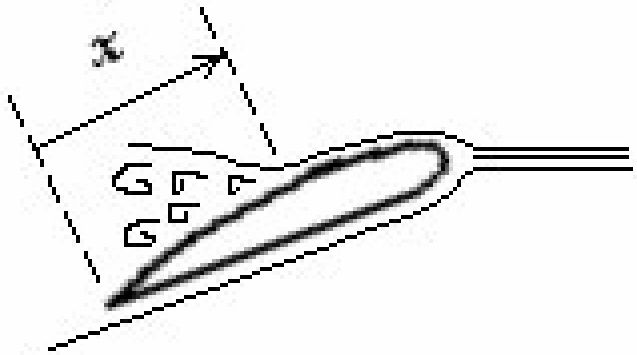

Figure 1-1 Internal state space variable in predominantly two-dimensional flows.

This internal state-space variable is then made non-dimensional by divison either by *M.A.C.* (wing mean aerodynamic chord), in case of wings with moderate to large aspect ratio, or by c_r (chord in the plane of symmetry), in case of wings with low aspect ratio. Therefore, the non-dimensional variable $\bar{x}(t)$ associated with $x(t)$ is $\bar{x}(t) = x(t)/M.A.C.$ or $\bar{x}(t) = x(t)/c_r$. Consequently, $\bar{x}(t) \in [0,1]$. As shown in figures 1-1 and 1-2, the value $\bar{x} = 0$ corresponds either to attached flow or to the absence of vortex breakdown over the wing, while $\bar{x} = 1$ corresponds to leading-edge separation or vortex burst at the apex. We take the wing trailing edge as the origin for $x(t)$ because it is consistent with the second-order polynomial model (equations (1-8)) adopted here for the stability derivatives, after the work of Fan & Lutze [30],[34]. This is in contrast to the reference system taken by Goman & Khrabrov [29], where the leading edge is adopted as the origin of $x(t)$.

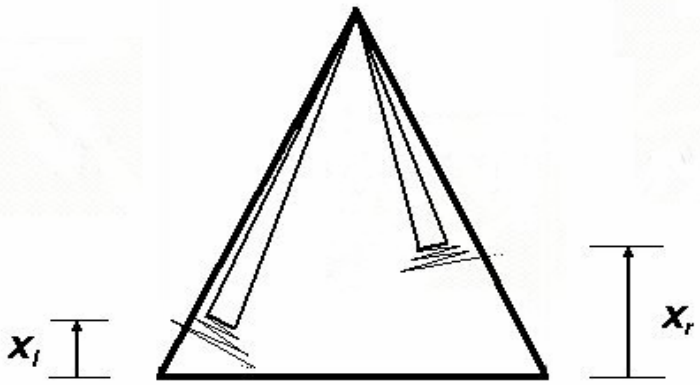

Figure 1-2 Internal state-space variable in predominantly vortical flows.

Taking into account the above features, a mathematical model was proposed [28],[29] where the internal dynamical variables (vector $\vec{x}$) approximately describes the state of separated and vortex flow about an aircraft. These variables are additional information required at a given instant of time to calculate the outputs (aerodynamic forces and moments, given by the vector $\vec{C} = \begin{bmatrix} C_D & C_Y & C_L & C_l & C_m & C_n \end{bmatrix}^T$) from the system inputs (motion variables and surfaces deflections, given by the vector $\vec{h} = \begin{bmatrix} \alpha & \beta & p & q & r & \delta_a & \delta_e & \delta_r \end{bmatrix}^T$). The unsteady aerodynamic state-space approach is then given by a dynamical system (1-2)

$$\frac{d\vec{x}}{dt} = f\left(\vec{x}, \vec{h}\right)$$

$$\vec{C} = g\left(\vec{x}, \vec{h}\right) \qquad \textbf{(1-2)}$$

To obtain the simplest mathematical model of this kind, Goman and Khrabrov [29] first considered the flow about a wing in pitching motion only. Then, the first equation of the dynamical system (1-2) was defined as:

$$\tau_1 \dot{x}(t) + x(t) = x_0\left(\alpha(t) - \tau_2 \dot{\alpha}(t)\right) \quad \textbf{(1-3)}$$

This definition was taken with two groups of unsteady fluid mechanics processes in mind. The first group concerns the different quasi-steady aerodynamic effects that have time-delays, such as circulation and boundary-layer convection lags. Since the resulting delay is approximately proportional to the variation of the angle of attack $\dot{\alpha}$, the quasi-steady value of the internal state variable can be expressed through the function $x_0(\alpha)$ by means of argument shift $x_0(\alpha - \tau_2 \dot{\alpha})$, where τ_2 defines the total time delay associated with the above-mentioned effects. The second group of fluid mechanics processes defines transient aerodynamic effects such as the dynamics of the flow adjustment to any change in the angle of attack. This dynamics can be described by the first-order differential equation (1-3), where τ_1 is the transient time-constant.

The steady state position $x_0(\alpha)$ of the separation point is generally a nonlinear function of the angle of attack. It can be obtained from static wind tunnel measurements, but, in order to be applicable for identification purposes, a mathematical relation would be more suitable.

In references [30],[34], Fan and Lutze started from the state-space model as proposed by Goman and Khrabrov [29], and further developed it to facilitate the identification process. Their first improvement was to propose the logistic or sigmoid function (1-4) shown below as the representation of $x_0(\alpha)$.

$$x_0\left(\alpha_{eff}(t)\right) \stackrel{\Delta}{=} \frac{1}{1 + \exp\left(\sigma\left(\alpha_{eff}(t) - \alpha^*\right)\right)} \quad \textbf{(1-4)}$$

where $\alpha_{eff}(t) = \alpha(t) - \tau_2 \dot{\alpha}(t)$, α^* is the angle of attack at which the flow separation is at the mid-chord point, and σ is the slope factor. Parameters α^* and σ are expected to be identified from wind tunnel experimental data. Figure 1-3 shows the influence of these parameters in the shape of the sigmoids for negative (a) and positive (b) values of σ. Because in the current work the sign of σ plays such an important role for the wing rock

representation, we write it explicitly, as it is shown in equation (1-5), and assume that $\sigma = |\sigma|$.

$$x_0(\alpha_{eff}(t)) = \frac{1}{1+\exp(\xi\sigma(\alpha_{eff}(t)-\alpha^*))} \quad \textbf{(1-5)}$$

with ξ = -1 or +1 for sigmoid functions that respectively increase or decrease with increasing values of α.

By considering the symmetrical motion in the longitudinal plane, the output equations were written as functionals of the kinematic variables involved in this kind of motion, that is,

$$C_a(t) = C_a(\alpha(t), \dot{\alpha}(t), q(t), \bar{x}(t)) \quad \textbf{(1-6)}$$

where a is the aerodynamic coefficient, like, for example, $a = D, L, m$

Since these functions are not known, practical schemes were developed [30],[34] to have them easily identified with the help of experimental data. In order to achieve that, Taylor series expansions of (1-6) in terms of the motion variables α and q were used, and the terms up to second order were retained. These expansions were taken around $(\alpha = 0, q = 0)$, while holding the state $\bar{x}$ fixed.

Taking the lift coefficient output equation as example ($a = L$), we have:

$$C_L(t) = C_{L0} + C_{L\alpha}(\bar{x})\alpha + C_{L\hat{q}}(\bar{x})\hat{q} + \Delta^2 C_L \quad \textbf{(1-7)}$$

Where $\Delta^2 C_L$ represents the second-order terms, that is

$$\Delta^2 C_L = C_{L\alpha^2}(\bar{x})\alpha^2 + C_{L\hat{q}^2}(\bar{x})\hat{q}^2 + C_{L\alpha\hat{q}}(\bar{x})\alpha\hat{q}$$

Here, $\hat{q} = q\hat{t}$ is the nondimensional pitch rate, and $\hat{t} = \frac{c}{2V}$ is the characteristic time of the flow, sometimes called convective time.

In the above equations (1-6) and (1-7), the stability derivatives are no longer constant as in the conventional approach, but assumed as functions of the internal state variable $\bar{x}$. To allow for parameter identification, they were defined in references [30],[34] as quadratic polynomials of the internal state variable $\bar{x}$, that is,

$$
\begin{aligned}
C_{L\alpha}(\bar{x}) &= a_1 + b_1\bar{x} + c_1\bar{x}^2 \\
C_{L\hat{q}}(\bar{x}) &= a_2 + b_2\bar{x} + c_2\bar{x}^2 \\
C_{L\alpha^2}(\bar{x}) &= a_3 + b_3\bar{x} + c_3\bar{x}^2 \\
C_{L\hat{q}^2}(\bar{x}) &= a_4 + b_4\bar{x} + c_4\bar{x}^2 \\
C_{L\alpha\hat{q}}(\bar{x}) &= a_5 + b_5\bar{x} + c_5\bar{x}^2
\end{aligned}
\qquad \textbf{(1-8)}
$$

Where a_j, b_j and c_j, j = 1,2,…,5 are constants to be determined from experimental data. Similar expressions were derived for drag and pitching moment coefficients C_D and C_m.

Developments made in references [18] and [22] show that, for the linear domain, the indicial function approach is equivalent to the state-space representation.

1.1.4 Nonlinear Internal State Equation Model

The state-space approach described in the preceding section is not capable of representing some nonlinear phenomena like, e.g., static hysteresis. In [31], Abramov et al introduced a more comprehensive variation of this approach that is capable of making up for these shortcomings. They developed a nonlinear model that naturally describes static hysteresis and critical state crossings [35], by connecting them to the mathematical phenomenon known as the Riemann-Hugoniot catastrophe [36]. Their model is built based on the assumption that the contributions from potential or attached (*pt*) and separated (*sp*) flows have different time scales and must be represented separately, as shown in Eq. (1-9):

$$C_N(t) = C_{N\,pt}(\alpha) + C_{N\,pt\,\dot{\alpha}} \frac{\dot{\alpha}\, c}{V} + C_{N\,sp}(t) \tag{1-9}$$

where $C_{N\,pt}(\alpha), C_{N\,pt_{\dot{\alpha}}}$ are the static dependency and aerodynamic derivative for attached flow. The term $C_{N\,sp}(t)$ defines the separated flow contribution that accounts for all the nonlinear unsteady effects. To describe the transition from an attached to a fully stalled flow, they introduced an internal state variable, $0 \le x \le 1$, associated with the size of the separated region of the wing, such that

$$C_{N_{sp}}(t) = g(x(t))\left[\Delta C_{N_{fs}}(\alpha) + \Delta C_{N_{fs_{\dot{\alpha}}}} \frac{\dot{\alpha} c}{V}\right] \tag{1-10}$$

where $g(x(t))$ is the weight function, equal to zero for fully attached flow and to 1 for fully separated conditions. The terms $\Delta C_{N\,fs}(\alpha) = C_{N_{fs}}(\alpha) - C_{N_{pt}}(\alpha)$, $\Delta C_{N_{fs_{\dot{\alpha}}}} = C_{N_{fs_{\dot{\alpha}}}} - C_{N_{pt\dot{\alpha}}}$ are the aerodynamic contributions due to fully separated or stalled (*fs*) conditions.

To allow the model to describe static hysteresis and critical states, the following nonlinear dynamic equation for the internal state variable *x* was introduced:

$$\frac{dx}{dt} = F(\alpha_*, x) \tag{1-11}$$

where $F = k_0(\alpha_*) + k_1(\alpha_*)x + k_2(\alpha_*)x^2 + k_3(\alpha_*)x^3$ and $\alpha_* = \alpha - k_{\dot{\alpha}} \frac{\dot{\alpha} c}{V}$. This third order polynomial defined as the right hand side of Eq. (1-11) allows the representation of the two stable branches in static hysteresis. Since each set of coefficients $k_0(\alpha_*), k_1(\alpha_*), k_2(\alpha_*), k_3(\alpha_*)$ define a different set of equilibrium points $\{x_e \text{ s.t. } F(\alpha, x_e) = 0\}$ for each angle of attack, the model can represent flows with one or two stable branches, being able of naturally identify models with static hysteresis.

When this model is used for parameter identification, we can see that it is necessary to identify one set of coefficients $k_0(\alpha_*), k_1(\alpha_*), k_2(\alpha_*), k_3(\alpha_*)$ for each angle of attack

chosen for the calculations, and this can make the number of required parameters too large to be identified.

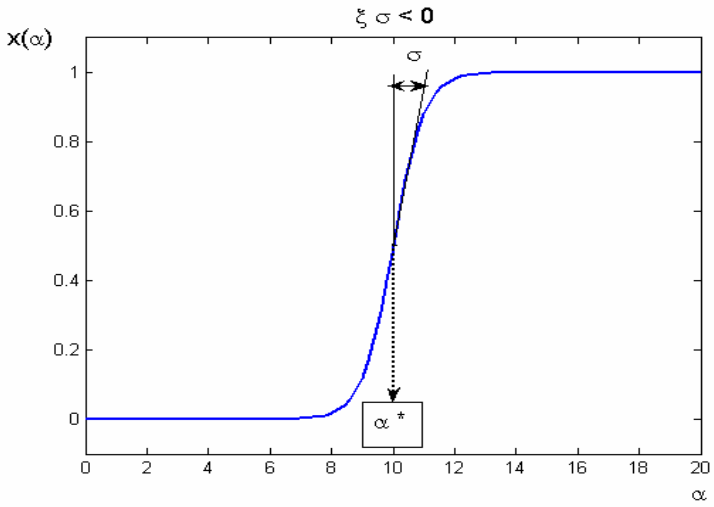

(a)

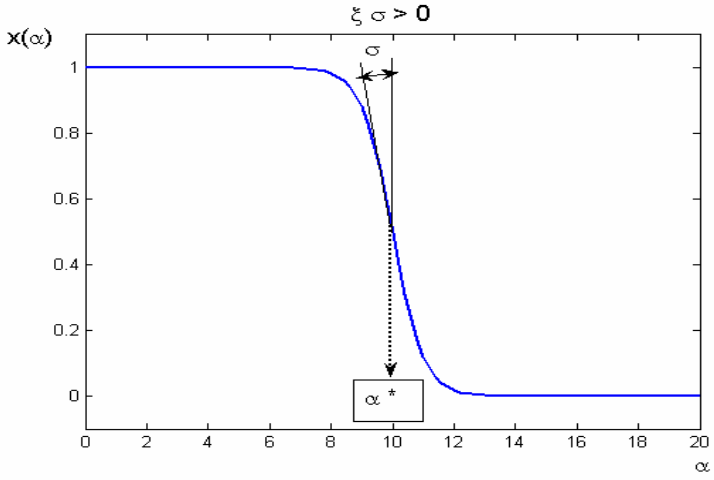

(b)

Figure 1-3 Influence of the parameters α^* and σ in the sigmoid shape for the cases where (a) ξ = -1; (b) ξ = 1.

1.1.5 State-Space Representation – One More Idea

Trying to find a simpler formulation that could also represent the static hysteresis phenomenon, de Oliveira Neto and Lutze came up with the model described in [32]. It is the result of a modification made to the model described in [30] in such a way that the internal state equation has a driving (or forcing) term that switches between two functions, that is:

$$\tau_1 \frac{d\bar{x}}{dt} + \bar{x} = U\, \bar{x}_{0U}\left(\alpha_{eff}\right) + D\, \bar{x}_{0D}\left(\alpha_{eff}\right) \qquad \textbf{(1-12)}$$

where $\bar{x} \in [0,1]$ is a non-dimensional coordinate that is related to the separation properties of the flow, τ_1 is a time-constant to be identified, and $\alpha_{eff} = \alpha - \tau_2 \dot{\alpha}$, with τ_2 being also a constant to be identified. The state variable $\bar{x}$ represents the non-dimensional distance from the trailing edge to either the position of the separation point or the position of the vortex breakdown, measured from the trailing edge and divided by the chord. Like the model described in (1.1.3), the constant τ_1 represents the relaxation time-constant that defines the transient aerodynamic effects like the dynamic properties of the separated flow adjustment when a flow condition is changed, and τ_2 defines the total time delay of the flow separation and reattachment due to the quasi-steady aerodynamic effects such as the circulation and boundary layer convection lags.

Since in cases where static hysteresis is present the flow exhibits different characteristics when the wing is going up or down in a quasi-static motion, in Eq. (1-12) an internal dynamic right-hand side term that can switch between two driving functions was defined. This switching function is $x_s = U\, x_{0U}\left(\alpha_{eff}\right) + D\, x_{0D}\left(\alpha_{eff}\right)$, where the terms $x_{0U}\left(\alpha_{eff}\right)$ and $x_{0D}\left(\alpha_{eff}\right)$ are the steady state dependency of the separation property on the angle of attack for the body going up and down, respectively. They are continuous, sigmoid-type functions defined as

$$x_{0U}(\alpha_{eff}) = \frac{1}{1+\exp\left[-\sigma_U(\alpha_{eff}-\alpha_U^*)\right]} \tag{1-13}$$

$$x_{0D}(\alpha_{eff}) = \frac{1}{1+\exp\left[-\sigma_D(\alpha_{eff}-\alpha_D^*)\right]} \tag{1-14}$$

where $\alpha_{(\bullet)}^*$ is the angle of attack at which the flow separation or the vortex burst position is at the mid-chord point, and $\sigma_{(\bullet)}$ is the slope factor. An example of the flow separation functions for up and down motions with the parameters $(\alpha_U^* = 15.7\,\text{deg},\ \alpha_D^* = 20.1\,\text{deg},\ \sigma_U = 31.7,\ \sigma_D = 14.5)$ is shown in Figure 1-4. We can observe in this figure the influence of $\alpha_{S(\bullet)}$ and $\sigma_{(\bullet)}$ on the shape of the sigmoids. The parameters *U* and *D* on the right-hand side of Eq. (1-12) are respectively defined as

$$\begin{aligned} U &\triangleq \frac{1+sign(\Delta\alpha)}{2} \\ D &\triangleq \frac{1-sign(\Delta\alpha)}{2} \end{aligned} \tag{1-15}$$

where $\Delta\alpha = \alpha_{i+1} - \alpha_i$ for the given sequence of the static angles of attack α_i, $i = 1,2,\ldots,l$ correspond to the wind tunnel measurements of the aerodynamic coefficients $\{\hat{C}_a(\alpha_i),\ i = 1,2,...,l\}$, and where $\Delta\alpha = \alpha(t_{i+1}) - \alpha(t_i)$ for the given time histories of angles of attack $\{\alpha(t_i),\ 0 \le t_i \le t_n\}$ correspond to the wind tunnel measurements of the aerodynamic coefficient time histories $\{\hat{C}_a(t_i),\ i = 1,2,...,n\}$. The subscript *a* represents the type of coefficient being modeled, for example *a* = *D, L* or *m*.

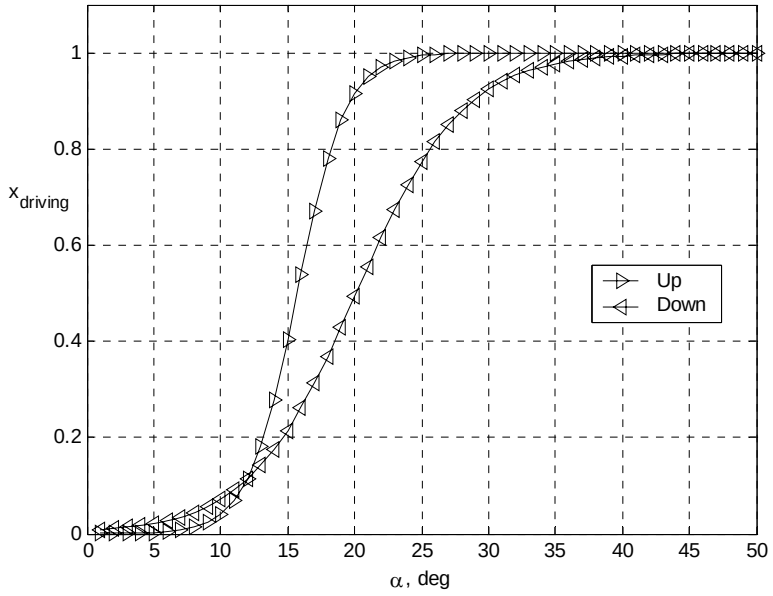

Figure 1-4 Example of the internal state equation driving function.

The output equations for the aerodynamic coefficients are defined to be functions of the internal state $\bar{x}(t)$, the angle of attack $\alpha(t)$, the pitch rate $q(t)$, and are, as in [34], written in the following form:

$$C_a = C_{a0} + C_{a\alpha}(\bar{x})\alpha + C_{a\hat{q}}(\bar{x})\hat{q} + \Delta^2 C_a \qquad \textbf{(1-16)}$$

with

$$\Delta^2 C_a \overset{\Delta}{=} C_{a\alpha^2}(\bar{x})\alpha^2 + C_{a\hat{q}^2}(\bar{x})\hat{q}^2 + C_{a\alpha\hat{q}}(\bar{x})\alpha\hat{q}$$

being the nonlinear part of the equation, where *a* represents the aerodynamic coefficient modeled.

$\hat{q} = q\hat{t}$ is the non-dimensional pitch rate and $\hat{t}$ is the characteristic time of the flow, defined as

$$\hat{t} = \frac{c}{2V}, \qquad \textbf{(1-17)}$$

c being a characteristic length, and V the airspeed. It is worthwhile noting that the convective time c/V is related to the time it takes for an air molecule to travel along the wing mean aerodynamic chord. The factor ½ is included in Eq. (1-17) because it was used to determine the non-dimensional pitch rate in most of the references related to unsteady aerodynamics and flight dynamics. The reason for that is probably just tradition. The mid-chord was historically taken as the coordinate origin for a pitching airfoil in unsteady aerodynamics analysis and, as a natural consequence, the semi-chord was introduced as the characteristic length [37],[38].

The stability derivatives in Eq. (1-16) are defined as quadratic polynomials of the non-dimensional state variable $\bar{x}$, that is

$$C_{a\chi}(\bar{x}) = a_{a\chi} + b_{a\chi}\bar{x} + c_{a\chi}\bar{x}^2,$$

where a is the type of aerodynamic coefficient, and χ represents the motion variables with respect to which the partial derivatives were taken. In this case, $\chi = \alpha, \hat{q}, \alpha^2, \hat{q}^2, \alpha\hat{q}$.

In [32] this formulation was used to represent the static hysteresis of an NACA 0018 airfoil, reported in [31]. The comparison between wind tunnel data and model responses for pitching moment and normal force coefficients can be seen in Figure 1-5 and Figure 1-6, respectively. They show that this formulation matches very well experimental results.

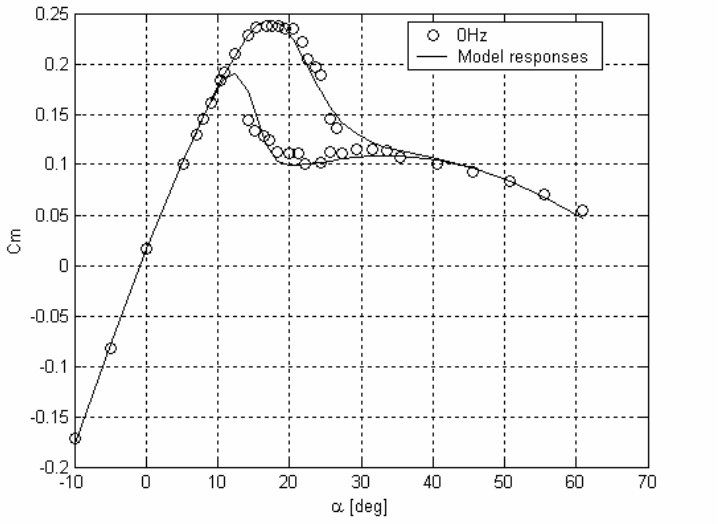

Figure 1-5 Experimental and model responses static pitching moment for a rectangular wing with NACA 0018 airfoil. Experimental data were taken from [31].

1.1.6 Aircraft Multi-Axis State-Space Formulation

The method presented in the section 1.1.5 can be used to represent only symmetrical longitudinal motion of wings and airplanes. Trying to find some formulation that could represent more general types of motion, we composed this method with the formulation originally described by Lutze, Fan and Stagg in [39] and [40] to build the models that have the ability to represent wing rock investigated in their research. This later formulation is briefly reproduced in this section for the convenience of the reader. The primary idea behind this method is the decomposition of the aircraft into several elements that contribute to the resulting aerodynamic force. These elements are small lifting surfaces that are referred to as *panels*. The approach taken is one of modeling the local forces and moments associated with the contributing lifting surfaces of the aircraft such as left and right wings, left and right horizontal tails, vertical tail, and surfaces

representing forward and aft fuselage. When an airplane rotates in the air, the air velocity is different at each surface, making the local angles of attack also different. Since the state-space model is based upon characterizing flow separation as a function of angle of attack, the work in this model is done using the local angle of attack and its time derivative. The local forces and moments can be calculated on each panel and, when combined with the forces and moments on the remaining panels, the total forces and moments for the whole aircraft are obtained. The goal is not only to characterize the rolling moment, but also the forces and moments along and about the other axes. The idea is to have one model capable of the prediction of lateral/directional characteristics as well as the longitudinal ones, even in the high angle of attack, unsteady aerodynamic region.

Next, the description of the basic model for each of the single lifting surfaces in this formulation is reproduced with its original notation.

► Normal Force on Left and Right Wings

The aerodynamic normal force acting on the left and right wing is represented in this model by the following state-space formulation [30],[34],[39],[40] :

$$\tau_{w1}\frac{dx_{wi}}{dt} + x_{wi} = x_{w0}\left(\alpha_{wi} - \tau_{w2}\dot{\alpha}_{wi}\right)$$

$$C_{Nwi} = C_{Nw0i} + C_{Nw\alpha i}\left(x_{wi}\right)\alpha_{wi} + C_{Nw\dot{\alpha} i}\left(x_{wi}\right)\dot{\alpha}_{wi} \qquad \textbf{(1-18)}$$

where subscript "*w*" represents quantities of the wing or the forward group of lifting surfaces, and *i* = *l* or *r*, respectively, standing for the left or right panel. In the state equation of (1-18) τ_{w1} is the wing panel relaxation time constant defining the transient aerodynamic effects and τ_{w2} quantifies the time delay due to the quasi-steady aerodynamic effects about the wing panel. The variable x_{wi} is the wing panel state variable associated with the nonlinear flow effects, and $x_{w0}\left(\alpha_{wi}\right)$ is the static dependency

of the state variable on the local angle of attack, given by the sigmoid-type function defined by

$$x_{w0}(\alpha_{wi}) = \frac{1}{1+\exp\left(-\sigma_w\left(\alpha_{wi}-\alpha^*_w\right)\right)} \qquad \textbf{(1-19)}$$

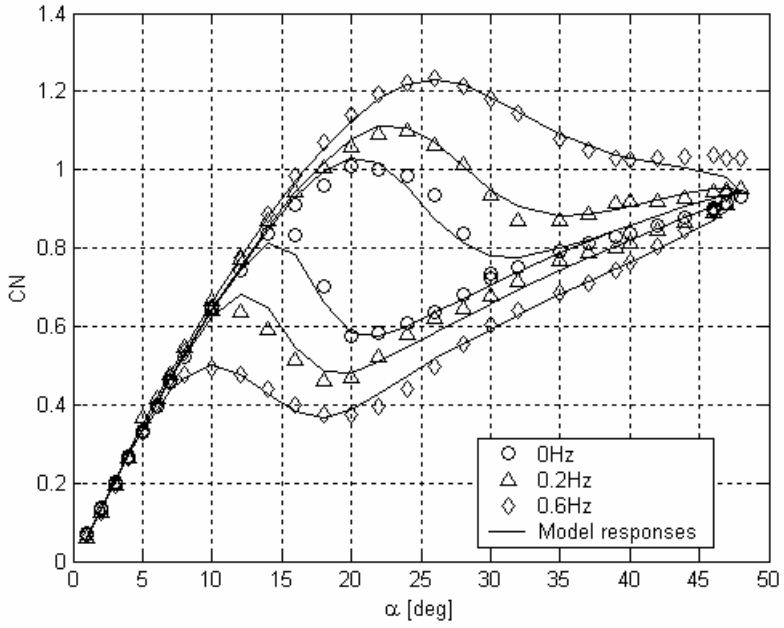

Figure 1-6 Experimental and predicted C_N responses for large amplitude pitch oscillations of a rectangular wing with NACA 0018 airfoil. Experimental data were taken from [31]

In equation (1-19) α_w^* describes the location of this function, σ_w is the slope factor, and α_{wi} is the local angle of attack of the wing panel at a location along the wing span at a distance l_w from the axis of the fuselage. In this work the primary concern is with pure rolling oscillatory motions. For this kind of motion the local velocity components at that location can be expressed in the body-axis system as (see Appendix A.2),

$$u_w = V_T \cos\theta_0$$

$$v_w = V_T sin\theta_0 sin\phi \qquad \textbf{(1-20)}$$

$$w_w = V_T sin\theta_0 \cos\phi \mp l_w\dot{\phi}$$

where the negative sign corresponds to the left wing panel while the plus sign to the right wing panel. The angle of attack and the sideslip angle are defined as,

$$\alpha = \tan^{-1}\frac{w}{u} \qquad \textbf{(1-21)}$$

$$\beta = sin^{-1}\frac{v}{\sqrt{u^2+v^2+w^2}}$$

Subtituting (1-20) into (1-21), the local angle of attack values for the left and right wing panels can be calculated through

$$\alpha_{wl} = \tan^{-1}\left(\tan\theta_0\cos\phi - \frac{l_w\dot{\phi}}{V_T\cos\theta_0}\right)$$

$$\alpha_{wr} = \tan^{-1}\left(\tan\theta_0\cos\phi + \frac{l_w\dot{\phi}}{V_T\cos\theta_0}\right) \qquad \textbf{(1-22)}$$

The output of the system (1-18) is C_{Nwi}, the normal force coefficient on the left or right wing panel. The derivatives $C_{Nwi\alpha}(x_{wi})$ and $C_{Nwi\dot{\alpha}}(x_{wi})$ are modeled as,

$$C_{Nwi\alpha}(x_{wi}) = a_{w1} + b_{w1}x_{1i} + c_{w1}x_{wi}^2$$

$$C_{Nwi\dot{\alpha}}(x_{wi}) = a_{w2} + b_{w2}x_{wi} + c_{w2}x_{wi}^2 \quad \textbf{(1-23)}$$

where a_{wj} , b_{wj} , and c_{wj} are constants to be identified from experimental results.

► Normal Force on Left and Right Horizontal Tails

The horizontal tail is modeled in a similar way to the wing, by

$$\tau_{t1}\frac{dx_{ti}}{dt} + x_{ti} = x_{t0}(\alpha_{ti} - \tau_{t2}\dot{\alpha}_{ti})$$

$$x_{t0}(\alpha_{ti} - \tau_{ti2}\dot{\alpha}_{ti}) = \frac{1}{1+\exp(-\sigma_t(\alpha_{ti} - \alpha_t^*))} \quad \textbf{(1-24)}$$

$$C_{Nti} = C_{Nti0} + C_{Nti\alpha}(x_{ti})\alpha_{ti} + C_{Nti\alpha^2}(x_{ti})\alpha_{ti}^2 + C_{Nti\dot{\alpha}}(x_{ti})\dot{\alpha}_{ti}$$

Subscript "*t*" stands for horizontal tail, and the left and right horizontal tails are represented respectively by *i* = *l, r*.

Not considering the aerodynamic interference from the wing, the local angle of attack at the left and right horizontal tail panels is written as,

$$\alpha_{tl} = \tan^{-1}\left(\tan\theta_0\cos\phi - \frac{l_t\dot{\phi}}{V_T\cos\theta_0}\right)$$

$$\alpha_{tr} = \tan^{-1}\left(\tan\theta_0\cos\phi + \frac{l_t\dot{\phi}}{V_T\cos\theta_0}\right) \quad \textbf{(1-25)}$$

where l_t is the distance of the selected location on the horizontal tail panel from the aircraft longitudinal axis, also another parameter to be identified.

The aerodynamic derivatives in Eq. (1-24) are, like the wing, modeled by quadratic polynomials of the internal flow state variable as

$$C_{Nti\alpha}(x_{ti}) = a_{t1} + b_{t1}x_{ti} + c_{t1}x_{ti}^2$$

$$C_{Nti\alpha^2}(x_{ti}) = \alpha_{t2} + b_{t2}x_{ti} + c_{t2}x_{ti}^2 \qquad \textbf{(1-26)}$$

$$C_{Nti\dot{\alpha}}(x_{ti}) = \alpha_{t3} + b_{t3}x_{ti} + c_{t3}x_{ti}^2$$

► Side Force on Vertical Tail

The sideslip angle values were relatively small in the wind-tunnel tests reported in Refs. [39], [40]. Because of that, the classic stability derivative approach was used to model the aerodynamic side force acting on the vertical tail, that is,

$$C_{Yv} = C_{Yt\beta}\beta_v + C_{Yt\dot{\beta}}\dot{\beta}_v \qquad \textbf{(1-27)}$$

Where $C_{Yt\beta}$ and $C_{Yt\dot{\beta}}$ are constant parameters. In Eq. (1-27), β_v and $\dot{\beta}_v$ are, respectively, local sideslip angle and its time-derivative at a selected location on the vertical tail. The distance of this location from the longitudinal body axis is represented by parameter l_3. For the pure rolling oscillatory motion, β_v can be obtained as

$$\beta_v = sin^{-1}\left(sin\theta_0 sin\phi + \frac{l_3\dot{\phi}}{V_T}\right) \qquad \textbf{(1-28)}$$

In case of larger values of the sideslip angle, parameters $C_{Yv\beta}$ and $C_{Yv\dot{\beta}}$ could also be defined as quadratic polynomials of some local, internal flow state variable.

► Side Force on the Fuselage

In this formulation, the only fuselage contribution to appear explicitly is that related to the lateral force. The fuselage contribution to the normal force is assumed to be lumped into those from the wing and the horizontal tail. For the same reason as in the case of the vertical tail, the side force acting on the fuselage is modeled as,

$$C_{Yb} = C_{Yb\beta}\beta + C_{Yb\dot{\beta}}\dot{\beta} \tag{1-29}$$

where β and $\dot{\beta}$ are, respectively, the aircraft sideslip angle and its time-derivative.

The panel contributions are then summed up in an appropriate way to give the approximate aerodynamic characteristics of the whole aircraft, as shown below for a conventional airplane configuration.

► Normal Force Coefficient

The normal force coefficient of the aircraft is obtained by adding up the wing and horizontal tail contributions, that is

$$C_N = \left(C_{Nwl} + C_{Nwr}\right) + \left(C_{Ntl} + C_{Ntr}\right) \tag{1-30}$$

► Side Force Coefficient

The contributors to the side force are the vertical tail and the fuselage. Thus,

$$C_Y = C_{Y_v} + C_{Yb} \tag{1-31}$$

► Pitching Moment Coefficient

Two components contribute to this coefficient: wing and horizontal tail. Adding the normal forces of these components multiplied by their corresponding arms about the transversal body axis y , the pitching moment coefficient is given by

$$C_m = \left(C_{Nwl} + C_{Nwr}\right)\frac{x_w}{c} - \left(C_{Ntl} + C_{Ntr}\right)\frac{x_t}{c} \tag{1-32}$$

where x_w and x_t are, respectively, the distances of the wing and horizontal tail aerodynamic centers to the aircraft C.G., and c is the aerodynamic chord length.

► Rolling Moment Coefficient

The rolling moment of the aircraft is generated by the normal forces on wing and horizontal tail panels, and by the side force from the vertical panel forces, all multiplied by arms about the longitudinal body axis *x*. Proceeding this way, the rolling moment coefficient is obtained as,

$$C_l = \left(C_{Nwl} - C_{Nwr}\right)\frac{y_w}{b} + \left(C_{Ntl} - C_{Ntr}\right)\frac{y_t}{b} + C_{Yv}\frac{z_v}{b} \qquad \textbf{(1-33)}$$

where y_w, y_t, and z_v are the moment arms for the wing, horizontal tail, and vertical tail, respectively, about the body axis *x*. The parameter *b* is the wing span.

► Yawing Moment Coefficient

Yawing moment contributors are the elements where side forces are applied. Then, the yawing moment coefficient is generated by the vertical tail and fuselage as follows,

$$C_n = -C_{Yv}\frac{x_v}{b} - C_{Yb}\frac{x_b}{b} \qquad \textbf{(1-34)}$$

where x_b and x_t are, respectively the moment arms of the fuselage and the vertical tail side forces with respect to the aircraft C.G.

1.2 The Wing Rock Phenomenon

Wing rock is defined in reference [41] as “uncommanded lateral-directional motion, viewed by the pilot primarily as a roll oscillation.” For some types of aircraft configurations, as the angle of attack further increases up to some critical value around 20 degrees a roll oscillation starts to grow in amplitude until it reaches a maximum value. At this point, the airplane continues to rock in a classic limit cycle behavior. This behavior occurs up to a higher critical value of the angle of attack (typically around 50 degrees). After that higher critical value of the angle of attack value, the roll oscillations are damped out.

This kind of phenomenon was first observed at NASA´s Langley Research Center around 1980 [42]. Wing rock can be described as a Dutch roll type of motion, during which the aircraft has sustained rigid body oscillations predominantly in roll, but also in yaw. It can appear in the subsonic flight regime and high angle of attack, or at transonic speeds and more moderate values of angle of attack [43]. When any perturbation in roll happens at higher values of the angle of attack, such as landing in crosswind or high load factor non-coordinated maneuvers, wing rock can develop. A variety of aircraft exhibited this phenomenon, but the most susceptible configurations have highly swept planforms or strakes and long slender forebodies that produce vortical flows during excursions into the high angle-of-attack regime. In general, it may adversely affect the whole flight envelope, but it can be particularly dangerous if it happens during landing, when it limits the approach angles of attack of military, commercial high-speed civil transport aircraft configurations or orbital space shuttles. At higher speeds, it can also pose serious limitation to combat effectiveness both in subsonic and in transonic flow regimes, and severely limits the pilot’s ability to perform a tracking task.

Wing rock has been encountered during the development of many military aircraft in service today. Some of the aircraft which have been documented to experience wing rock

are the A-4 Skyhawk, F-4 Phantom, F-5 Tiger, T-38 Talon, F-14 Tomcat, F-16 Fighting Falcon, F-18 Hornet, X-29, X-31, HP-115 [44], Gnat trainer, Tornado, and Harrier.

We can see wing rock from two perspectives: from the global perspective of the flight dynamics or the particular perspective of the physical mechanisms that happens on each case. From the flight dynamics perspective, wing rock can be explained by the behavior of the stability derivatives and the energy exchange concept [45], summarized in Section (1.2.1) of this report. When it comes to the behavior of the stability derivatives, under a certain critical value of the angle of attack, the airplane exhibits stable dynamic lateral stability and roll motions following a disturbance damp out. This stable dynamic lateral stability is equivalent to positive roll damping, which means negative C_{l_p}. At a certain angle of attack, roll damping becomes negative. As shown by Nguyen *et al* [45], a loss of damping in roll at high angles of attack makes a configuration susceptible to wing rock but does not necessarily generate a sustained wing rock. To generate a sustained wing rock motion, an additional aerodynamic cause is necessary. For wing rock to occur, there must be a nonlinear variation of roll damping such that negative damping (destabilizing) exists at low values of sideslip/roll angle and positive damping (stabilizing) at higher values of sideslip/roll angle.

The flow mechanism of the wing rock at high angles of attack depends on the aircraft configuration, but the principal source of wing rock is the lifting surfaces. Thin, low-aspect ratio, highly swept delta wings are prone to develop wing rock at high angles of attack. However, aircraft configurations not having highly swept delta wings but featuring fuselages with long, slender forebodies are also known to exhibit wing rock. This latter type of wing rock is called *wing-body wing rock* or *forebody-induced wing rock* and it is known to occur even when the main lifting surface - the wing - is removed. For the configuration without the wing, the horizontal and vertical tail surfaces coming under the influence of the forebody vortex system produce the necessary rolling moments. From the published results on wing rock phenomenon, a good way to organize ideas is to classify wing rock occurrences according to three main types**:** slender-wing rock, conventional-wing rock, and wing-body rock, explained as follows.

Slender-wing rock is the occurrence of wing rock on highly swept-back, sharp leading edge delta wings, alone or with blended bodies, at sufficiently high angle of attack. It is triggered by some initial disturbance that initiates roll. Studies of the wing rock motion on flat plate, slender delta wings have provided interesting insights on the importance of unsteady aerodynamics to the wing rock motion [45], [46], [47]. At high angles of attack, slender wing flow separates right at the leading edge and generates vortices (the *leading edge vortices*). To describe the flow mechanism acting on this type of wing rock, consider a delta wing with sweep angle equal or larger than 76 degrees at an angle of attack between 20 and 50 degrees. Consider also a view from the trailing edge toward the leading edge. Now, let us suppose that a disturbance causes the wing to initially roll in the positive direction of the body axis. As the roll angle increases at a constant pitch angle, angle of attack and sideslip are related to the roll angle through Eqs. (A.2-6) in Appendix A.2. Because of these relations, the effective angle of attack on the wing decreases and the effective sideslip angle increases as the roll angle grows. The increased sideslip on the wing during roll causes the windward vortex on the down-going wing to move inboard and toward the upper surface, and the leeward vortex to move outboard and be lifted off. At a certain point, the rolling moment due to the vortex on the down-going wing takes over the moment associated with the "lifted-off" vortex, and the movement first stops and then reverts. When the roll angle is back to zero, the dynamic hysteresis associated with the vertical location of the two leading edge vortices results in a residual rolling moment that keeps the oscillations going on. It appears as if the vortices have a sort of "inertia"**:** their vertical positions during oscillation have a delay when compared to the static ones. We extracted from [46] figures 1-4 and 1-5 that show the non-dimensional vertical and spanwise body coordinates of the vortices core, in addition to the crossflow streamlines and pressure distribution curves, obtained from computational simulations by using a discrete vortex potential model. It can be observed that the lag in vortex position makes the upgoing wing closer to its corresponding vortex core, and that these different positions results in the wing residual rolling moment at zero roll angle.

Conventional wing rock is that occurring on airplanes having straight or moderate-swept wings, and moderate to high aspect ratio. It can be subdivided into conventional-wing rock that happens at low or at high subsonic Mach numbers. Because in this case the wing aspect ratio is higher, two-dimensional streamwise flow effects dominate the aerodynamics, and in the low subsonic regime this kind of wing rock is related to dynamic stall [48]. According to tests made on the F-5A [43], at transonic speeds wing rock was generated by a limit cycle mechanism due to the fluctuating pressure changes on the wing top surface, especially near the wing tip region. In the cases observed, the major reason for the pressure change was the motion-induced variations in local angle of attack, which alternatively caused leading edge stall and recovery. Those fluctuating pressure changes are caused by flow separation driven by the shock-boundary layer interaction.

Forebody-induced wing rock is that type of wing rock that happens because of vortices generated by the fuselage forebody. A generic aircraft model featuring a slender, pointed fuselage forebody was used in tests described in [49]. This generic aircraft model exhibited wing rock when fitted with different wings of varying aspect ratio and sweep, or even without any wing at all. Therefore, for this type of wing rock, the wing itself was not the primary cause of the motion. One possible explanation is the one found in reference [50]. According to Ericson, at higher angles of attack, the airplane loses damping in roll and sheds forebody vortices in an asymmetric way. These vortices are convected towards the tail surfaces, sucked down over their upper surfaces and produced the necessary rolling moments. Therefore, the lifting surfaces, either the wings or the tail surfaces, when coming under the influence of forebody vortices, served as rolling moment generators to sustain the wing rock. That is the reason that this kind of wing rock is called *forebody-induced wing rock*.

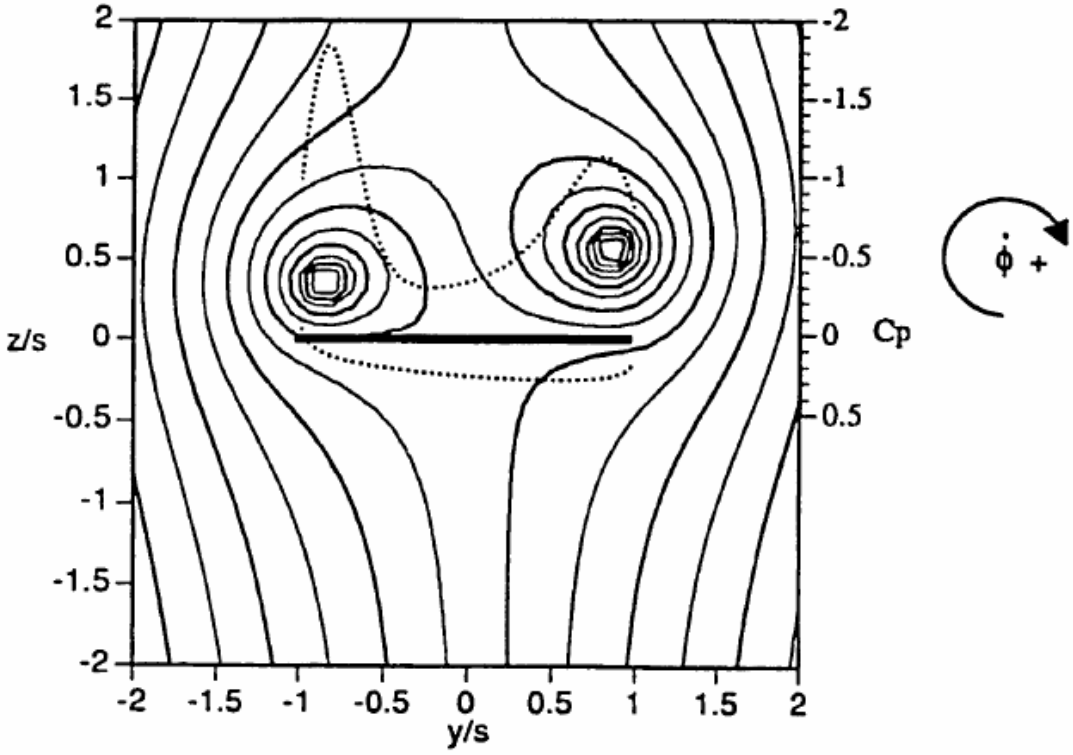

Figure 1-7 Crossflow streamlines and pressure distribution (dot line) for zero roll angle and positive roll rate. Figure reproduced from [46] with permission of the author.

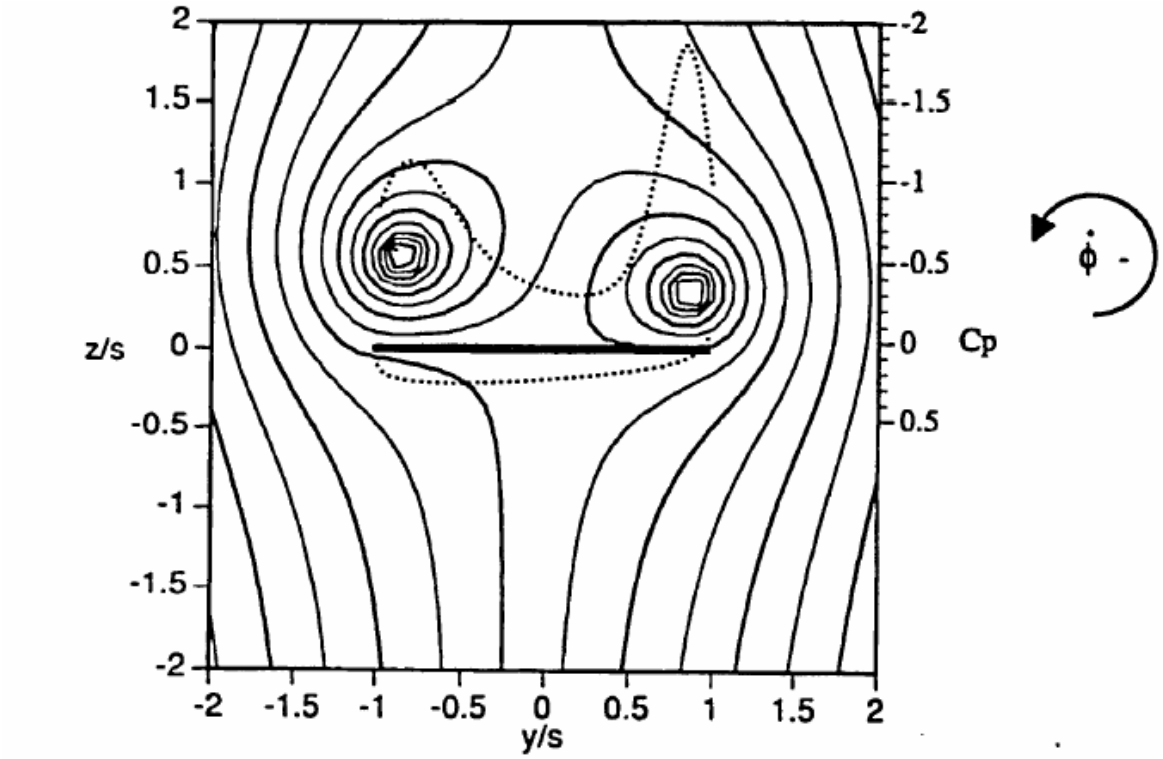

Figure 1-8 Crossflow streamlines and pressure distribution (dot line) for zero roll angle and negative roll rate. Figure reproduced from [46] with permission of the author.

1.2.1 The Energy Exchange Concept

When the model rolling moment coefficient as a function of the roll angle $C_l(\phi)$ can be determined for a wing undergoing wing rock, the energy exchange technique used by Nguyen et al [45] is very helpful in analyzing the physical mechanisms driving the limit-cycle oscillation. If we consider the case where the model is constrained to one degree of freedom, the equation of motion for the system is

$$I_{xx}\ddot{\phi}(t) = \sum L_R(t) = L_{aero} + \overbrace{L_{friction}}^{\approx 0} = q_\infty SbC_l(t)$$

$$\Rightarrow C_l(t) = \frac{I_{xx}\ddot{\phi}}{q_\infty Sb} \qquad \textbf{(1-35)}$$

Thus, when the model geometry, inertia, wind tunnel test conditions and roll angle time history are known, the rolling moment coefficient time-history $C_l(t)$ can be determined. The energy added to or extracted from the system during the motion for a specific time interval can be expressed as

$$\Delta E = q_\infty \, S \, b \int_{t_1}^{t_2} C_l(t)\,\dot{\phi}\,dt \qquad \textbf{(1-36)}$$

Eq. (1-36) may be rewritten in terms of the instantaneous roll angle $\phi(t)$ as the following line integral:

$$\Delta E = q_\infty \, S \, b \int_{C_\phi} C_l[\phi(t)]\,d\phi \qquad \textbf{(1-37)}$$

where C_ϕ is the curve obtained by plotting C_l as a function of the instantaneous roll angle $\phi(t)$ for the interval $[t_1, t_2]$. Therefore, the energy exchanged in a cycle of motion is directly related to the area enclosed by C_ϕ. Figure 1-9 shows the conceptual drawings of

possible cases for C_ϕ, where the arrows indicate the direction in time. When the loop encloses an area in a clockwise sense, energy is being added to the system (Figure 1-9a), whereas counterclockwise loops indicate energy dissipation from the system (Figure 1-9b). If a limit cycle occurs, the net energy exchange is zero (Figure 1-9c). Figure 1-10 shows the actual roll angle time-history of a slender delta wing at an angle of attack where the roll oscillations damp out. It was obtained from wind tunnel tests by Arena, and reported in [46] and [51]. The corresponding $C_l \times \phi$ loop is shown in Figure 1-11. Figure 1-12 presents a time history of wing rock buildup at $\theta_0 = 30°$ for tests reported in [51]. The dynamic rolling moment characteristics of the buildup cycle *A* are shown in Figure 1-13, where the clockwise loop in the plot indicates a dynamic instability. Notice that the restoring moment is roughly linear with roll angle. Since energy is being fed to the system, the roll angle amplitude is increasing. When the loop is very thin like the one shown, it accounts for the fact that the buildup happens very slowly. The analogous plot of the rolling moment coefficient after the system has reached steady state (cycle B) can be seen on Figure 1-14. There still is an unstable region between -20° and 20°, but two stable damping "lobes" have formed for the larger roll angles. The limit cycle oscillation is sustained because the area of the lobes equals the area of the unstable portion of the plot such that the net energy exchange is zero.

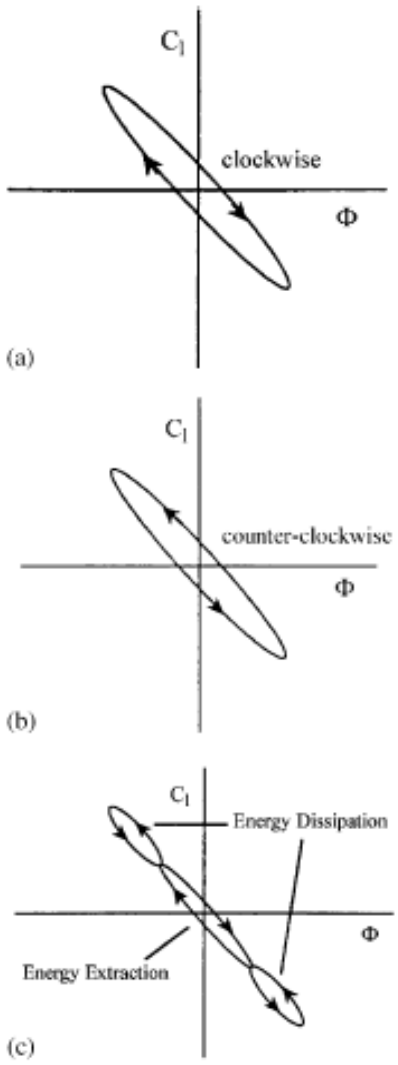

Figure 1-9 Conceptual drawings of the rolling moment coefficient *versus* roll angle. Figure reprinted from [52] by permission of the author.

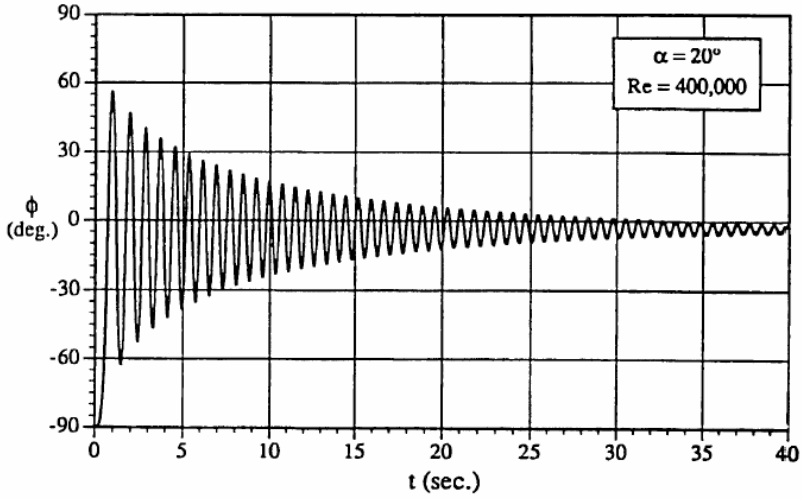

Figure 1-10 Roll angle time-history for wing pitch angle where there is no wing rock. Figure reprinted from [46] by permission of the author.

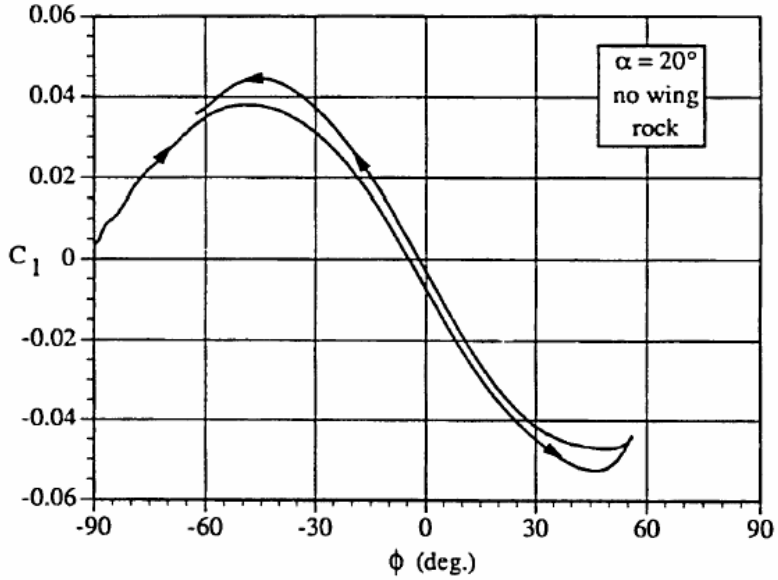

Figure 1-11 Rolling moment coefficient vs. roll angle cycle for a wing pitch angle where there is no wing rock. Figure reprinted from [46] by permission of the author.

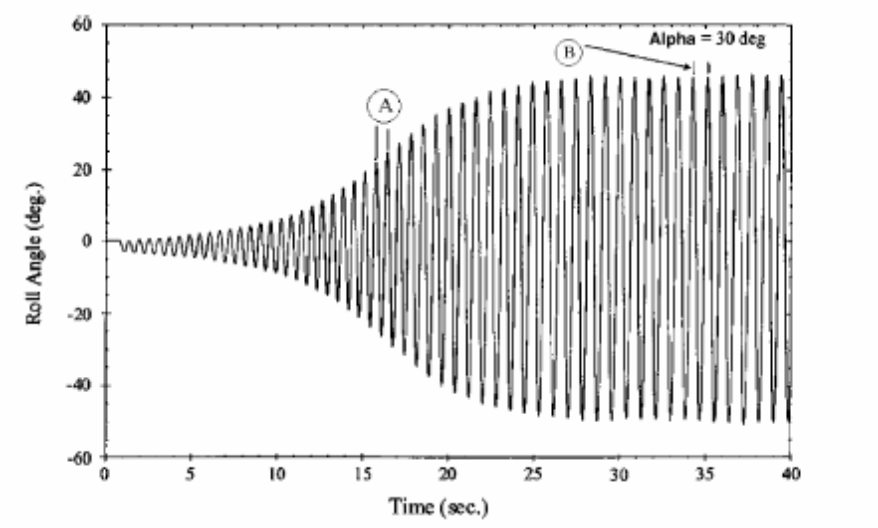

Figure 1-12 Time history of wing rock buildup in free to roll tests at wing pitch angle equal 30 deg. Figure reproduced from [46] by permission of the author.

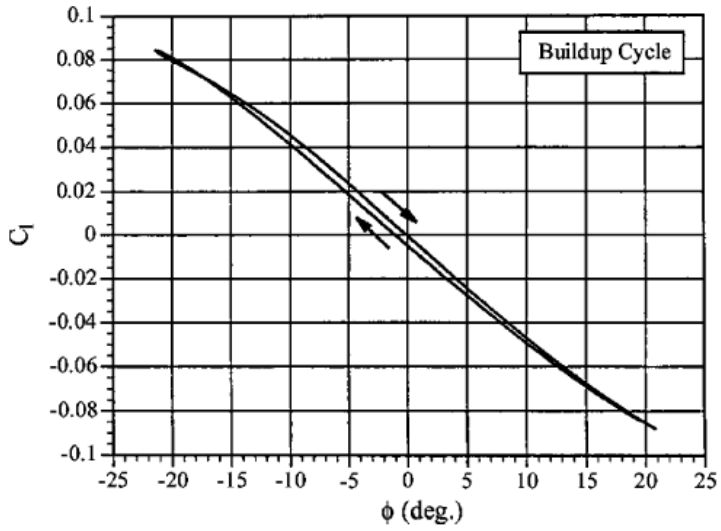

Figure 1-13 Rolling moment coefficient for a cycle of wing rock buildup. Figure reproduced from [46] by permission of the author.

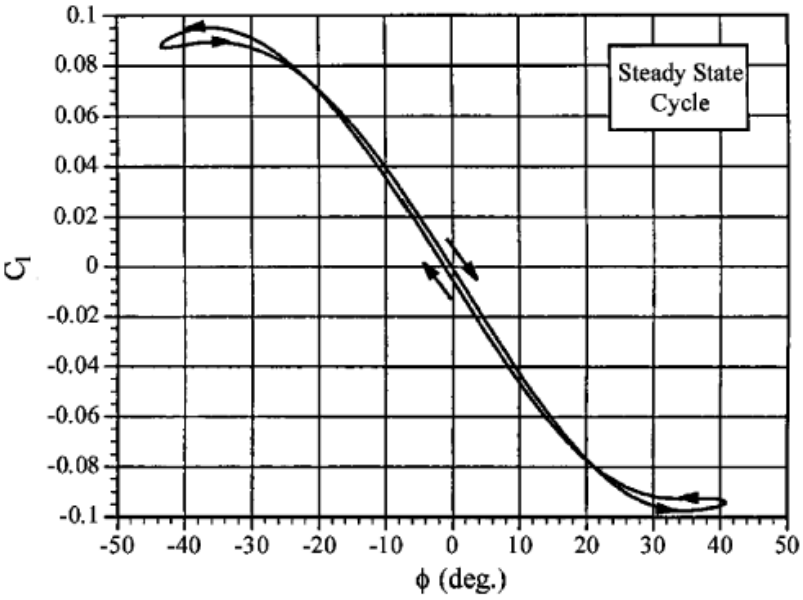

Figure 1-14 Rolling moment coefficient for a steady state cycle of wing rock. Figure reprinted from [46] by permission of the author.

1.2.2 Experimental Investigations on the Slender Delta Wings

This is a brief review of the references where unsteady aerodynamic measurements and wing rock motion data were taken and used to identify unsteady aerodynamic models investigated along the same lines as this research. As previously mentioned, the principal source of wing rock is the lifting surfaces. Furthermore, some of the aircraft unsteady aerodynamic models investigated here are a composition of basic aerodynamic models that represent the unsteady aerodynamic behavior of each of the lifting surfaces. Since these models include internal state variables that describe the flow characteristics, their construction is heavily based on observations made on the available experimental data. Most of the published experimental data is for slender delta wings. Also, because the most susceptible configurations to wing rock have highly swept planforms or strakes that produce vortical flows during excursions into the high angle-of-attack regime, it is

thought that the mechanisms which are present in the wing rock of slender delta wings will also be the dominant effects in the wing rock of complete aircraft configurations. Thus we focus our attention on this kind of lifting surface.

The experimental work done by Nguyen, Yip, and Chambers [45] at NASA Langley provides data that helps us understand the fundamental flow mechanisms causing wing rock for slender delta wing configurations. This experimental work also led to the *Energy Exchange Concept*, described in Section 1.2.1, which is important to the current work. The data published in that reference for the slender delta wing free-to-roll dynamic tests are used here to identify the model parameters of the investigated formulations. As discussed in Section 1.2.1, analysis of the motions obtained in the free-to-roll tests were made by the analysis of the measured roll angle data. Nguyen *et al.* were able to derive an estimate of the roll acceleration by fitting a smoothing cubic spline to the roll angle time history data points, thus eliminating high frequency noise. With the roll acceleration determined, an estimate of the total aerodynamic rolling-moment coefficient was derived through Eq. (1-35). With the roll angle and the total aerodynamic time-histories, Nguyen et al were able to plot the $C_l \times \phi$ loops for the angles of attack equal to 27 and 32 degrees, as shown in Figures 1-15 and 1-16 and used in this research to identify parameters associated with the dynamic behavior.

Levin and Katz [47] have also conducted free to roll tests on 76 and 80 degree swept delta wings. Only the delta wing with a sweep angle equal to 80 degrees and an aspect ratio of 0.71 (root chord = 0.4285 m, span = 0.150 m) demonstrated wing rock in the free to roll tests documented in that reference. In their experiments, static force and moment data were obtained. The corresponding experimental results for the static tests, shown in Figure 1-17 and Figure 1-18 for roll angles of 0, 10, 20 and 30 degrees, and for an airspeed of 14 m/s, helped to identify the unsteady aerodynamic model parameters associated with the static behavior of the model investigated in this research. Concerning the dynamic data, Levin and Katz obtained time histories of the roll angle, and of the lateral and normal force coefficients. However, they were not able to acquire experimental values for the rolling moment coefficients.

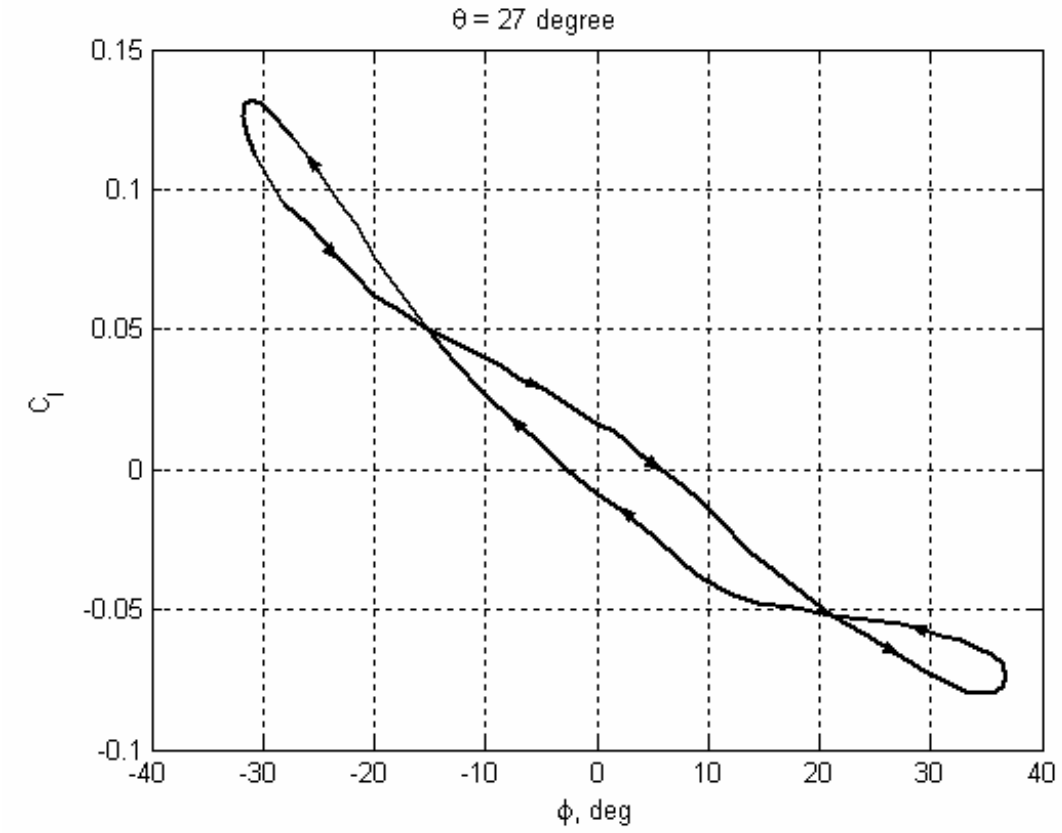

Figure 1-15 C_l vs. roll angle histogram for one cycle of wing rock at θ_0 = 27 degree . Data extracted from [45].

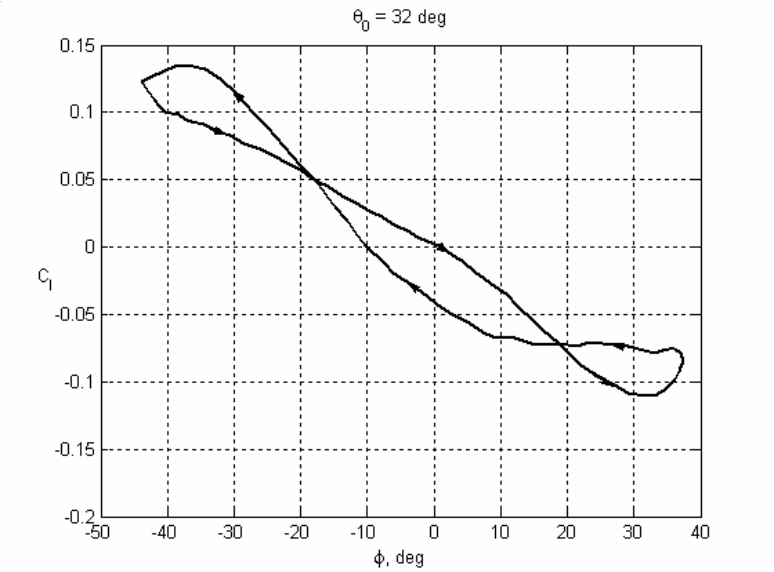

Figure 1-16 C_l vs. roll angle histogram for one cycle of wing rock at θ_0 = 32 degree. Data extracted from [45].

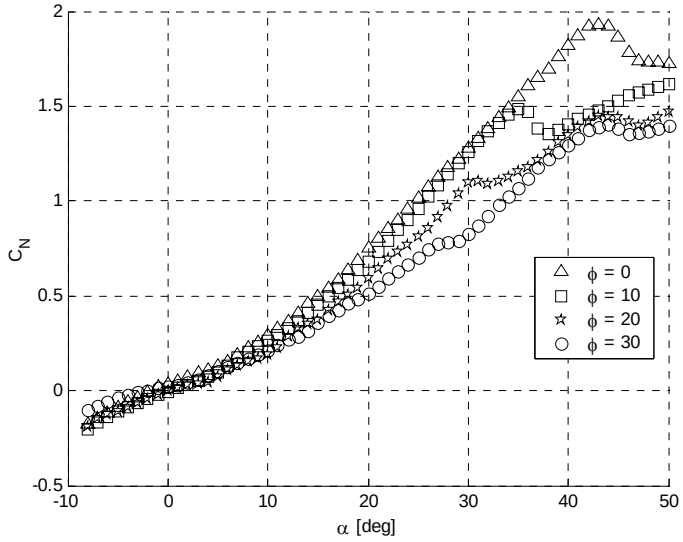

Figure 1-17 Normal force coefficient in balance coordinates *vs*. pitch angle – results from static tests. Data extracted from [47].

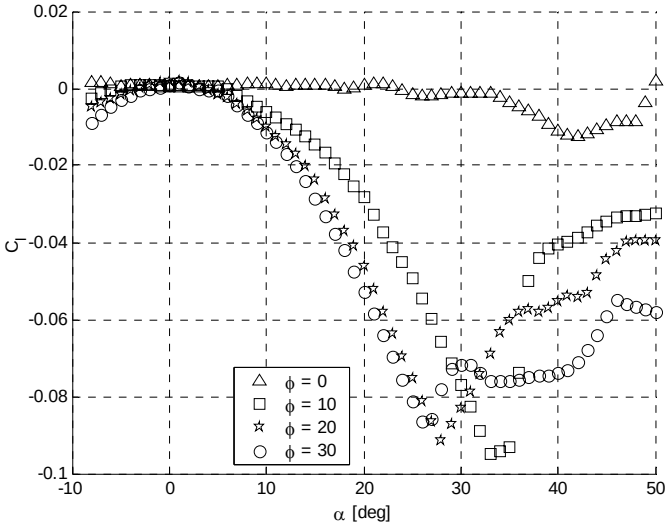

Figure 1-18 Rolling moment vs. pitch angle – results from static tests. Data extracted from [47].

Another reference that contains experimental data useful in the identification of the basic unsteady aerodynamic models investigated here is the one written by Arena [46]. The primary goal of that experimental investigation was to document motion history and flow field behavior on a slender delta wing undergoing wing rock to identify mechanisms that may be responsible for wing rock. Two delta wing models with a leading edge sweep angle of 80 degree were used. One of them was used for flow visualization and free-to-roll time histories determination. The other was instrumented for the steady and unsteady measurement of surface pressure. The main features of the experimental apparatus were the air bearings and the modular optical encoder, installed with the purpose of having a single degree of freedom motion with little friction from the bearing or from roll angle acquisition. The work documented the angle of attack range where wing rock exists for this particular wing, at a Reynolds number of 400,000. Inside that range, initial angles of attack were chosen to represent damped motion ($\alpha = 20°$) and limit cycle wing rock ($\alpha = 30°$). The corresponding rolling moment coefficient *vs*. roll angle loops are

reproduced here in Figure 1-11 and Figure 1-14, respectively. The measurement of the rolling moment acting on the wing was possible by finite differencing the motion history of the wing. In order to have further insight into how the surface pressure creates the rolling moment, a motion control system was developed to guide the model through the wing rock time histories obtained in the free to roll experiments. The steady and unsteady flow visualization of vortex trajectories allowed measurements of the vortex core location for the wing undergoing wing rock, reproduced in Figure 1-19 for the chord location of 75%, providing the vortex positions above a slender delta wing as a function of the roll angle during wing rock motion, and helped to shape the internal state equations of some of the unsteady aerodynamic models proposed and investigated here. The coordinate system used to give the positions of the vortex cores is shown in Figure 1-20. It was found that vortex breakdown is not a primary mechanism involved in the slender-wing rock motion, since it is not seen on the wing over a large range of angles of attack at which wing rock occurs. But when it occurs over the model, additional damping is added which results both in an overall reduction in the wing rock amplitude and in a jump in the reduced frequency. However the author stated that it is just an additional contribution to the damping and not one of the primary mechanisms responsible for the occurrence of the wing rock.

The geometrical and physical differences between the wing models and experimental apparatus used in the tests published in [45], [46], and [47] are summarized in Table 1-1. The wings were fixed to the sting in different ways. The free to roll apparatus used by Nguyen, Yip, and Chambers [45] had its bearings and the potentiometer used to measure the roll angle located beneath the wing. This caused the center of rotation of the model to be two inches below the longitudinal axis of the wing. A sketch of this apparatus is shown on Figure 1-21. Levin and Katz managed to mount the bearings and potentiometer on the wing centerline. This caused the wing to have a relatively large center body hump, as shown in Figure 1-22.

1.2.3 Analytical and Computational Investigations on the Wing Rock

Konstadinopoulos, Mook, and Nayfeh [53] numerically reproduced the slender delta wing wind tunnel tests whose results were published in [45], [47]. They used an unsteady vortex-lattice method (UVLM) to provide the aerodynamic loads and integrated the single degree-of-freedom equation of motion using a predictor-corrector scheme. The UVLM was coupled with the equation of motion and both the motion and the flow field were predicted interactively. Their simulations considered the geometrical and physical differences between the experimental apparatus used in both tests, as well as the damping due to the friction in the bearings of the stings. Simulations were done for the case where the axis of rotation was below the centerline of the wing, reproducing the arrangement used by Nguyen et al [45] in their tests, and also for the case where the axis of rotation was on the centerline, as in the experiments reported in [47]. An analytical representation of the rolling moment was developed to help the understanding of the wing rock dynamics. In this representation, the rolling moment is represented by the expansion in terms of angle of roll ϕ and roll rate $\dot{\phi}$ given by Eq. (1-38).

$$C_l\left(\phi,\dot{\phi}\right) = a_1\phi + a_2\dot{\phi} + a_3\phi^3 + a_4\phi^2\dot{\phi} + a_5\dot{\phi}^2\phi + a_6\dot{\phi}^3 + a_7\phi^5 + a_8\phi^4\dot{\phi} + a_9\phi^2\dot{\phi}^3 + a_{10}\dot{\phi}^2\phi^3 + a_{11}\phi^4\dot{\phi} + a_{12}\dot{\phi}^5 \quad \textbf{(1-38)}$$

In Eq. (1-38), the coefficients a_i were determined by a least-squares fit with the numerical results found with the help of the UVLM. Since the curves of the rolling moment coefficient C_l vs. angle of roll ϕ change with the angle of attack, so do their coefficients. It was observed that some of the terms in Eq. (1-38) make virtually no contribution and their coefficients can be set equal to zero. This is the case for the coefficients $a_8, a_9, a_{10}, a_{11}, a_{12}$. The simulations showed that when the angle of attack exceeds a critical value, the limit cycle develops after a small perturbation in roll. The UVLM is limited to angles of attack for which vortex bursting does not occur and to situations in which separation occurs only along the edges.

Later, the nonlinear analysis of Eq. (1-38) was carried out in [54]. The analytical result was used to construct phase planes by using the method of multiple scales, and the global nature of the wing rock was revealed through stable limit cycles, unstable foci, saddle points, and domains of initial conditions that lead either to sustained oscillatory motion, divergence or damping.

In addition to his experimental work, summarized here in Section 1.2.2, Arena [46] investigated the steady and unsteady behavior of delta wings in roll also with the development of a computational model since there were certain aspects of the flow field that could not be revealed with the experimental apparatus. For example, it was not possible to measure the unsteady behavior of vortex strength during wing rock. His computational model represented the separated flow field above the wing as a system of two discrete vortices in an inviscid flow. The position and strength of each vortex was captured by the formulation of specific boundary conditions. The idea was to use this computational model to capture the primary mechanisms responsible for wing rock that had not been captured during the wind tunnel tests, such as the vortex strength influence. According to Arena's conclusions in [46], vortex strength hysteresis on the downward wing contributes with a rolling moment that opposes the direction of rotation and helps to stabilize the wing at the higher values of the roll angle.

Saad [55] numerically simulated three degree of freedom wing rock motion through the flow solver code *fdl3di*: roll, sideslip and vertical motion. The results were obtained for a generic fighter model consisting of fore-body, cropped delta wing and vertical fin. Until then, wing rock numerical simulations had been limited to a single degree of freedom in roll and applied to simple delta-wing configurations. He studied the additional effects of sideslip and vertical motion, as well the effect of adding the vertical fin. The effect of adding the sideslip and vertical motion degrees of freedom to the simulations of the wing-body configuration were found to delay the onset and to reduce the amplitude of wing rock by about 50% with no change in frequency. The aerodynamic effect of the fin was found to delay the vortex burst on the upper surface of the wing. As a net result of the

vertical fin inclusion, the oscillations were more damped, with significant increase in frequency.

1.3 Overview of the Thesis

The goal of the current research is to investigate functional, unsteady aerodynamic models with a state-space representation that could be coupled to the equations of motion to simulate wing rock. To achieve these goals, we insert modifications into an existing basic unsteady aerodynamic formulation and identify its parameters using published experimental data for slender delta wings. Since the identification results obtained with the pre-existing formulation are not satisfactory, we first develop a basic unsteady aerodynamic model that is capable of accounting for the static hysteresis phenomenon. Then, we add additional internal state variables representing both the spanwise and vertical motion of the vortex core, which account for the sideslip and roll angle on the lifting surface normal force. Next, we apply this model to each one of the lifting surfaces or panels in which the aircraft is split, and investigate its ability to represent the wing rock phenomenon. The unsteady aerodynamic model is finally coupled to the equations of motion to perform simulations of the wing rock phenomenon.

The proposed models are described in Ch. 2. The identifications of their model parameters are shown in Ch. 3. Chapter 4 presents the simulations done with the models that were identified. Some final comments and conclusions are presented in Chapter 5.

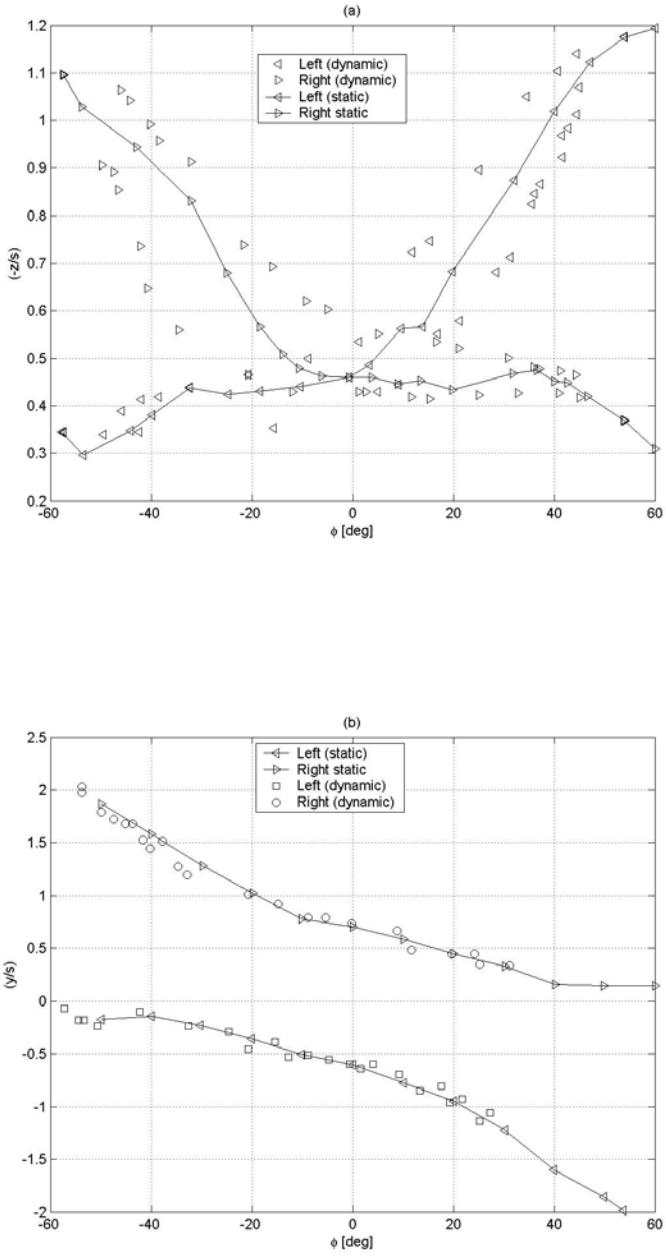

Figure 1-19 Vertical and spanwise vortex positions during wing rock. Data extracted from [46]. (a) Vertical position. (b) Spanwise position.

Table 1-1 Geometrical and physical parameters of some tested slender delta wings.

	Wing 1 [45]	Wing 2 [47]	Wing 3 [46]
root chord c_r, m	1.765	0.4285	0.422
planform area S, m^2	0.5491	0.0321	0.0314
span b, m	0.622	0.150	0.149
rolling moment of inertia I_{xx}, kg m^2	9.18×10^{-2}	2.7×10^{-4}	1.13×10^{-3}
ρ, kg/m^3	1.187	1.2	1.2
V_∞, m/s	9.266	15	13.8

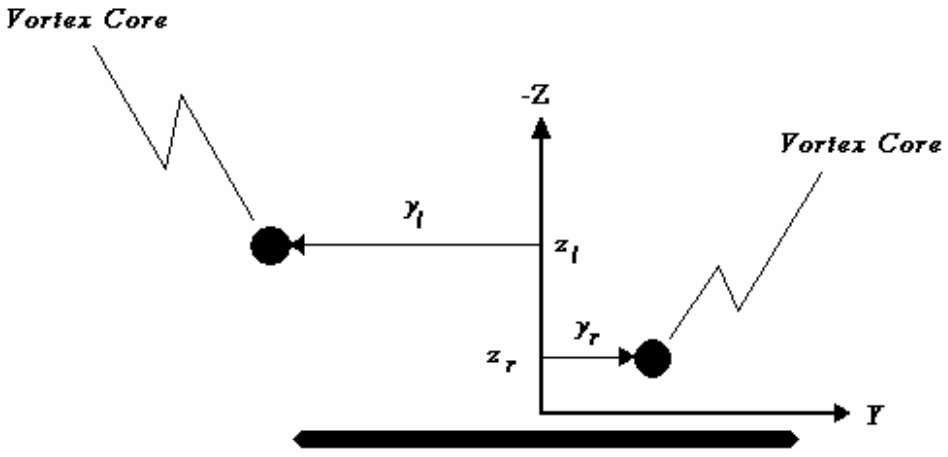

Figure 1-20 Sketch of asymmetric vortex position – rear view. Figure reprinted from [46] by permission of the author.

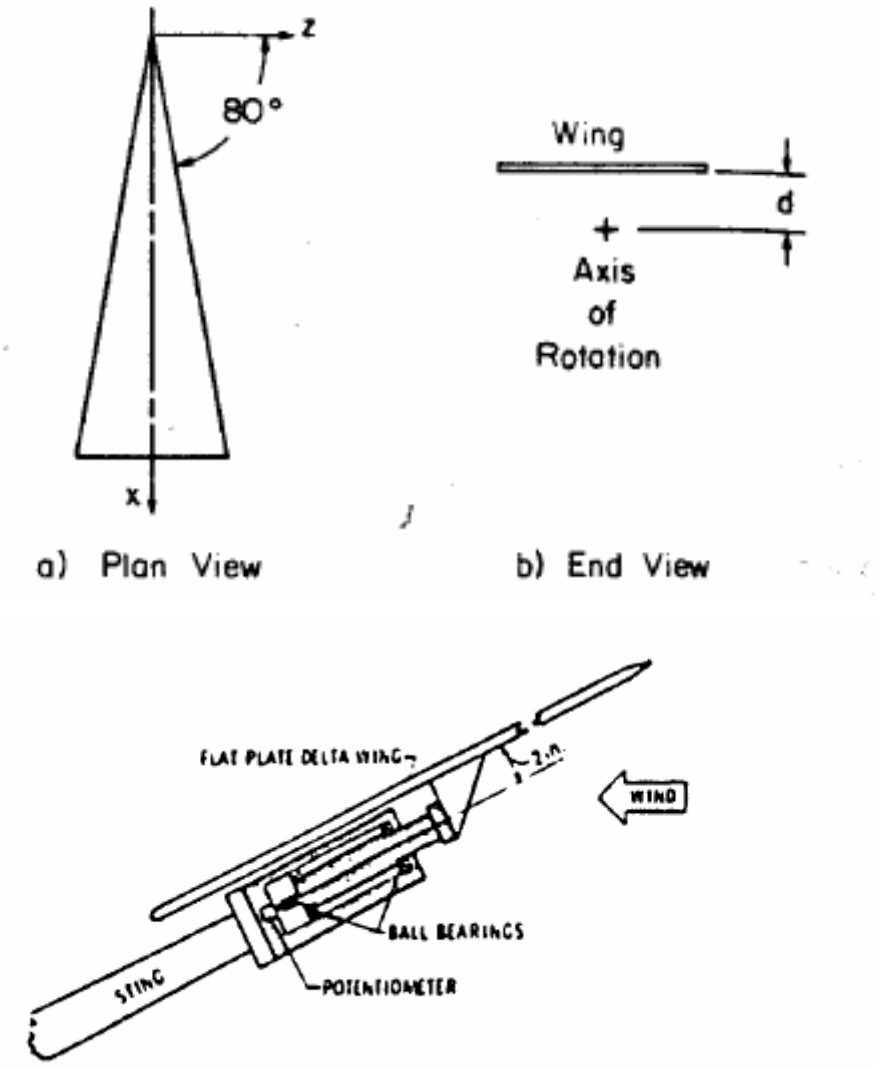

Figure 1-21 Free to roll apparatus used by Nguyen, Yip, and Chambers. Figure reprinted from [45] by permission of the American Institute of Aeronautics and Astronautics, Inc.

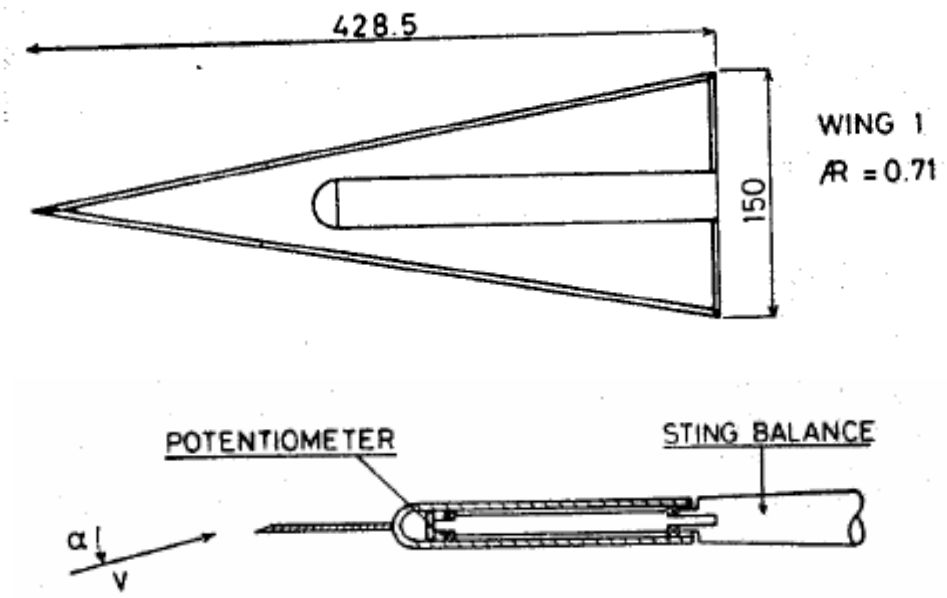

Figure 1-22 Free to roll apparatus used by Levin and Katz [47]. Figure reprinted by permission of the American Institute of Aeronautics and Astronautics, Inc.

2 The Investigated Unsteady Aerodynamic Models

Unsteady aerodynamic effects at high angles of attack resulting from separated and vortex flow development can significantly alter the aerodynamic loads with respect to their conventional representation. In the conventional approach, the unsteady effects are described using linear terms with unsteady aerodynamic derivatives. Nevertheless, there are special regions of incidence, e.g. $C_{L\max}$, where the conventional representation is not valid. Since in unsteady flight conditions the aerodynamic forces and moments are time and motion history dependent, a dynamic model is needed for the development of a valid description. The special approaches using the differential equations that have been proposed can improve the aerodynamic model and take into account the nonlinear unsteady aerodynamic effects due to separated and vortex flow dynamics. A basic state-space model with state-space representation was studied in refs. [30], [32], [34], after the ideas of Goman and Khrabrov proposed in [29]. This general concept was described in Section 1.1.3. Fan and Lutze proposed in [30], [34] a variation of this model, and some of their contributions are mentioned in Section 1.1.3, as well. As a difference to the Goman and Khrabrov version, the variation proposed by Fan and Lutze uses the distance between the wing trailing edge and the separation point as the internal state variable, instead of the distance between wing leading edge and the separation point used by the Russian authors. The reason behind this choice was to have aerodynamic coefficients at low angles of attack independent of the internal state variable. That made this model more consistent with the conventional approach. De Oliveira and Lutze [32] added to this formulation an improvement that allows it to represent static hysteresis. The description of this improvement was described in Section 1.1.5.

The application of the exact original state-space model to the rolling delta wing has some problems. One of them is that the separation point has different values for each of the side of the wing, and consequently so does the internal state variable. Another problem is that the angles of attack are different for each side of the wing when the wing is rolling.

Both of these problems make it difficult to use only one output equation to determine each aerodynamic coefficient. In a tentative approach to address the unsteady aerodynamic characteristics in multiple axes, Stagg and Lutze [39],[40] proposed dividing the airplane lifting surfaces into separate panels, and applied the basic state-space model to characterize the unsteady aerodynamics of each one of them in the way described on Section 1.1.6. Here this panel formulation describing the unsteady aerodynamic characteristics of the aircraft in multiple axes is composed with some proposed basic unsteady aerodynamic models and investigated. The investigation starts with a model whose improvements over the original Stagg and Lutze model allows it to match some influences of the roll (or the sideslip) angle. Also, the basic unsteady aerodynamic model used in each panel is that described in Section 1.1.5, which is improved to represent static hysteresis. The second model investigated has some further modifications, for example, the addition of both the roll angle as an input variable, and of two internal state variables.

Since the acquisition of wind tunnel experimental data was not part of this research, all the investigated models have their parameters identified with data available for slender delta wings taken from published references. The slender delta wing geometries and the data used to identify the model parameters are described in Section 3.2.

2.1 The First Unsteady Aerodynamic Model Investigated

The original state-space model was found to have good performance in describing the unsteady aerodynamics of the airplane when considered as a single lifting surface up to high angles of attack [29], [30], [34]. Nevertheless, this good performance was observed only for longitudinal motion, in which the only motion variable was the angle of attack. Trying to take advantage of the state-space formulation to find the simplest model that could describe the unsteady aerodynamics of the whole airplane in multiple axis, Stagg and Lutze [39],[40] proposed dividing the airplane into panels that represent lifting surfaces, and applied the basic state-space model presented in [30], [34] to characterize the unsteady aerodynamics of each one of them in the way described in Section 1.1.6. When the rolling moment coefficient was plotted against the sideslip angle in [39] for the

F-18 forced to oscillate in roll at pitch angle equal to 30 degrees with amplitude of 20 degrees and a frequency of 1 Hz, the result is shown in Figure 2-1, where the arrows indicate direction in time. Comparing it to Figure 1-9, we can see that, according to the *Energy Exchange Concept* [45] described in Section 1.2.1, this model would not undergo limit cycle oscillations if the F-18 model was left free to rotate. Another try was made here to verify if a model based on this formulation could simulate wing rock by adding some improvements and identifying its parameters with the help of simulated experimental data.

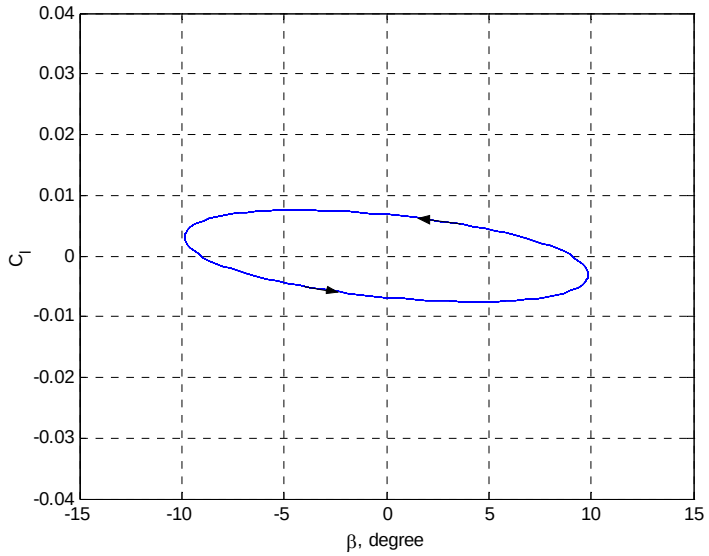

Figure 2-1 Roll coeficient *versus* sideslip angle for the F-18

Considering Figure 1-17, we notice that there is a different C_N *vs.* α curve for each value of the roll angle, and they have not only different slopes but also different angles of stall. One of the reasons for the different slopes is because the wing normal coefficient C_N values shown in Figure 1-17 are represented in balance coordinates. That means that, because the wind tunnel balance used to take the experimental values of the delta wing normal coefficient C_N recorded only the vertical component, then to be compared to the

experimental results the values of the wing normal coefficient in body axes C_N have to be converted to the normal coefficient in balance coordinates $(C_N)_{bal}$ through Eq. (2-1) below:

$$(C_N)_{bal} = C_N \cos\phi \qquad \textbf{(2-1)}$$

where ϕ is the roll angle and C_N is the wing total normal coefficient in body axes.
Another possible reason for the slopes of the C_N *vs.* α curve being different for each value of the roll angle could be the wing aerodynamic characteristics variation with the sideslip angle.

When the multi-axis state-space representation (see Section 1.1.6) is applied to the slender delta wing configuration, it is split into two lifting panels: left and right semi-wings, so we drop the subscript "*w*". Since this type of configuration has not tails, the number of parameters to be identified is less than the one corresponding to a conventional aircraft. In the present case, we have four unknowns: the left and right normal force coefficients and moment arms. Also reduced in number are the equations used: in the static case we have just one normal force equation like the first term of (1-30), and the rolling moment equation (1-33). There still is the dynamic relationship that we assumed between the normal forces on left and right wings (1-18), and the number of unknowns is reduced to three.

Comparing Eq. (1-33) with Figure 1-18 one can notice that, when applied to that wing-alone configuration, the original Stagg formulation does not have flexibility to account for the variation of the rolling moment coefficient static values with the angle of attack and with the roll angle variations. This happens because, in the multi-axis original formulation, the lateral arm y_w has the same value for left and right wings. Also, in the static case, the normal force coefficient static values on both wings are the same because the angles of attack on both left and right wings have the same values. Consequently, if it was calculated through that formulation, the static responses of the rolling moment coefficient would be zero for all values of the roll angle and the original model will never

match the experimental data. To add more flexibility to Stagg's formulation, we define, as additional model parameters, the set containing one different parameter for each of the left and right wing lateral arms y_{wl}, y_{wr} , free to vary with the roll angle (see Table 3-1). The results of the identification done for this first improvement to the Stagg's formulation only using static experimental values, and are shown on Figure 2-2 and Figure 2-3. This parameter identification was done by a least –squares fit between the calculated values of the normal force and rolling moment coefficients and the experimental data taken from reference [47]. More details about the parameter identification can be seen in Chapter 3. Figure 2-4 shows the variation of the identified wing lateral arms with the roll angle. We see in Figure 2-2 and Figure 2-3 that the experimental values of the angle of stall change with the roll angle. The original formulation does not have the flexibility to account for that either. Trying to improve still further the match between the model responses and the experimental data, we let the parameters α^* and σ vary with the roll angle such that there is one different identified value of each parameter per roll angle value (see Table 3-1). Finally, the series expansion of C_N in α and $\dot{\alpha}$ in Eq. (1-18) is also increased to a higher order in Eq. (2-5), due to the high nonlinearity exhibited by the experimental data. After adding these modifications, the first unsteady aerodynamic model for the slender delta wing to be investigated is obtained and summarized through Eqs. 2-2 to 2-7. The notation used is similar to that of Section 1.1.6.

► State equations:

$$\tau_{1,x}\frac{d\bar{x}_i}{dt}+\bar{x}_i=\bar{x}_0\left(\alpha_i-\tau_{2,\alpha}\dot{\alpha}_i\right) \tag{2-2}$$

► Output equations:

$$C_N=C_{N,l}+C_{N,r} \tag{2-3}$$

$$C_l=C_{Nl}\frac{|y_l|}{b}-C_{Nr}\frac{|y_r|}{b}=C_{Nl}\bar{y}_l-C_{Nr}\bar{y}_r\,, \tag{2-4}$$

where

$$C_{Ni}=C_{N0}+C_{N\alpha}\ (\bar{x}_i)\alpha_i+C_{N\alpha^2}(\bar{x}_i)\alpha_i^2+C_{N\hat{\dot{\alpha}}}(\bar{x}_i)\hat{\dot{\alpha}}_i+C_{N\hat{\dot{\alpha}}^2}(\bar{x}_i)\hat{\dot{\alpha}}_i^2+C_{N\alpha\hat{\dot{\alpha}}}(\bar{x}_i)\alpha_i\hat{\dot{\alpha}}_i \tag{2-5}$$

with $i = l$ (left), r (right) panel, and $\hat{\dot{\alpha}}=\dot{\alpha}\,\hat{t}$.

The spanwise positions $\bar{y}_l$, $\bar{y}_r$ of the normal force point of application, the sigmoid location angle of attack α^* and the slope σ are made functions of the roll angle. The remaining functions and parameters for this formulation are:

$$\bar{x}_0(\alpha_i) = \frac{1}{1+\exp\left(-\sigma\ (\alpha_i - \alpha^*)\right)} \qquad \textbf{(2-6)}$$

$$C_{N\alpha}(\bar{x}_i) = a_1 + b_1\ \bar{x}_i + c_1\ \bar{x}_i^2$$

$$C_{N\alpha^2}(\bar{x}_i) = a_2 + b_2\ \bar{x}_i + c_2\ \bar{x}_i^2$$

$$C_{N\hat{\alpha}}(\bar{x}_i) = a_3 + b_3\ \bar{x}_i + c_3\ \bar{x}_i^2 \qquad \textbf{(2-7)}$$

$$C_{N\hat{\alpha}^2}(\bar{x}_i) = a_4 + b_4\ \bar{x}_i + c_4\ \bar{x}_i^2$$

$$C_{N\alpha\hat{\alpha}}(\bar{x}_i) = a_5 + b_5\ \bar{x}_i + c_5\ \bar{x}_i^2$$

The parameters of this formulation that must be identified are:

- the polynomial coefficients C_{N0}, a_i, b_i, c_i of Eqs. (2-7);
- transient time-constant $\tau_{1,x}$ and time-delay constant $\tau_{2,\alpha}$ of Eq. (2-2), functions of the wing pitch angle θ_0 at which the dynamic experimental data are obtained;
- the parameters α^* and σ of the logistic equation (2-6) that represent the static position of the vortex breakdown over the panel. They are left free to vary with the roll angle at which the static experimental data was obtained and, therefore, there are one of each of these parameters for each static experimental value of the roll angle;
- the normal force arms y_l, y_r, which are also varying with the roll angle at which the static experimental data are obtained.

The identification of these parameters is described in further detail in Section 3.3.

As shown in Figures 3-4 to 3-9, the responses obtained for this, the first model investigated did not match the experimental data very well. Because of that, a second unsteady aerodynamic model was developed. Next, we present its description.

2.2 The Second Unsteady Aerodynamic Model Investigated

As shown in Section 1.2.1, for the wing rock limit-cycle oscillations to occur, the rolling moment coefficient must laterally destabilize the wing at small roll angles and stabilize it at larger values. The fluid mechanism that does this and sustains the limit-cycle oscillations involves a time lag in the vortex core position and strength. In this second model to investigate, we propose to match these effects with a basic unsteady aerodynamic model that represents the variation of the panel normal lifting forces with the strength and vertical position of the vortex core vertical position as a function of the roll angle. Therefore, in this formulation, the panel normal lifting forces are modeled to be functions of both the angle of attack and the roll angle. Since the wing rock oscillations of this type of configuration are strongly related to the movement of the leading edge vortices, we try to find these functions by assuming that the points of application of the panel normal lifting forces coincide with the vortex core positions. The spanwise non-dimensional body-axes coordinates $\bar{y}_i(t)$ are also taken as internal flow state variables, in addition to the chordwise coordinates $\bar{x}_i(t)$, associated with the region of the separated flow. A third type $\bar{v}_i(t)$ of state variable, associated with the effects of both the vortex strength and vortex core vertical position, is also added to the system. The basic unsteady aerodynamic model proposed here is, in its most general form, composed of the state equations of the above mentioned state variables and the output (or observer) equations that give the values of the airplane rolling moment and normal force coefficients. The airplane force coefficients are the summation of the coefficients of each lifting surface panel that represents the airplane. The state equations are the first-order differential equations (2-8) to (2-10) whose above mentioned dependent variables $\bar{x}_i(t)$, $\bar{y}_i(t)$, and $\bar{v}_i(t)$ represent the system dynamics. Equations (2-11) and (2-12) are the output equations. The input variables are the kinematic motion parameters, also called *motion variables*: the panel local angle of attack $\alpha_i(t)$, the airplane roll angle $\phi(t)$, and their respective time derivatives $\dot{\alpha}_i(t)$, $\dot{\phi}(t)$. For convenience, the roll angle $\phi(t)$ is chosen as the second motion variable instead of $\beta_i(t)$ because all the experimental data

used to find the model parameters were published as a function of $\phi(t)$. For each fixed value of the wing pitch angle θ_0, the local sideslip angle time history $\beta_i(t)$ can be determined through $\phi(t)$ and $\alpha_i(t)$ time-histories by using Eqs. (1-22) and (1-28), derived in Appendix A.2. However, for a general type of motion where the pitch angle is not fixed, those relations are no longer valid.

In this postulated model, the equations used to represent the unsteady aerodynamics for general flight conditions in each panel of the airplane are:

$$\frac{d\bar{x}_i(t)}{dt} = f_{1,i}(\alpha_i, \dot{\alpha}_i) \tag{2-8}$$

$$\frac{d\bar{y}_i(t)}{dt} = f_{2,i}(\phi, \dot{\phi}) \tag{2-9}$$

$$\frac{d\bar{v}_i(t)}{dt} = f_{3,i}(\phi, \dot{\phi}) \tag{2-10}$$

$$C_{N,i} = g(\bar{x}_i, \bar{y}_i, \alpha_i, \dot{\alpha}_i, \phi, \dot{\phi}) \tag{2-11}$$

where the subscript *i* stands for each lifting panel, i.e., *i = l (left) , r (right)*.
The value of the normal force coefficient for the whole slender delta wing is found also through Eq. (2-3).

As shown in Section 1.1.6, we can calculate the rolling moment coefficient for the aircraft through Eq. (1-33), which in the particular case of the slender delta wing reduces to:

$$C_l = C_{Nl}|\bar{y}_l(\phi)| - C_{Nr}|\bar{y}_r(\phi)| \tag{2-12}$$

where $\bar{y}_{(\bullet)}$ are the non-dimensional arms of the normal force coefficient with respect to the longitudinal body axis, given by Eq. (2-9).

With the help of the formulation described in Section 1.1.5, the system composed by the Eqs. (2-8), (2-9), (2-10), and (2-11) results in the following equations:

$$\tau_{1x}\frac{d\bar{x}_i}{dt}+\bar{x}_i=U_\alpha\bar{x}_{0,U}\left(\alpha_{eff,i}\right)+D_\alpha\bar{x}_{0,D}\left(\alpha_{eff,i}\right) \quad \textbf{(2-13)}$$

$$\tau_{1y}\frac{d\bar{y}_i}{dt}+\bar{y}_i=U_\phi\bar{y}_{0,i,U}\left(\phi_{eff}\right)+D_\phi\bar{y}_{0,i,D}\left(\phi_{eff}\right) \quad \textbf{(2-14)}$$

$$\tau_{1v}\frac{d\bar{v}_i}{dt}+\bar{v}_i=U_\phi\bar{v}_{0,i,U}\left(\phi_{eff}\right)+D_\phi\bar{v}_{0,i,D}\left(\phi_{eff}\right) \quad \textbf{(2-15)}$$

$$C_{N,i}=C_{N,i}\left(\bar{x}_i,\alpha_i\right)+\Delta C_{N,i}\left(\bar{v}_i,\phi\right) \quad \textbf{(2-16)}$$

We do this because we want this model to be capable of representing static hysteresis, whenever it occurs. Equation (2-13) is the same as Eq. (1-12), that is,

$$U_\alpha\overset{\Delta}{=}\frac{1+sign\left(\Delta\alpha\right)}{2} \quad \textbf{(2-17)}$$

$$D_\alpha\overset{\Delta}{=}\frac{1-sign\left(\Delta\alpha\right)}{2} \quad \textbf{(2-18)}$$

with $\Delta\alpha=\alpha_{j+1}-\alpha_j$ for the given sequence of the static angles of attack α_j, j = 1,2,…,l, or $\Delta\alpha=\alpha\left(t_{j+1}\right)-\alpha\left(t_j\right)$ for the given time histories of angles of attack $\left\{\alpha\left(t_j\right),0\le t_j\le t_n\right\}$ in the considered panel. The static dependence between the internal state variable $\bar{x}_i$ and the angle of attack are determined for the up (U) and down (D) direction by

$$\bar{x}_{0U}=\frac{1}{1+\exp\left[-\sigma_{x,U}\left(\alpha_{eff,i}-\alpha_U^*\right)\right]} \quad \textbf{(2-19)}$$

$$\bar{x}_{0D}=\frac{1}{1+\exp\left[-\sigma_{x,D}\left(\alpha_{eff,i}-\alpha_D^*\right)\right]} \quad \textbf{(2-20)}$$

Since all the effects due to the sideslip or to the roll angle are now included in the term $\Delta C_{N,i}(\phi)$ of Eq. (2-16), the parameters $\alpha^*_{(\bullet)}$ and $\sigma_{x,(\bullet)}$ related to the localization and shape of the sigmoids given by Eqs. (2-19) and (2-20) are not let free to vary with the roll angle in this case. The values of α_{eff} are determined through the equation

$$\alpha_{eff,i} = \alpha_i - \tau_{2,\alpha}\dot{\alpha}_i \qquad \textbf{(2-21)}$$

with $\tau_{2,\alpha}$ being a time-delay constant related to the vortex burst location. Equation (2-14) is similar in structure to (2-13), and its nomenclature is given as follows,

τ_{1y} = the transient time-constant related to the vortices core spanwise displacement.

$\bar{y}_i = \dfrac{y_i}{b}$ = non-dimensional distance between the panel normal lifting force point of application and the longitudinal axis.

$$U_\phi \overset{\Delta}{=} \frac{1 + sign(\Delta\phi)}{2} \qquad \textbf{(2-22)}$$

$$D_\phi \overset{\Delta}{=} \frac{1 - sign(\Delta\phi)}{2} \qquad \textbf{(2-23)}$$

with $\Delta\phi = \phi_{j+1} - \phi_j$ or $\Delta\phi = \phi(t_{j+1}) - \phi(t_j)$ respectively in the quasi-static and in the dynamic cases, where, in the quasi-static case, the given sequence of the static roll angles is ϕ_j, j = 1,2,…,l, and where $\Delta\phi = \phi(t_{i+1}) - \phi(t_i)$ for the given time histories of roll angles $\{\phi(t_i), 0 \le t_i \le t_n\}$. The time-delay effects on the vortex movements due to the roll angle are taken into account through

$$\phi_{eff} = \phi - \tau_{2,\phi}\dot{\phi}, \qquad \textbf{(2-24)}$$

where $\tau_{2,\phi}$ is a time-delay constant related to the vortex core position, to be found from wind tunnel data.

Since the vortex strength and vertical core position effects are considered to be lumped into Eq. (2-15), we want the state variables $\bar{y}_i$ to behave qualitatively like the wind

tunnel tests results shown in Figure 1-19. That means that $\bar{y}_i$ must get smaller for the panel that is going down. Because of that, the logistic functions that compose the right-hand-side of (2-14) are built as follows,

$$\bar{y}_{0,i,U}(\phi) = \frac{1}{1+\exp\left[\xi_i \sigma_{y,i,U}\left(\phi - \phi^*_{y,i,U}\right)\right]} \tag{2-25}$$

$$\bar{y}_{0,i,D}(\phi) = \frac{1}{1+\exp\left[\xi_i \sigma_{y,i,D}\left(\phi - \phi^*_{y,i,D}\right)\right]} \tag{2-26}$$

where $\xi_l = -1$ and $\xi_r = 1$ respectively for left (i = l) and right (i = r) panels. Symbols $\sigma_{y,i,(\bullet)}$ and $\phi^*_{y,i,(\bullet)}$ stand respectively for the slope and roll angle location of the logistic functions that represent the static variation of the vortex spanwise position with the roll angle.

The state variable $\bar{v}$ is defined to represent the increase in panel lift due to both the increase in vortex strength and the approximation of the vortex core to the panel upper surface, as the wing rolls. Because of that, the forcing terms of on the right-hand side of Eq. (2-15) are modeled to be

$$\bar{v}_{0,i,U}(\phi) = \frac{1}{1+\exp\left[-\xi_i \sigma_{v,i,U}\left(\phi - \phi^*_{v,i,U}\right)\right]} \tag{2-27}$$

$$\bar{v}_{0,i,D}(\phi) = \frac{1}{1+\exp\left[-\xi_i \sigma_{v,i,D}\left(\phi - \phi^*_{v,i,D}\right)\right]} \tag{2-28}$$

In these last equations, the symbols $\sigma_{v,i,(\bullet)}$ and $\phi^*_{v,i,(\bullet)}$ stand respectively for the slope and roll angle location of the logistic functions that represent the static variation of the effects of vortex vertical position and strength with the roll angle.

In Eq. (2-16), the first parcel $C_{N,i}(\bar{x}, \alpha_i)$ is taken as it was developed in [34], that is, as the following expansion in terms of the angle of attack α and its non-dimensional time-derivative $\hat{\dot{\alpha}}$, for the roll angle equal zero:

$$C_{N,i} = C_{N0} + C_{N\alpha}(\bar{x}_i)\alpha_i + C_{N\alpha^2}(\bar{x}_i)\alpha_i^2 + C_{N\hat{\dot{\alpha}}}(\bar{x}_i)\hat{\dot{\alpha}}_i + C_{N\hat{\dot{\alpha}}^2}\hat{\dot{\alpha}}_i^2 + C_{N\alpha\hat{\dot{\alpha}}}(\bar{x}_i)\alpha_i\hat{\dot{\alpha}}_i \quad \textbf{(2-29)}$$

where

$$C_{N\chi}(\bar{x}_i) = a_j + b_j\bar{x}_i + c_j\bar{x}_i^2 \quad \textbf{(2-30)}$$

with $\chi = \alpha, \alpha^2, \hat{\dot{\alpha}}, \hat{\dot{\alpha}}^2, \alpha\hat{\dot{\alpha}}$, and $j = 1,2,3,4,5$, respectively. The motion variable $\hat{\dot{\alpha}} = \hat{t}\,\dot{\alpha}$ is the non-dimensional angle of attack rate and $\hat{t}$ is the characteristic time of the flow defined as in Eq. (1-17).

In Eq. (2-16), $\Delta C_{N,i}(\phi)$ is the parcel that accounts for the effects of the roll angle at a fixed pitch angle value θ_0. It is this normal force term that accounts for the effects due to both vortex vertical position and strength. The normal lifting force on a panel gets bigger as the roll angle changes in a way that makes the panel go down. Also, it was shown in [46] that the limit-cycle oscillations are sustained by a time lag in vortex core position and strength. To make this model capable of handling these variations in a nonlinear way, the panel normal force $\Delta C_{N,i}(\phi)$ is built according to the following dependence of the roll angle ϕ and of the non-dimensional roll rate $\hat{\dot{\phi}}$:

$$\begin{aligned}\Delta C_{N,i}(\bar{v}_i, \phi) = {} & C_{N\phi}(\bar{v}_i)\phi + C_{N\phi^3}(\bar{v}_i)\phi^3 + C_{N\phi^5}(\bar{v}_i)\phi^5 + C_{N\hat{\dot{\phi}}}(\bar{v}_i)\hat{\dot{\phi}} + C_{N\hat{\dot{\phi}}^3}(\bar{v}_i)\hat{\dot{\phi}}^3 \\ & + C_{N\phi^2\hat{\dot{\phi}}}(\bar{v}_i)\phi^2\hat{\dot{\phi}} + C_{N\phi\hat{\dot{\phi}}^2}(\bar{v}_i)\phi\hat{\dot{\phi}}^2\end{aligned} \quad \textbf{(2-31)}$$

where

$$\hat{\dot{\phi}} = \dot{\phi}\frac{b}{2V} \quad \textbf{(2-32)}$$

$$C_{N\phi}(\bar{v}_i) = a_6 + b_6\bar{v}_i + c_6\bar{v}_i^2$$

$$C_{N\phi^3}(\bar{v}_i) = a_7 + b_7\bar{v}_i + c_7\bar{v}_i^2$$

$$C_{N\phi^5}(\bar{v}_i) = a_8 + b_8\bar{v}_i + c_8\bar{v}_i^2$$

$$C_{N\dot{\phi}}(\bar{v}_i) = a_9 + b_9\bar{v}_i + c_9\bar{v}_i^2 \qquad \textbf{(2-33)}$$

$$C_{N\dot{\phi}^3}(\bar{v}_i) = a_{10} + b_{10}\bar{v}_i + c_{10}\bar{v}_i^2$$

$$C_{N\phi^2\dot{\phi}}(\bar{v}_i) = a_{11} + b_{11}\bar{v}_i + c_{11}\bar{v}_i^2$$

$$C_{N\phi\dot{\phi}^2}(\bar{v}_i) = a_{12} + b_{12}\bar{v}_i + c_{12}\bar{v}_i^2$$

V = free stream airspeed.

The coefficients a_j, b_j, c_j, are functions of the angle of attack, and are determined by a least-squares fit with the experimental data. The expansion terms in Eq. (2-31) were picked in order to match the expansion developed by Konstadinopoulos, Mook, and Nayfeh for $C_l(\phi)$ in [53].

The parameters to be identified using wind tunnel data for this postulated model are dependent on the pitch angle θ_0 at which the identification is done. They are:

- the polynomial coefficients C_{N0}, a_j, b_j, c_j, $j = 1,2,3,4,5$ of Eqs. (2-29) and (2-30);
- the polynomial coefficients a_j, b_j, c_j , $j = 6,7,8,9,10,11,12$ of Eqs. (2-31) and (2-33);
- transient time-constants τ_{1x}, τ_{1y}, τ_{1v} appearing respectively in Eqs. (2-13), (2-14), and (2-15);
- time-delay constants $\tau_{2,\alpha}$, $\tau_{2,\phi}$ from Eqs. (2-21) and (2-24);

- parameters $\alpha^*_{(\bullet)}$, $\phi^*_{(\bullet)}$, and $\sigma_{(\bullet)}$ of logistic equations (2-19), (2-20), (2-25), (2-26), (2-27), and (2-28).

Later on this report, it is shown in Figures 3-10 through 3-17 that the model responses obtained for this unsteady aerodynamics model described above results in good agreement with the experimental data. Also, it is shown in Chapter 4 that this second model is able to simulate wing rock.

Next, we describe some details of the model parameters identifications.

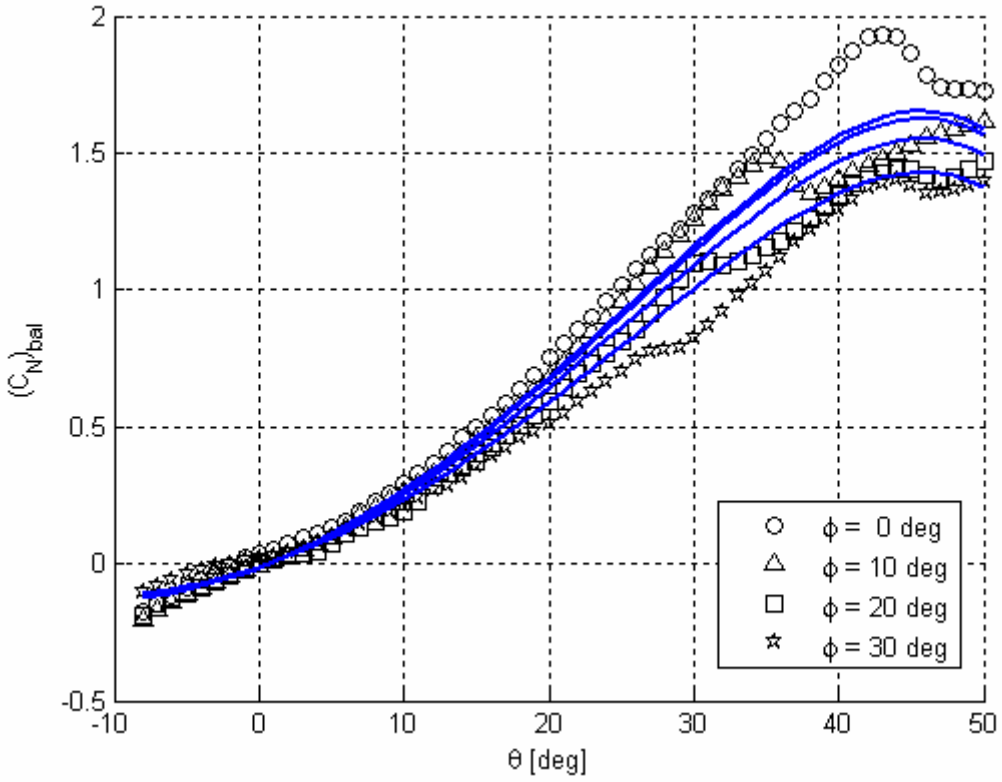

Figure 2-2 Static model responses *vs* experimental data for the normal force of the slender delta wing, static values in balance coordinates for the improved Stagg's model.

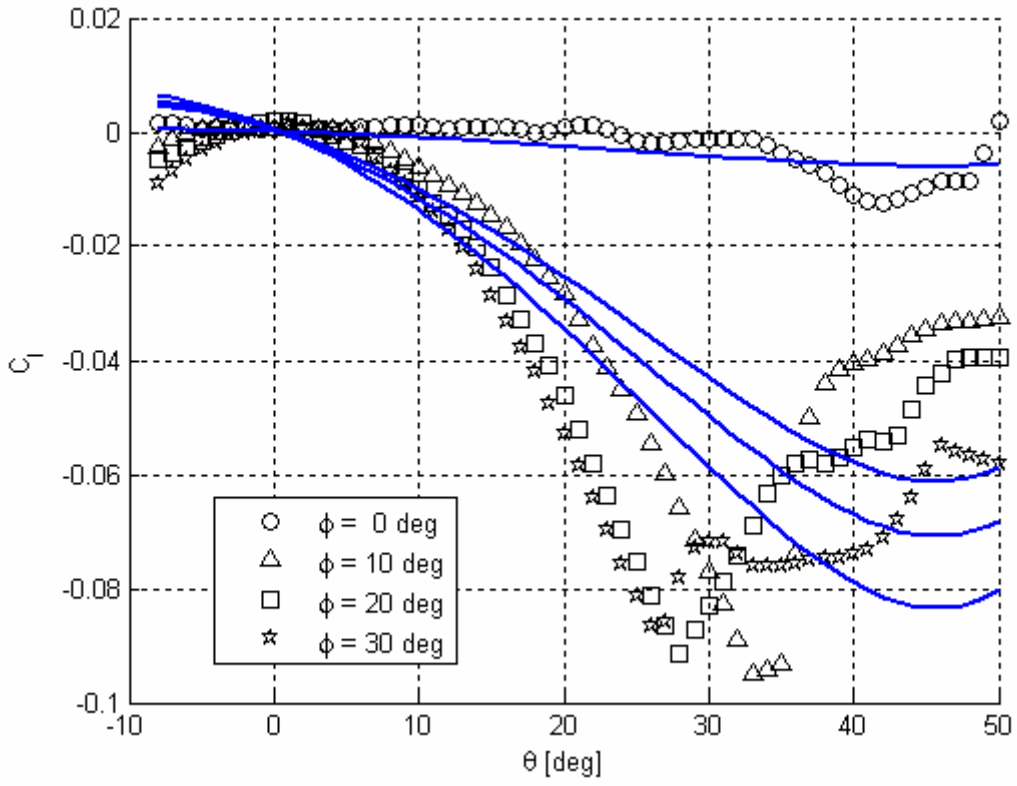

Figure 2-3 Model responses *vs* experimental data for the rolling moment coefficient of the slender delta wing, static values for the improved Stagg's model.

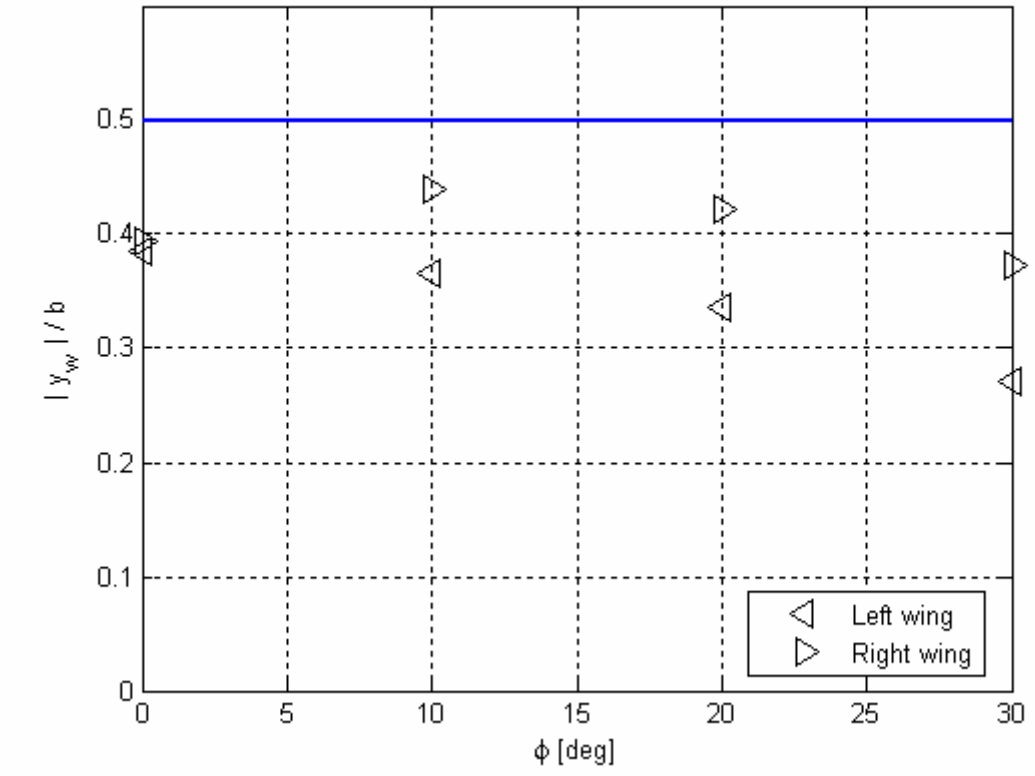

Figure 2-4 Variation of the normal force non-dimensional arms with the roll angle, static values for the improved Stagg's model.

3 Model Parameters Identifications

3.1 Parameter Identification Method

The identification method used here is the minimum mean-square error approach. The models have their parameters identified using experimental data in three phases and the squared error is minimized through an unconstrained optimization process. In the first two phases, the parameter identification is done using static experimental data. First, we identify the parameters involved with the determination of the static terms of the normal lifting forces ($\vec{x}_{CN}$). These parameters are those related to the quadratic polynomials that determine the stability derivatives with respect to the motion variables (a_j, b_j, c_j), and those that are used to determine the static values of the internal state variables $\bar{x}_i$ for each panel *i*, namely $\alpha^*_{(\bullet)}, \sigma_{(\bullet)}$. Next, we identify only the parameters associated with the arms of the rolling moment coefficients ($\vec{x}_{Cl}$) using the experimental static values of the rolling moment coefficient. In those first two phases of the parameter identification, the parameters related to the dynamic behavior of the model are kept out of the optimization process. These dynamic parameters are the coefficients (a_j, b_j, c_j) of the quadratic polynomials that represent the stability derivatives with respect to the time-rate of the motion variables, and the time-constant and time-delay parameters, stored in vector $\vec{x}_{dyn}$. We then take the parameter values previously determined in the two identification phases described above and use them as initial guess for the third identification phase. In this third phase, the model parameters are determined when the mean squared error with respect to dynamic experimental data is minimized for each value of the sting pitch angle. The dynamic phase of the identification is done using the experimental values of the rolling moment time histories obtained as described in Section 3.2. Table 3-1 and Table 3-2 show the elements of vectors $\vec{x}_{CN}$, $\vec{x}_{Cl}$, and $\vec{x}_{dyn}$ for the first and the second investigated models, respectively.

When the quasi-static sequences of experimental data are considered, the error cost-functions to be minimized are as follows,

$$\varepsilon_{CN}(\vec{x}_{CN}) = \frac{1}{M * N}\sum_{j=1}^{N}\sum_{i=1}^{M}\left[\hat{C}_N(\theta_{0i},\phi_j) - C_N(\theta_{0i},\phi_j,\vec{x}_{CN})\right]^2 \quad \textbf{(3-1)}$$

$$\varepsilon_{Cl}(\vec{x}_{Cl}) = \frac{1}{M * N}\sum_{j=1}^{N}\sum_{i=1}^{M}\left[\hat{C}_l(\theta_{0i},\phi_j) - C_l(\theta_{0i},\phi_j,\vec{x}_{Cl})\right]^2 \quad \textbf{(3-2)}$$

where each value of the roll angle in the sequence ϕ_j, *j = 1,2, ... , N* has a corresponding sequence of values for the wind tunnel sting pitch angle θ_{0i}, *i = 1,2, ... , M*, as shown in Figures 1-17 and 1-18. At these points, the wind tunnel measurements are $\left\{\hat{C}_N(\theta_{0i},\phi_j), \hat{C}_l(\theta_{0i},\phi_j); i = 1,2,...,M; j = 1,2,...,N\right\}$, while the model responses determined at the same points for a given sets $\vec{x}_{CN}, \vec{x}_{Cl}$ of model parameters are $\left\{C_N(\theta_{0i},\phi_j,\vec{x}_{CN}), C_l(\theta_{0i},\phi_j,\vec{x}_{Cl}); i = 1,2,...,M; j = 1,2,...,N\right\}$.

When the published values of wind tunnel dynamic measurements at unsteady flow conditions are used to identify parameters, one roll angle time history $\{\phi(t_i), 0 \le t_i \le T_F\}$, such that $0 = t_1 < t_2 < ... < t_i < t_{i+1} < ... < t_L = T_F$, is taken for each fixed value of the sting pitch angle θ_0 in the sequence θ_{0k}, *k = 1, 2, ... , K* . If the corresponding dynamic wind tunnel measurements of the rolling moment coefficient can be represented by $\left\{\hat{C}_l(\phi(t_i,\theta_0)); i = 1,2,...,L; k = 1,2,...,K\right\}$ and the values of the model responses calculated at the same points for given set $\vec{x}_{dyn}$ of model parameters are $\left\{C_l(\phi(t_i,\theta_0),\vec{x}); i = 1,2,...,L; k = 1,2,...,K\right\}$, the error cost-function for the dynamic phase of the identification is

$$\varepsilon_{dyn}\left(\vec{x}_{dyn}\right)=\frac{1}{L}\sum_{i=1}^{L}\left[\hat{C}_l\left(\phi(t_i,\theta_0)\right)-C_l\left(\phi(t_i,\theta_0),\vec{x}_{dyn}\right)\right]^2 \quad \textbf{(3-3)}$$

For known sequences of experimental data at each fixed pitch angle θ_0, the design variables in the cost-functions (3-1) to (3-3) are the model parameters stored in $\vec{x}_{CN}$, $\vec{x}_{Cl}$, and $\vec{x}_{dyn}$. Representing the cost-functions in terms of these model parameters, we have $\varepsilon_{CN}\left(\vec{x}_{CN}\right)$, $\varepsilon_{Cl}\left(\vec{x}_{Cl}\right)$, and $\varepsilon_{dyn}\left(\vec{x}_{dyn}\right)$. In this particular case, these individual cost-functions are controlled by different sets of variables, that is, $\vec{x}^*_{CN}$, $\vec{x}^*_{Cl}$, $\vec{x}^*_{dyn}$ are the solutions to individual objectives, shown as follows

$$\left(\vec{x}^*_{CN},f^*_{CN}\right)=\min\varepsilon_{CN}\left(\vec{x}_{CN}\right)$$

$$\left(\vec{x}^*_{Cl},f^*_{Cl}\right)=\min\varepsilon_{Cl}\left(\vec{x}_{Cl}\right) \quad \textbf{(3-4)}$$

$$\left(\vec{x}^*_{dyn},f^*_{dyn}\right)=\min\varepsilon_{dyn}\left(\vec{x}_{dyn}\right)$$

In this research, MATLAB™ scripts have been used to find the values of $\left(\vec{x}^*_{CN},\varepsilon^*_{CN}\right)$, $\left(\vec{x}^*_{Cl},\varepsilon^*_{Cl}\right)$, and $\left(\vec{x}^*_{dyn},\varepsilon^*_{dyn}\right)$. These scripts call the built-in function *fminsearch*, a multidimensional unconstrained nonlinear minimization based on the Nelder-Mead algorithm [56].

Next, we show the experimental data used to identify the model parameters and present some of the results of the identification.

3.2 Simulated Experimental Data Used in Parameter Identification

Since wind tunnel tests are not part of this research, previously published experimental data are used to identify the parameters of the investigated models. Because not all the needed data could be found in just one reference, data from several references are combined to form the set of simulated experimental data used in the parameter

identification. The static data used for the parameter identification are those obtained by Levin and Katz [47] for the slender delta wing whose geometry is shown in Figure 1-22. These static experimental data are reproduced in Figure 1-17 and Figure 1-18. Here, it is assumed that this wing undergoes wing rock for pitch angles between 22 and 45 degrees of angle of attack. It is also assumed that this wing has a dynamic behavior during steady state limit cycles similar to the experimental data obtained by Nguyen, Yip, and Chambers [45] for θ_0 = 27 (Figure 1-15) and 32 deg (Figure 1-16). The rolling moment coefficient experimental histogram for θ_0 = 27 deg is also used to identify the model parameters for θ_0 = 38 deg. The rolling moment coefficient experimental histogram for θ_0 = 20 deg is also used to identify model parameters for θ_0 = 45 deg. All these data are multiplied by correction factors, to make the maximum absolute values of the rolling moment coefficient in the cycle consistent with the static value at the same pitch and roll angles shown in Figure 1-18. For the wing pitch angles at which the oscillations in roll damp out, the experimental data used to identify the parameters are assumed to have the same qualitative behavior exhibited in Figure 1-11. At these values of the pitch angle, the model parameters are identified on the first cycle in roll.

The simulated dynamic experimental data set was extracted from [45] as described next. The roll angle time history used at angles of attack equal to 27 deg and 38 deg is obtained from reference [45], and shown in figures 3-13 and 3-16. This roll angle time history was originally obtained in [45] for the angle of attack equal to 27 deg, where the wing undergoes wing rock, but it is assumed here to be valid also for an angle of attack of 38 deg. The roll angle time history used for the angles of attack equal to 20 and 45 deg is shown in figures 3-10 and 3-13. The values of the roll angle ϕ corresponding to chosen discrete values of time were taken from these time histories. The corresponding values of the rolling moment coefficients were taken from the $C_l \times \phi$ plots for each discrete value of ϕ. The resulting simulated experimental C_l time histories are shown in figures 3-4, 3-6, 3-8, 3-11, 3-14, 3-17, and 3-20.

3.3 Identification Results

The whole set of model parameters involved in the previously discussed aerodynamic formulations is stored as vector $\vec{x}$. In order to merge the slender delta wing unsteady aerodynamic model with the equations of motion and proceed with further analyses, the models corresponding to the formulations described in Chapter 2 are identified using the slender delta wing experimental data described in Section 3.2, and the results are presented in the next Section.

3.3.1 Parameter Identification for the First Investigated Model

The results of the parameter identification of the first investigated model using the static experimental data are shown from Figure 3-1 to Figure 3-3. Comparing Figure 1-19 and Figure 3-3, we see that the values of the rolling moment arms vary with the roll angle in the opposite direction from expectations. The reason for that is that this formulation does not include the representation of vortex strength and vertical position, which would be responsible for the pressure distribution surfaces over the wing panels. Therefore, the restoring rolling moment increases for larger roll angle values is simulated in this formulation by a bigger moment arm. The remaining parameters identified using static experimental data are shown on Eqs. (3-5) to (3-7), and in Table 3-4.

Next, the model parameters found for the first investigated model are shown in Equations (3-5) to (3-22).

$$\begin{aligned} C_{Ni} = & \text{-0.005288} + C_{N\alpha}(\bar{x}_i)\alpha_i + C_{N\alpha^2}(\bar{x}_i)\alpha_i^2 \\ & + C_{N\hat{\alpha}}(\bar{x}_i)\hat{\dot{\alpha}}_i + C_{N\hat{\alpha}^2}(\bar{x}_i)\hat{\dot{\alpha}}_i^2 + C_{N\alpha\hat{\alpha}}(\bar{x}_i)\alpha_i\hat{\dot{\alpha}}_i \end{aligned} \quad \textbf{(3-5)}$$

where:

$$C_{N\alpha}(\bar{x}_i) = 0.6703 - 7.293\,\bar{x}_i - 5.427\,\bar{x}_i^2 \quad \textbf{(3-6)}$$

$$C_{N\alpha^2}(\bar{x}_i) = 1.453 - 3.261\,\bar{x}_i + 1.838\,\bar{x}_i^2 \quad \textbf{(3-7)}$$

i = left, right panel.

The terms of Eq. (3-5) which are dependent on unsteady aerodynamics have parameters identified using the rolling moment coefficient experimental time-histories, for one value of the wing pitch angle at a time. The results of this phase of the identification for the first investigated model are presented in Figures 3-4 to 3-9. The identified parameters of the first investigated model at some selected values of the pitch angle θ_0 are shown as follows on Eqs. (3-8) to (3-22):

► $\theta_0 = 20\,\text{deg}$:

$$C_{N\dot{\alpha}}(\bar{x}_i) = -9.656 + 761.9\,\bar{x}_i + 0.005699\,\bar{x}_i^2 \quad \textbf{(3-8)}$$

$$C_{N\dot{\alpha}^2}(\bar{x}_i) = 0.5342\,\bar{x}_i^2 \quad \textbf{(3-9)}$$

$$C_{N\alpha\dot{\alpha}}(\bar{x}_i) = 0 \quad \textbf{(3-10)}$$

$$\tau_{1,x} = 0.1995\,\hat{t} \quad \textbf{(3-11)}$$

$$\tau_{2,\alpha} = 0.7952\,\hat{t} \quad \textbf{(3-12)}$$

► $\theta_0 = 27\,\text{deg}$:

$$C_{N\dot{\alpha}}(\bar{x}_i) = -10.94 + 785.8\,\bar{x}_i + 0.005660\,\bar{x}_i^2 \quad \textbf{(3-13)}$$

$$C_{N\dot{\alpha}^2}(\bar{x}_i) = 0.3757\,\bar{x}_i^2 \quad \textbf{(3-14)}$$

$$C_{N\alpha\dot{\alpha}}(\bar{x}_i) = 0 \quad \textbf{(3-15)}$$

$$\tau_{1,x} = 0.1932\,\hat{t} \quad \textbf{(3-16)}$$

$$\tau_{2,\alpha} = 0.7924\,\hat{t} \quad \textbf{(3-17)}$$

► $\theta_0 = 45$ deg:

$$C_{N\dot{\alpha}}(\bar{x}_i) = \text{-}57.74 - 0.002444\,\bar{x}_i \quad \textbf{(3-18)}$$

$$C_{N\dot{\alpha}^2}(\bar{x}_i) = -1861 \quad \textbf{(3-19)}$$

$$C_{N\alpha\dot{\alpha}}(\bar{x}_i) = 77.41 \quad \textbf{(3-20)}$$

$$\tau_{1,x} = \text{-}4.829\,\hat{t} \quad \textbf{(3-21)}$$

$$\tau_{2,\alpha} = 0 \quad \textbf{(3-22)}$$

where $\hat{t} = 0.01428$ s

When we compare the model and the experimental data time-history responses in Figure 3-4 to Figure 3-9, it can be observed that they are not in good agreement. At the pitch angles of 20 and 27 degree, they are only similar qualitatively. At 45 degree, they are not similar even qualitatively. Trying to improve the agreement between model responses and experimental data, the formulation described in Section 2.2 is proposed. The corresponding identification results are presented in the following Section.

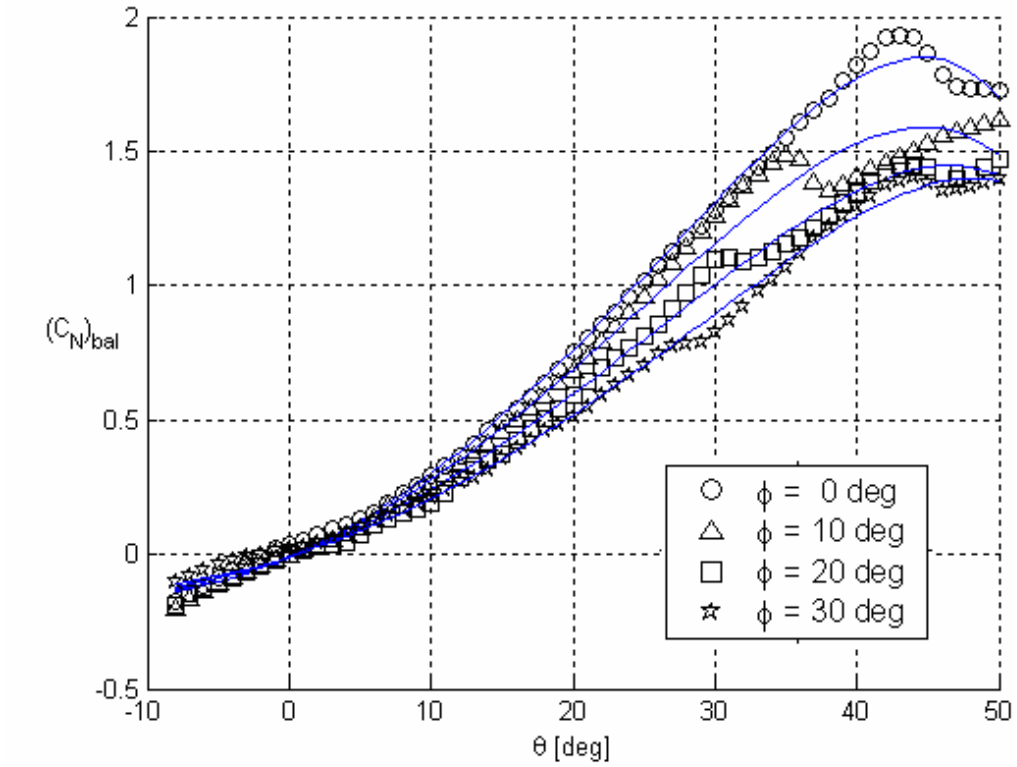

Figure 3-1 Static normal force coefficient in balance coordinates *vs* sting pitch angle. Model responses (lines) and experimental data (geometric figures) for the improved Stagg's model – the first investigated model.

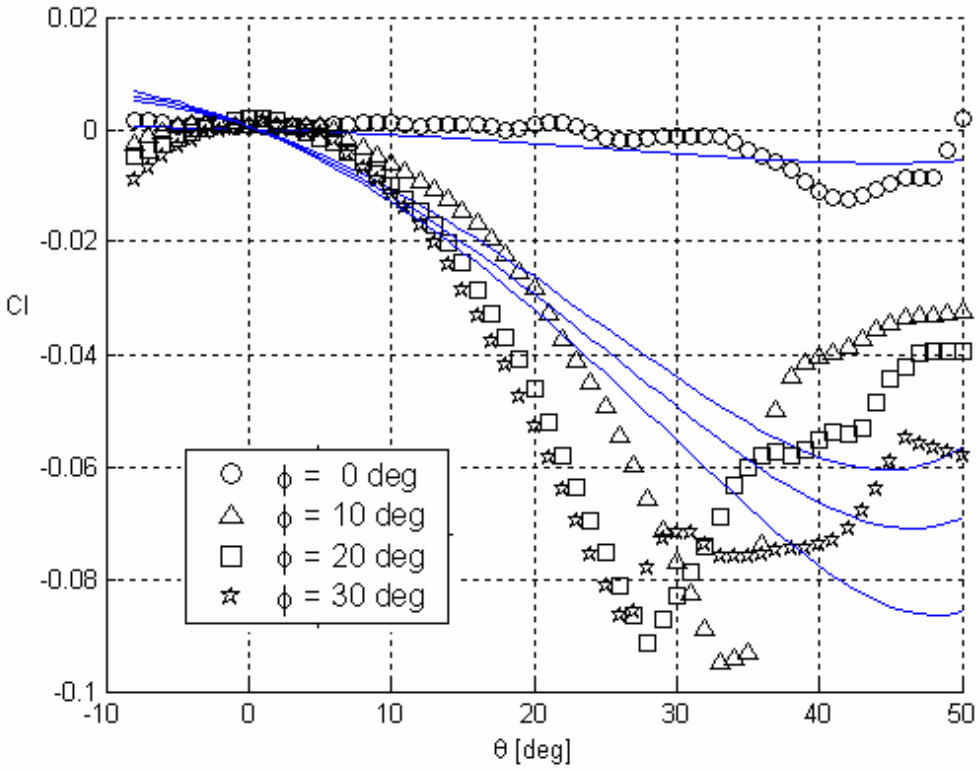

Figure 3-2 Static experimental values of the rolling moment coefficients (geometric figures) and model responses (lines) *vs*. wing pitch angle for the first investigated model.

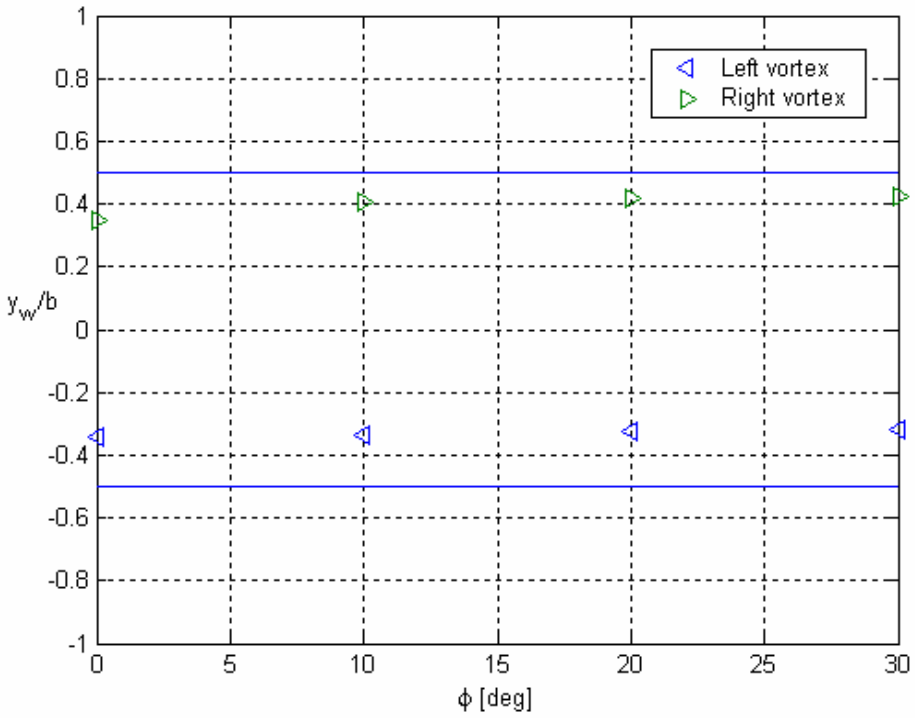

Figure 3-3 Identified static values of the normal forces non-dimensional arms *vs*. the roll angles for the first investigated model

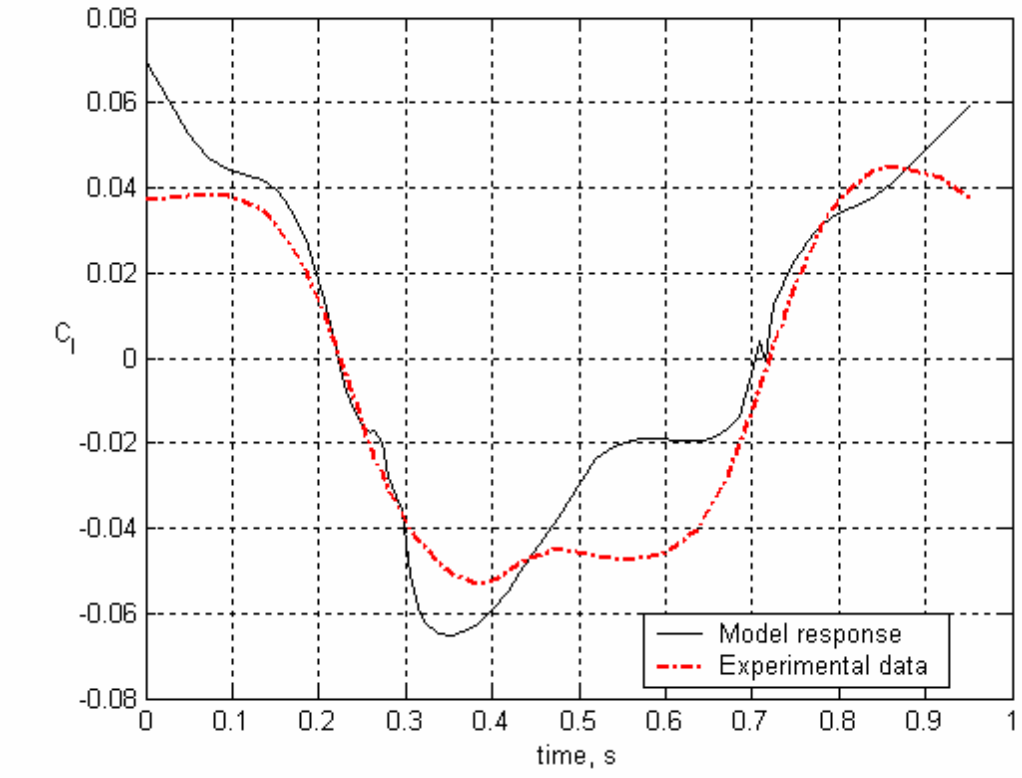

Figure 3-4 Rolling moment coefficient time histories for the first investigated model at θ_0 = 20 deg.

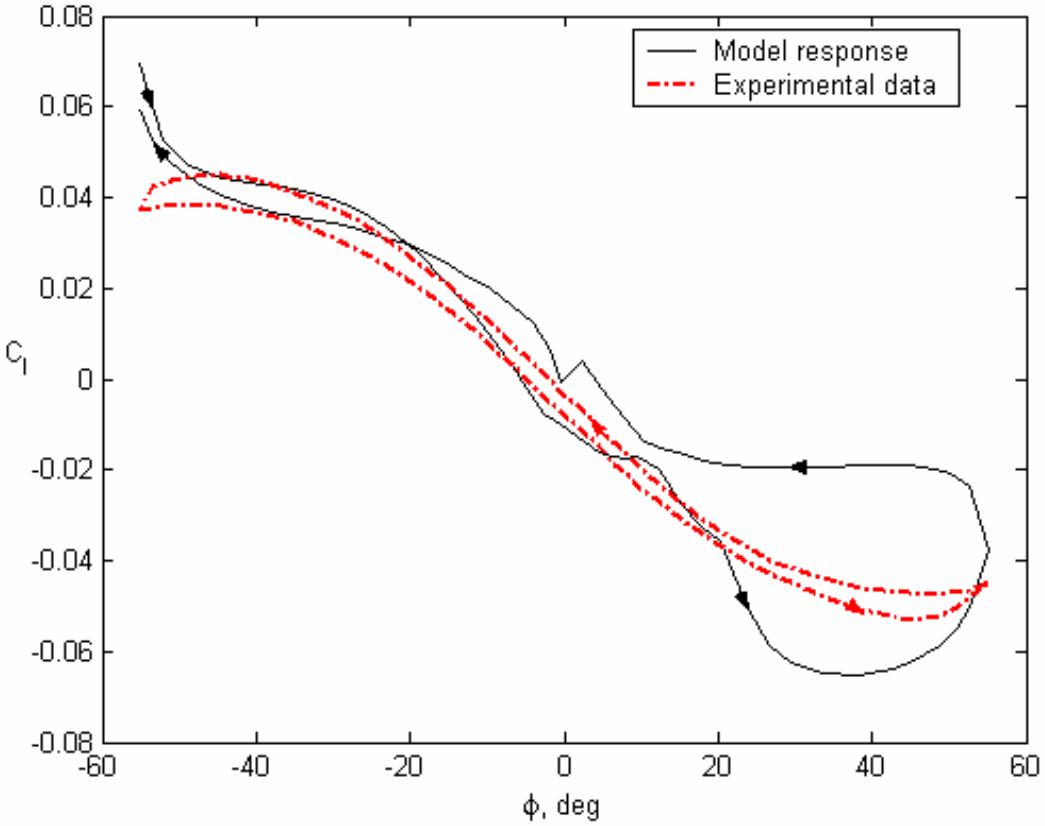

Figure 3-5 Rolling moment coefficient *vs.* roll angle for the first investigated model at θ_0 = 20 deg.

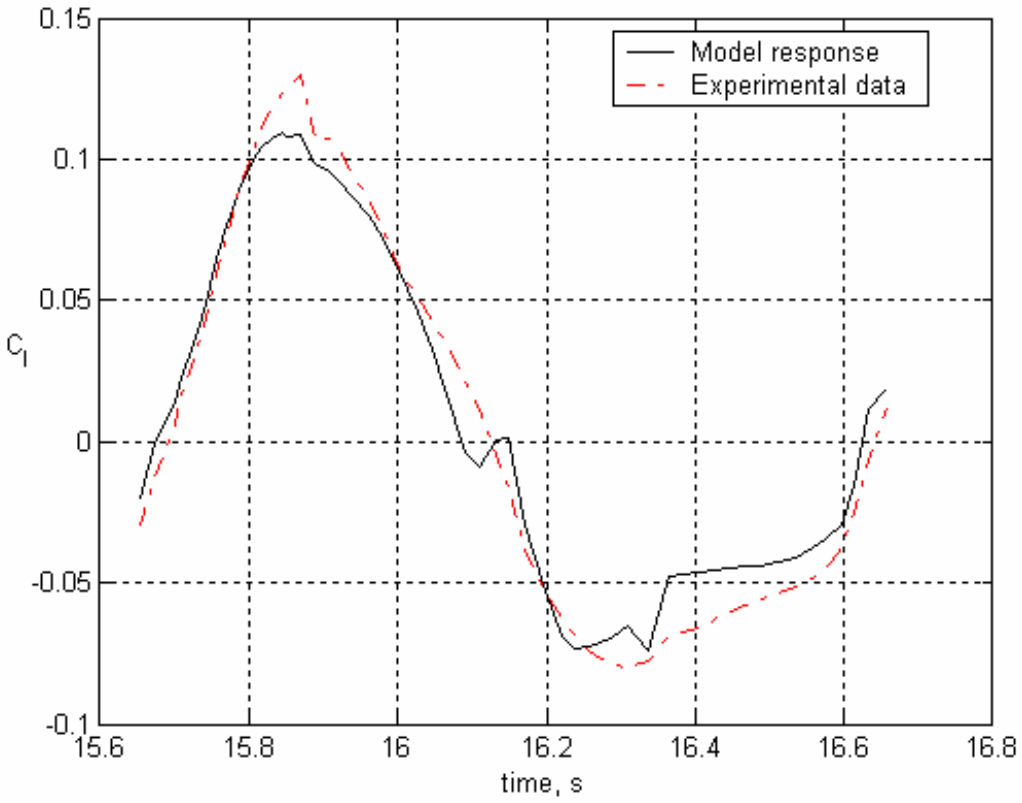

Figure 3-6 Rolling moment coefficient time histories for the first investigated model at θ_0 = 27 deg.

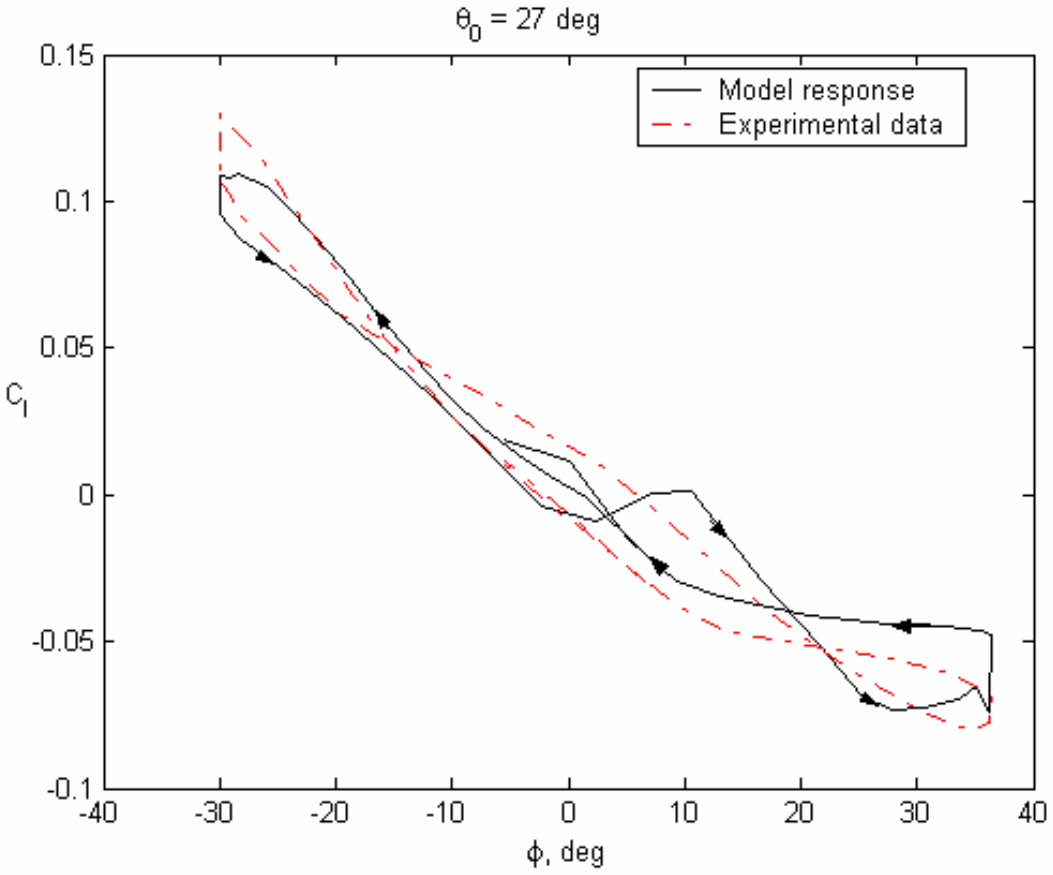

Figure 3-7 Rolling moment coefficient *vs.* roll angle for the first investigated model at θ_0 = 27 deg.

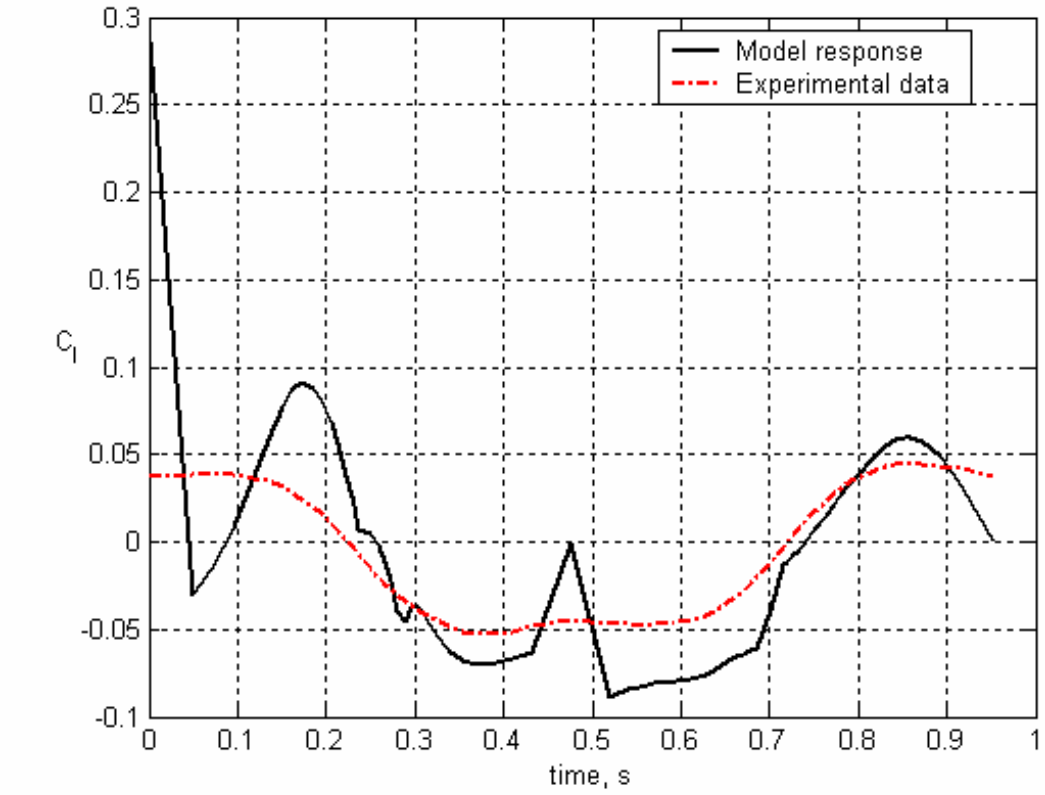

Figure 3-8 Rolling moment coefficient time histories for the first investigated model at θ_0 = 45 deg.

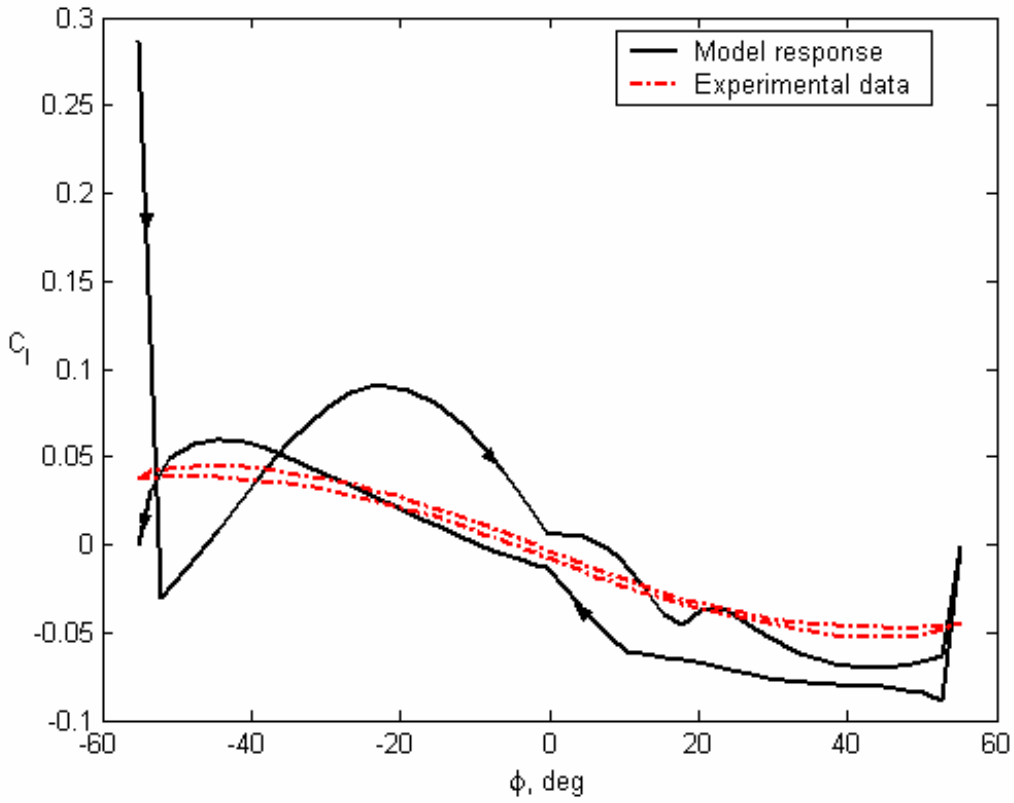

Figure 3-9 Rolling moment coefficient *vs.* roll angle for the first investigated model at θ_0 = 45 deg.

3.3.2 Parameter Identification for the Second Investigated Model

In this Section, we present the identification results for the unsteady aerodynamic formulation described in Section 2.2, when applied to a slender delta wing at angle of attack and with a degree of freedom only in roll. The identification is done with the help of the same experimental data set already described on Section 3.2. The sub-sets of design variables considered in the identification are shown on Table 3-2.

The first try to identify the parameters of the second proposed and investigated formulation is done by using the procedure exactly as described in Section 3.1 for the wing at θ_0 = 27 degrees, that means that the parameters related to the rolling moment arms identified using the static experimental data were kept fixed when the dynamic phase of the identification was made. The results of this first try were not good enough, probably because the static and dynamic experimental data used in the identifications come from different sources. In a second try, we left the parameters of the model parameters vector $\vec{x}^*_{Cl}$ free to vary in the dynamic phase of the identification. The results thus obtained match the experimental data quite well, as can be seen in figures 3-10 to 3-17. The fact that in this second proposed and investigated unsteady aerodynamic model we choose internal state variables that are related to physical characteristics of the flow allows for better insight. Some of the plots of the internal state variables for the wing pitch angle θ_0 = 27 deg are shown in Figure 3-22. According to the identification results shown in this figure, the vortex breakdown barely goes ahead of the trailing edge. This is consistent with the experimental observations [46] that show that slender wing rock happens even when vortex breakdown is not seen over the wing. Figure 3-22 is also consistent with what is expected for both the $\bar{y}$ and $\bar{v}$ internal state variables. We can see on that figure that the internal state variable $\bar{y}$, related to the spanwise positions of the vortex core, oscillates between the centerline and the half-span. Also on that figure, the internal state variable related to the vortex strength and vertical position is in phase

with the roll angle, and attains its maximum and minimum values at the extreme values of the roll angle in such a way that the restoring moments keep the oscillations going.

The second model has 62 parameters to be identified, that makes it more capable of fitting the data. Nevertheless, to find the right set of model parameters is far from straightforward. If the unconstrained optimization process is carried out for the complete roll angle time history since the beginning, a good match is hard to achieve. The best approach is to proceed with the identification starting with a part of the time history, say one fifth of the whole time history. After good agreement between model response and simulated experimental data was obtained for that part of the time history, another fraction was added, and so on. That procedure was used to get the results shown in figures 3-11 to 3-21. The identified values of the second investigated model parameters are shown in tables 3-5 to 3-9.

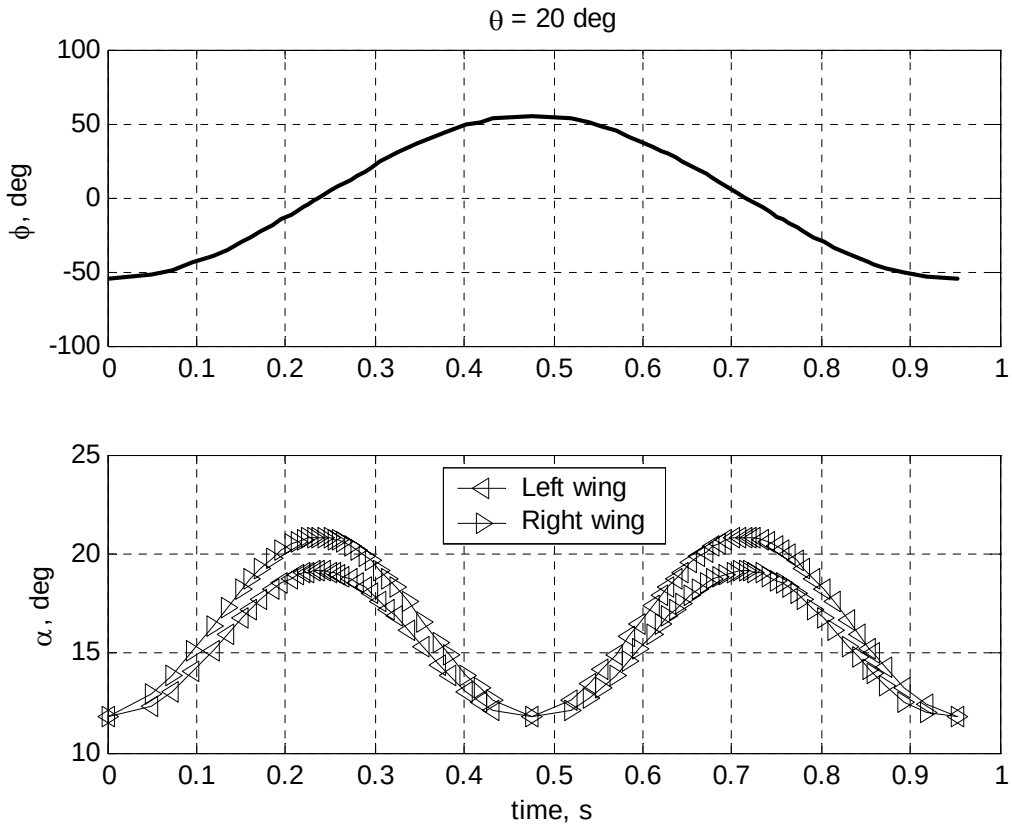

Figure 3-10 Roll angle time history for θ_0 = 20 deg (above), and corresponding angle of attack time history for each half-wing (below).

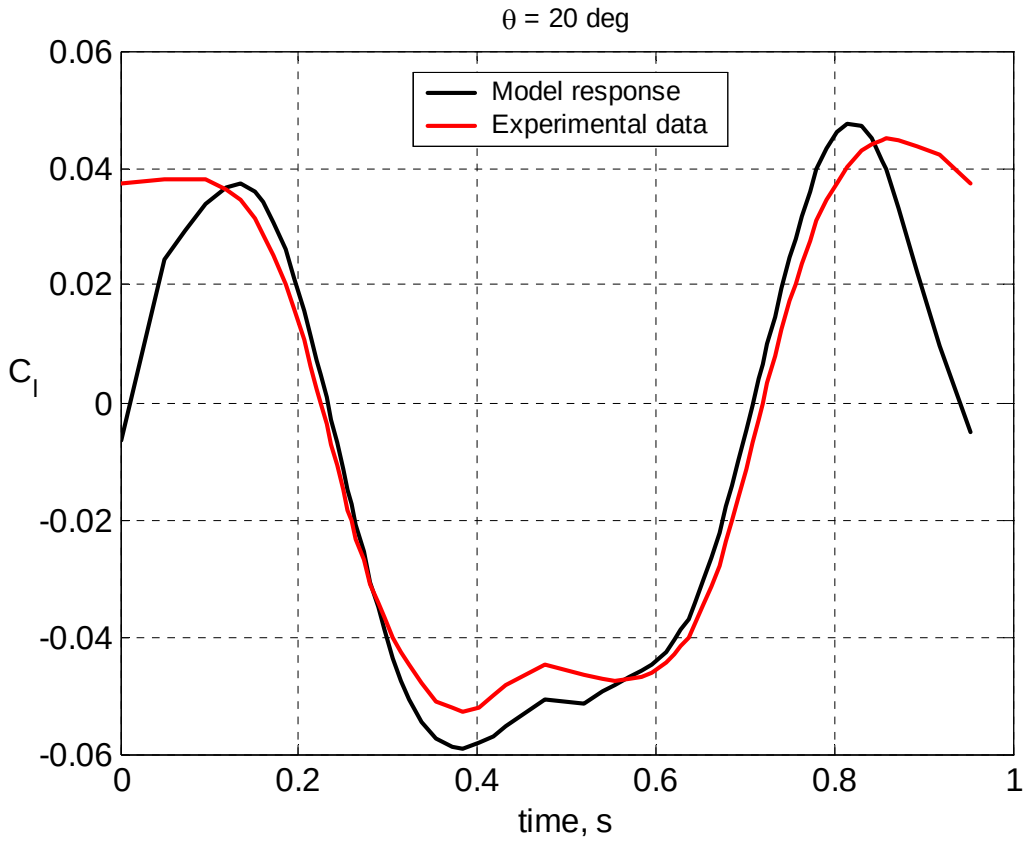

Figure 3-11 Rolling moment coefficient time-history at θ_0 = 20 deg, second investigated model.

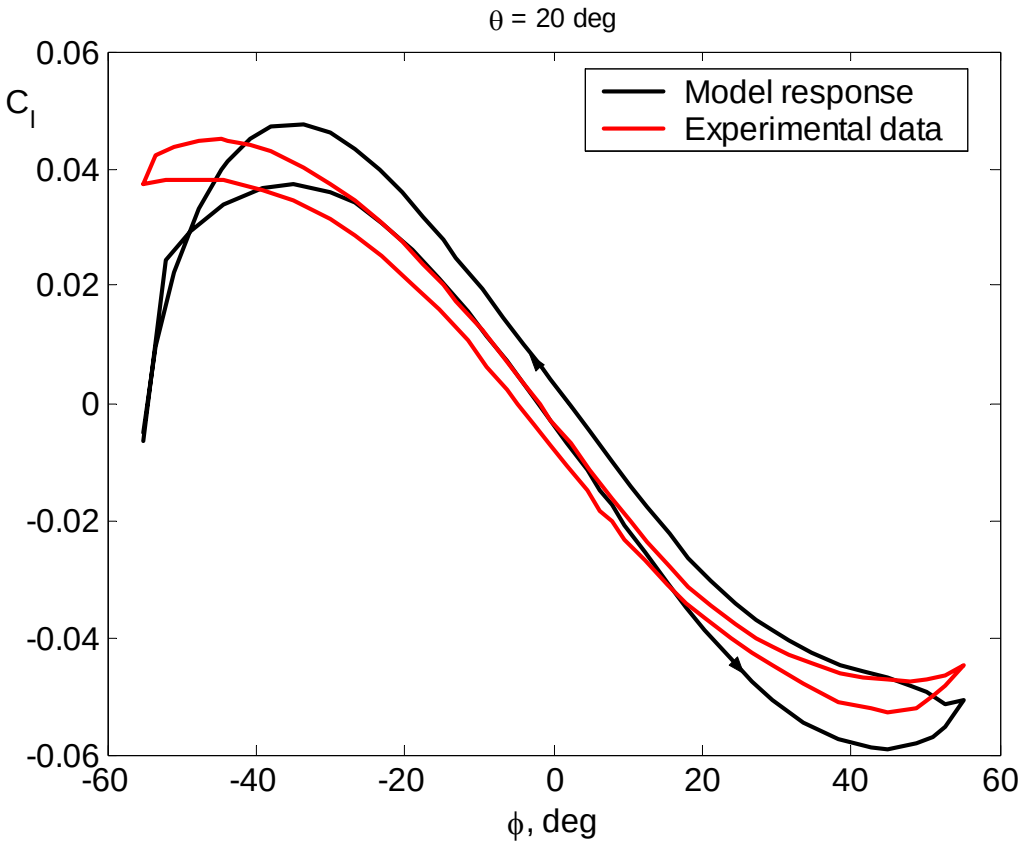

Figure 3-12 Rolling moment coefficient vs. roll angle loops at θ_0 = 20 deg, second investigated model.

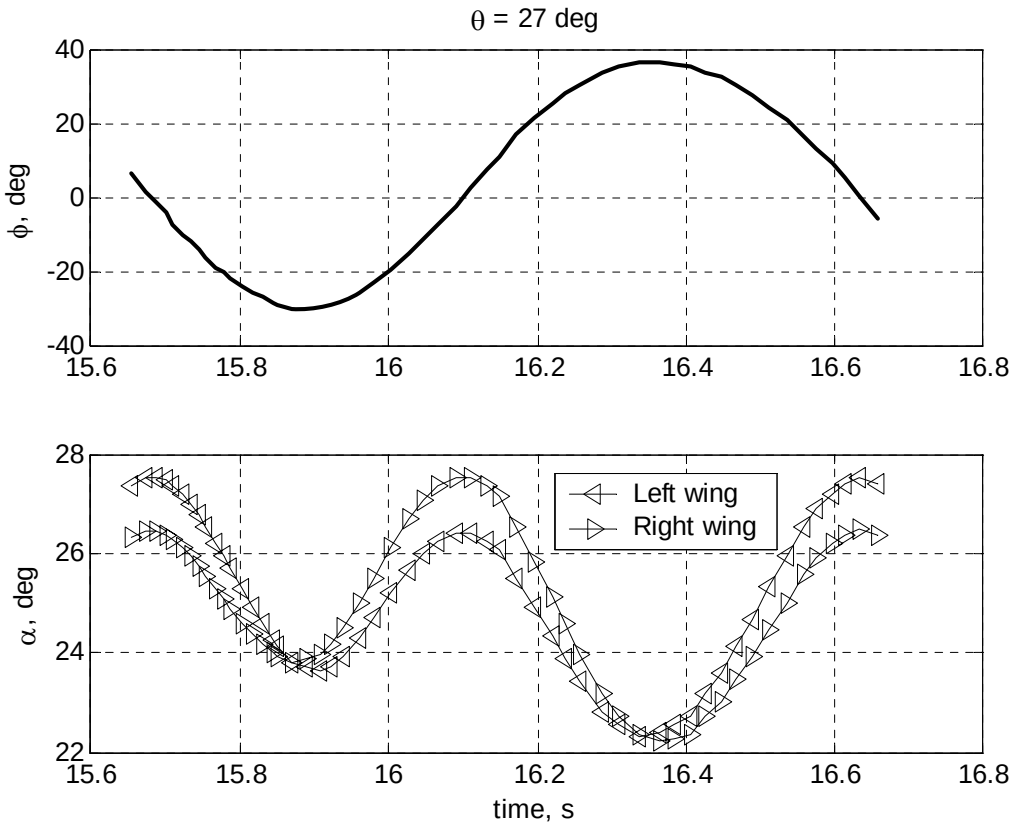

Figure 3-13 Roll angle time history for θ_0 = 27 deg (above), and corresponding angle of attack time history for each half-wing (below).

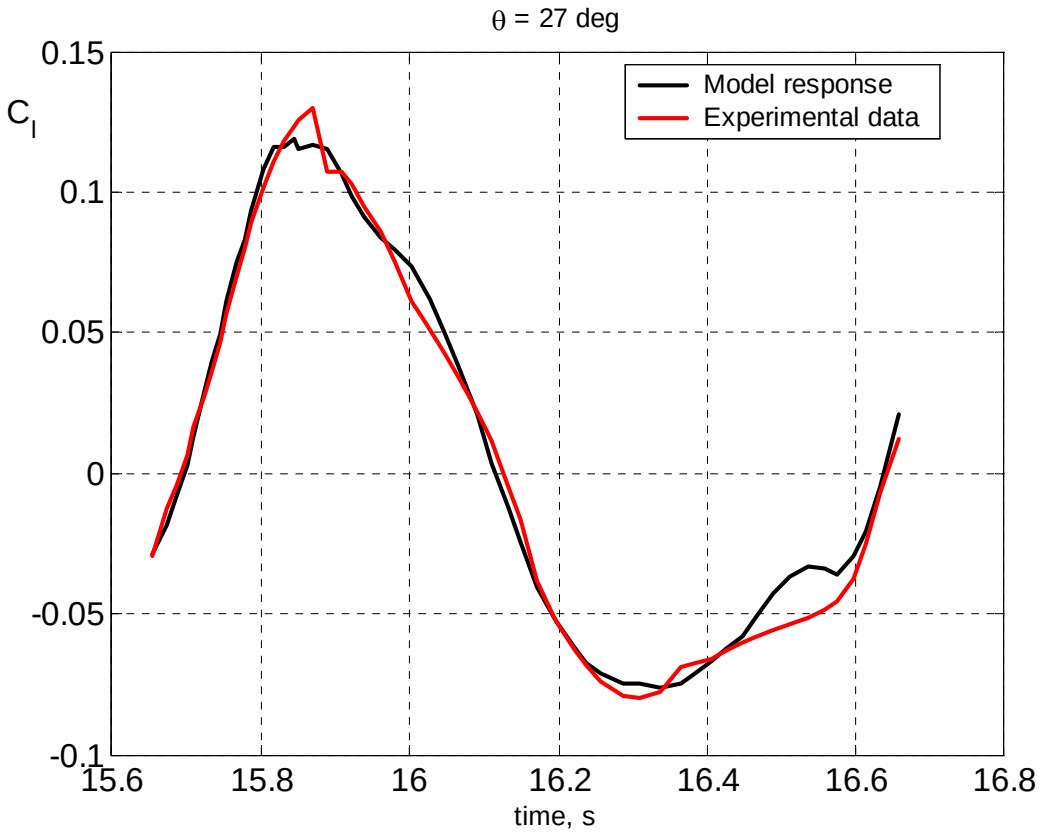

Figure 3-14 Rolling moment coefficient time-history at θ_0 = 27 deg, second investigated model.

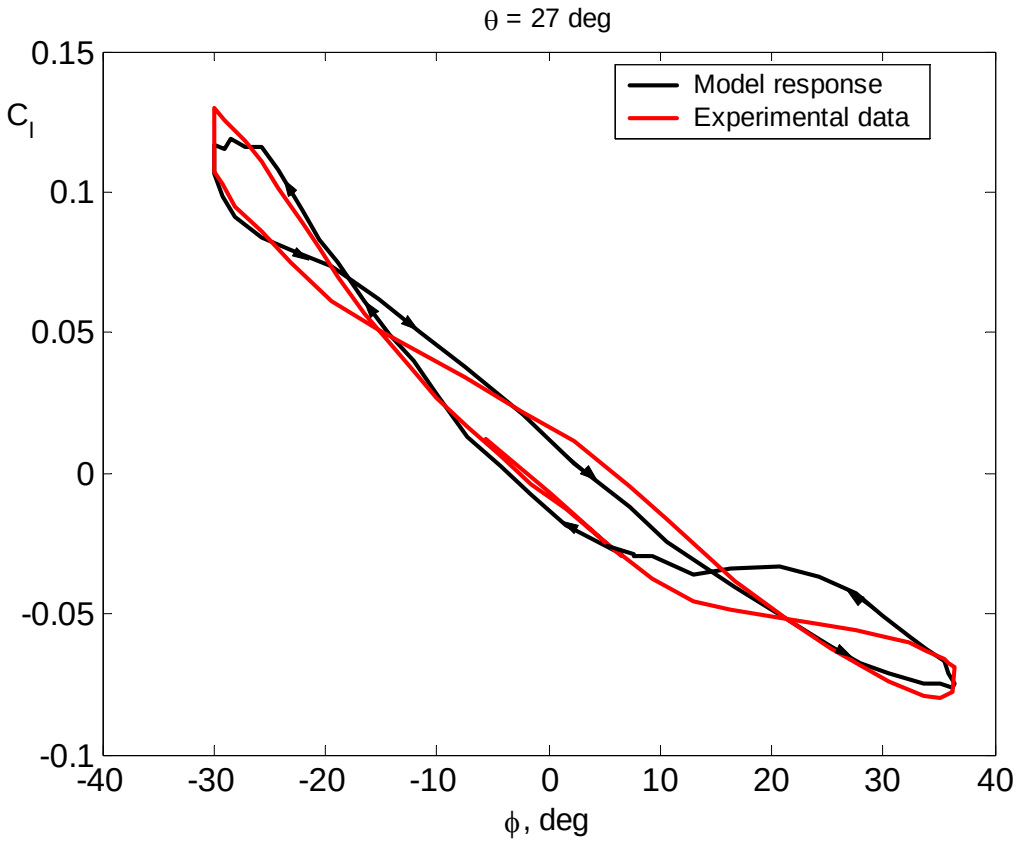

Figure 3-15 Rolling moment coefficient vs. roll angle loops at θ_0 = 27 deg.

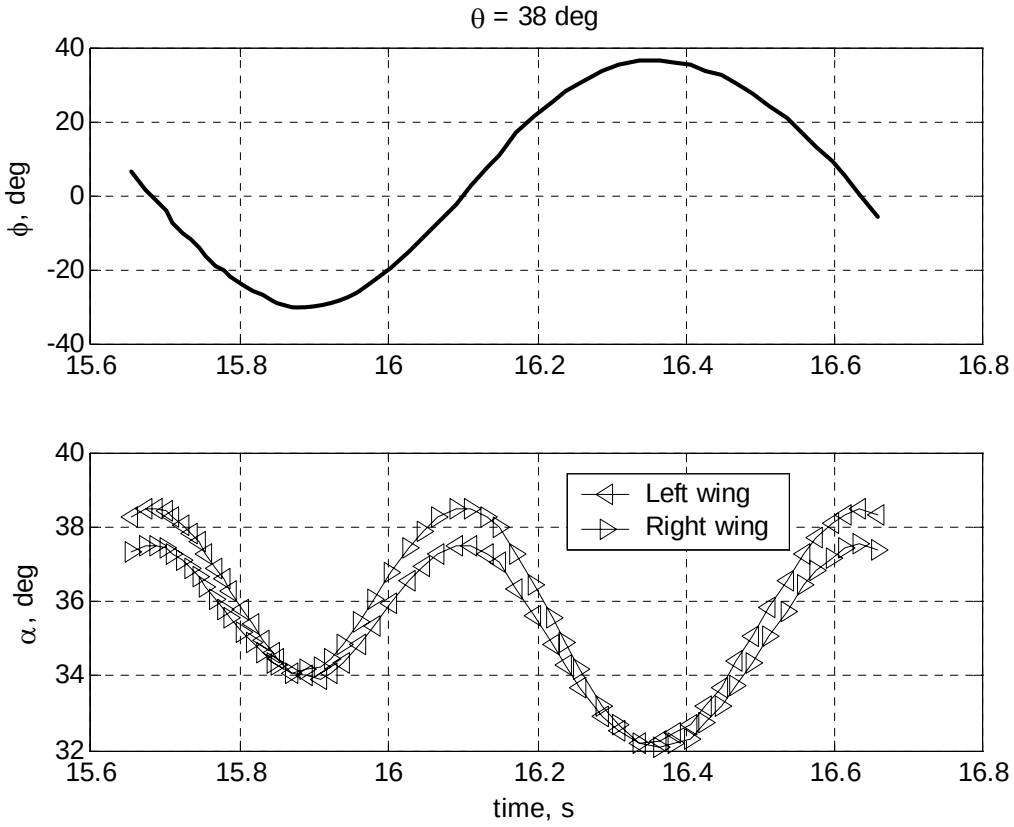

Figure 3-16 Roll angle time history for θ_0 = 38 deg (above), and corresponding angle of attack time history for each half-wing (below).

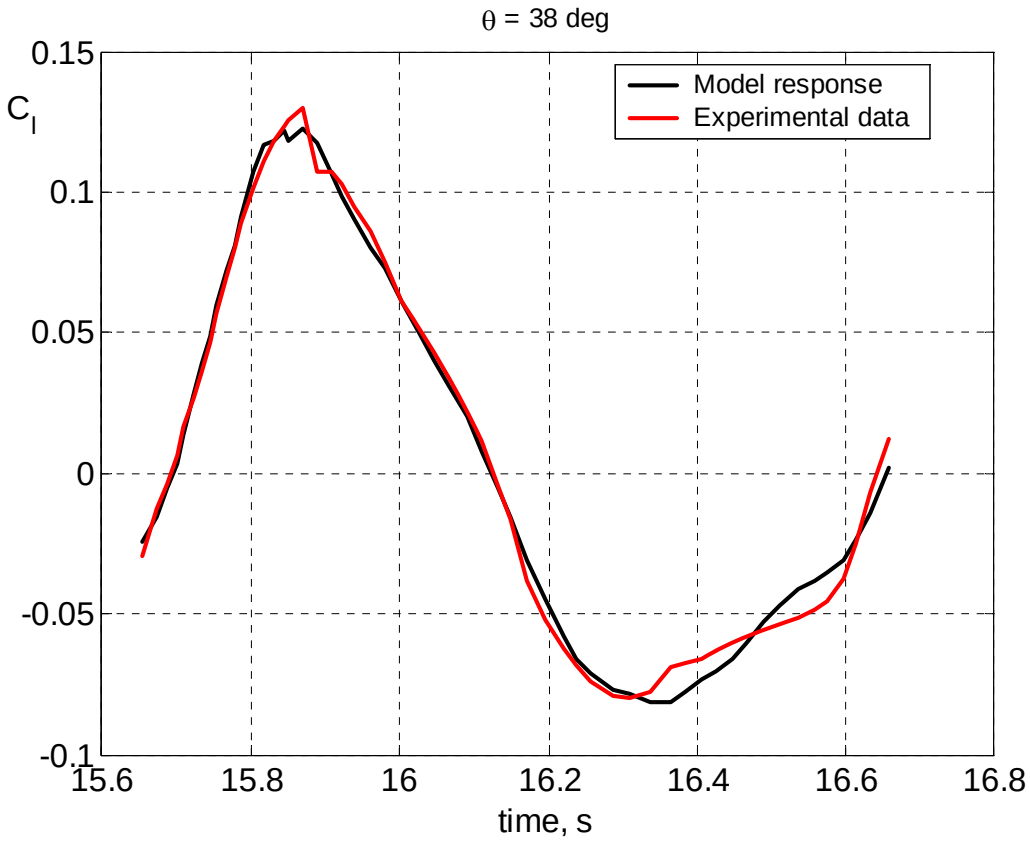

Figure 3-17 Rolling moment coefficient time-history at θ_0 = 38 deg.

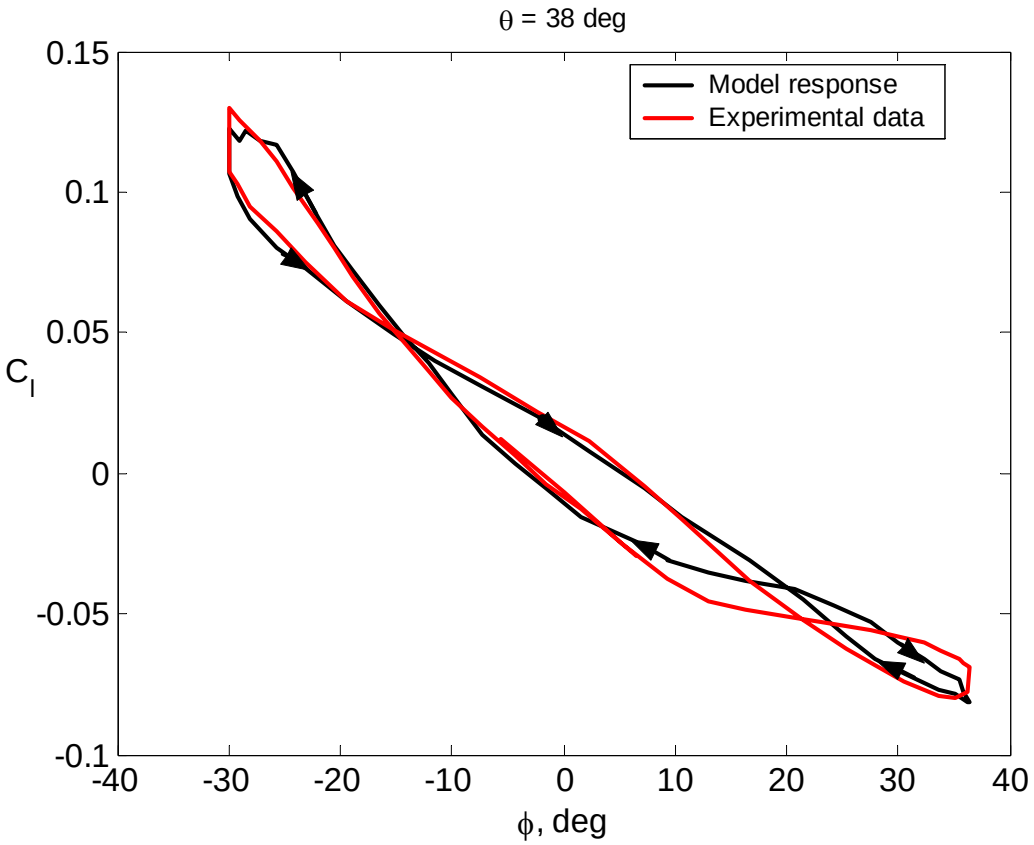

Figure 3-18 Rolling moment coefficient vs. roll angle loops at θ_0 = 38 deg.

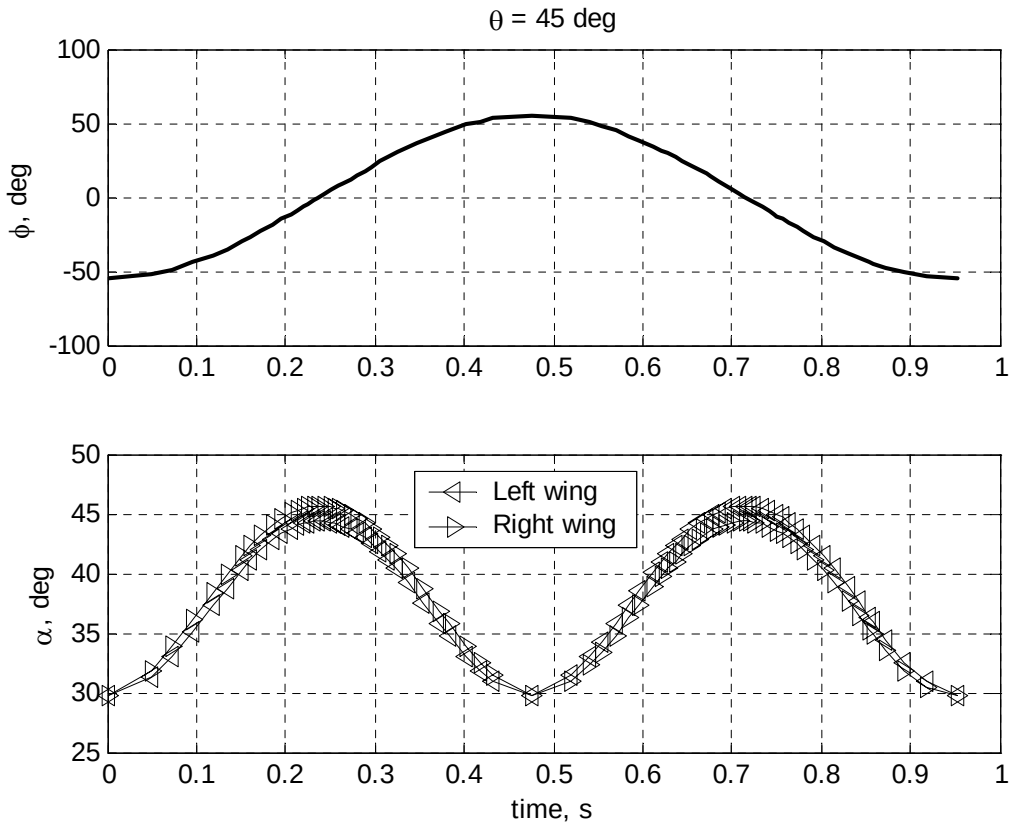

Figure 3-19 Roll angle time history for θ_0 = 45 deg (above), and corresponding angle of attack time history for each half-wing (below).

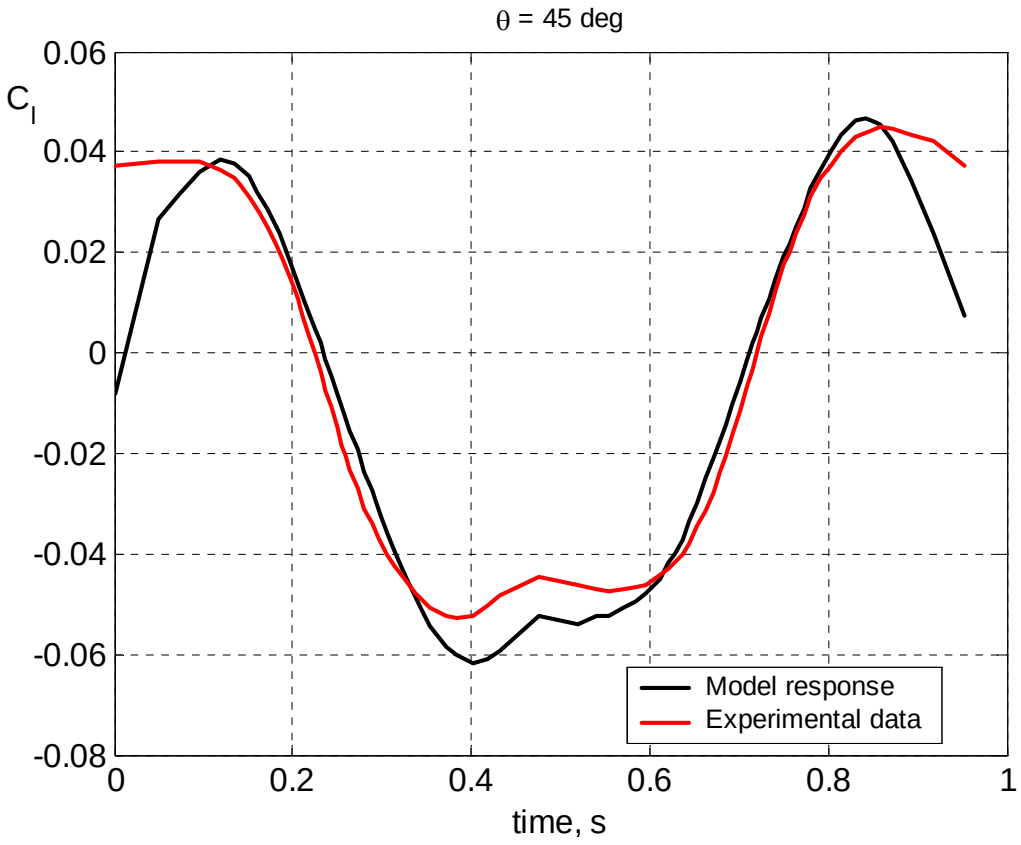

Figure 3-20 Rolling moment coefficient time-history at θ_0 = 45 deg.

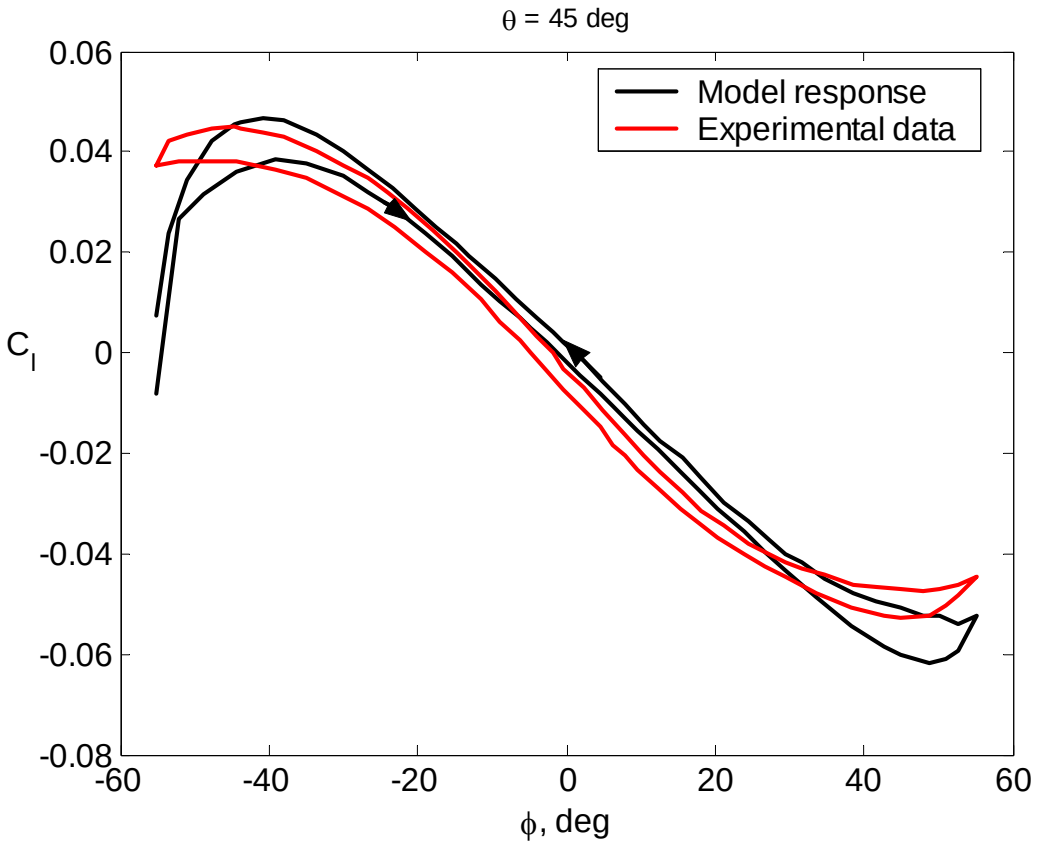

Figure 3-21 Rolling moment coefficient vs. roll angle loops at θ_0 = 45 deg

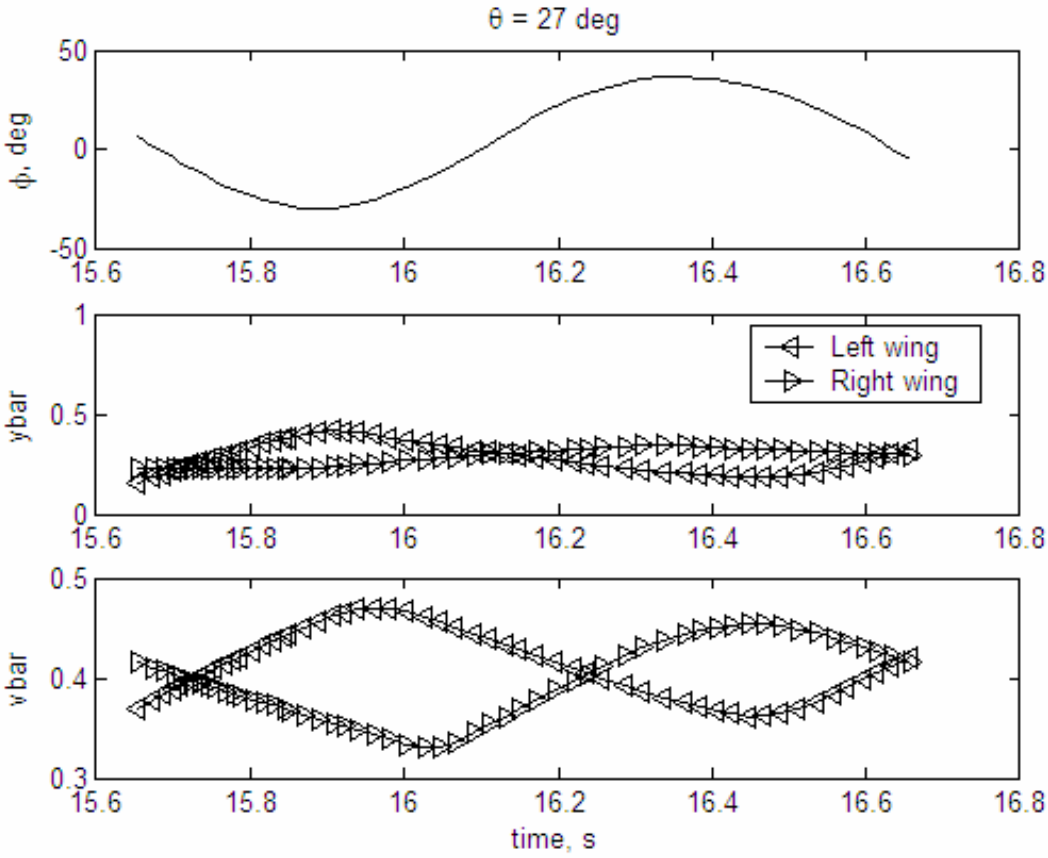

Figure 3-22 Time histories at θ_0 = 27 deg of the internal state variables related to the spanwise and vertical positions of the vortices cores.

Table 3-1 Model parameters for the first investigated model.

i	$\boldsymbol{x_{C_N}(i)}$	$\boldsymbol{x_{C_l}(i)}$	$\boldsymbol{x_{dyn}(i)}$
1	C_{N0}	y_l @ $\phi = 0°$	a_3
2	a_1	y_l @ $\phi = 10°$	b_3
3	b_1	y_l @ $\phi = 20°$	c_3
4	c_1	y_l @ $\phi = 30°$	a_4
5	a_2	y_r @ $\phi = 0°$	b_4
6	b_2	y_r @ $\phi = 10°$	c_4
7	c_2	y_r @ $\phi = 20°$	a_5
8	α_D^* @ $\phi = 0°$	y_r @ $\phi = 30°$	b_5
9	α_D^* @ $\phi = 10°$	-	c_5
10	α_D^* @ $\phi = 20°$	-	τ_1
11	α_D^* @ $\phi = 30°$	-	τ_2
12	α_U^* @ $\phi = 0°$	-	-
13	α_U^* @ $\phi = 10°$	-	-
14	α_U^* @ $\phi = 20°$	-	-
15	α_U^* @ $\phi = 30°$	-	-
16	σ_D @ $\phi = 0°$	-	-
17	σ_D @ $\phi = 10°$	-	-
18	σ_D @ $\phi = 20°$	-	-
19	σ_D @ $\phi = 30°$	-	-
20	σ_U @ $\phi = 0°$	-	-
21	σ_U @ $\phi = 10°$	-	-
22	σ_U @ $\phi = 20°$	-	-
23	σ_U @ $\phi = 30°$	-	-

Table 3-2 Model parameters for the second investigated model.

i	$x_{C_N}(i)$	$x_{C_l}(i)$	$x_{dyn}(i)$
1	C_{N0}	$\phi^*_{y,l,D}$	a_3
2	a_1	$\phi^*_{y,l,U}$	b_3
3	b_1	$\sigma_{y,l,D}$	c_3
4	c_1	$\sigma_{y,l,U}$	a_4
5	a_2	$\phi^*_{y,r,D}$	b_4
6	b_2	$\phi^*_{y,r,U}$	c_4
7	c_2	$\sigma_{y,r,D}$	a_5
8	a_6	$\sigma_{y,r,U}$	b_5
9	b_6	-	c_5
10	c_6	-	a_9
11	a_7	-	b_9
12	b_7	-	c_9
13	c_7	-	a_{10}
14	a_8	-	b_{10}
15	b_8	-	c_{10}
16	c_8	-	a_{11}
17	α^*_D	-	b_{11}
18	α^*_U	-	c_{11}
19	σ_D	-	a_{12}
20	σ_U	-	b_{12}

Table 3-3 Continuation of Table 3-2

i	$x_{C_N}(i)$	$x_{C_l}(i)$	$x_{dyn}(i)$
21	$\phi^*_{v,l,D}$	-	c_{12}
22	$\phi^*_{v,l,U}$	-	$\tau_{1,x}$
23	$\sigma_{v,l,D}$	-	$\tau_{1,y}$
24	$\sigma_{v,l,U}$	-	$\tau_{1,v}$
25	$\phi^*_{v,r,D}$	-	$\tau_{2,\alpha}$
26	$\phi^*_{v,r,U}$	-	$\tau_{2,\phi}$
27	$\sigma_{v,r,D}$	-	
28	$\sigma_{v,r,U}$	-	

Table 3-4 Parameters related to the internal state driving equation location and slope in function of the roll angle for the first investigated model.

ϕ [deg]	α^*	σ
0	1.354	4.775
10	1.465	3.660
20	1.543	3.205
30	1.454	3.724

Table 3-5 Identified values of the second investigated model parameters stored as x_{CN}

i	$x_{C_N}(i)$	θ_0 = 20 deg	θ_0 = 27 deg	θ_0 = 38 deg	θ_0 = 45 deg
1	C_{N0}	2.7404e-002	2.1850e-002	2.1850e-002	2.7404e-002
2	a_1	6.8707e-001	6.8711e-001	6.8711e-001	6.8707e-001
3	b_1	-7.0906e+000	-7.0919e+000	-7.0919e+000	-7.0906e+000
4	c_1	-5.2137 e+000	-5.2155e+000	-5.2155e+000	-5.2137e+000
5	a_2	1.6909 e+000	1.6872e+000	1.6872e+000	1.6909e+000
6	b_2	-3.0125 e+000	-3.0145e+000	-3.0145e+000	-3.0125e+000
7	c_2	2.1221 e+000	2.1195e+000	2.1195e+000	2.1221e+000
8	a_6	-2.6740e-001	-2.2958e-001	-2.2958e-001	-2.6740e-001
9	b_6	-2.6043e-002	5.9983e-002	5.9983e-002	-2.6043e-002
10	c_6	1.4537e-001	1.7257e-001	1.7257e-001	1.4537e-001
11	a_7	8.9613e-003	2.6163e-001	2.6163e-001	8.9613e-003
12	b_7	1.2309e-001	1.1374e-001	1.1374e-001	1.2309e-001
13	c_7	7.9218e-002	7.9529e-002	7.9529e-002	7.9218e-002
14	a_8	1.4662 e+000	9.9747e-002	9.9747e-002	1.4662e+000
15	b_8	4.2017e-002	3.9816e-002	3.9816e-002	4.2017e-002
16	c_8	2.3602e-002	2.4769e-002	2.4769e-002	2.3602e-002
17	α_D^*	1.4160e+000	2.8554e+000	3.3317e+000	2.1722e+000
18	α_U^*	1.4160e+000	2.8554e+000	3.3317e+000	2.1722e+000
19	σ_D	2.0682e+000	1.0377e+001	1.1598e+001	2.8981e+000
20	σ_U	2.0682e+000	1.0377e+001	1.1598e+001	2.8981e+000

Table 3-6 Continuation of Table 3-5.

i	$\boldsymbol{x}_{C_N}(i)$	$\theta_0 = 20$ deg	$\theta_0 = 27$ deg	$\theta_0 = 38$ deg	$\theta_0 = 45$ deg
21	$\phi^*_{v,l,D}$	2.1314e-002	3.1542e-002	2.4476e-002	2.2465e-002
22	$\phi^*_{v,l,U}$	-3.5402e-002	2.6730e-002	3.1913e-002	-3.4784e-002
23	$\sigma_{v,l,D}$	1.4597e+001	6.3498e+000	8.4220e+000	1.6358e+001
24	$\sigma_{v,l,U}$	1.0026e-001	5.9295e+000	7.4075e+000	8.6172e-002
25	$\phi^*_{v,r,D}$	6.1938e-002	2.0780e-001	1.9686e-001	6.0358e-002
26	$\phi^*_{v,r,U}$	5.7646e-002	5.2698e-001	5.6696e-001	5.6214e-002
27	$\sigma_{v,r,D}$	1.3842e+001	3.7205e+000	3.6031e+000	1.5137e+001
28	$\sigma_{v,r,U}$	1.1438e+001	1.5301e+001	1.7665e+001	1.2999e+001

Table 3-7 Identified values of the second investigated model parameters stored as $\boldsymbol{x}_{Cl}$

i	$\boldsymbol{x}_{C_l}(i)$	$\theta_0 = 20$ deg	$\theta_0 = 27$ deg	$\theta_0 = 38$ deg	$\theta_0 = 45$ deg
1	$\phi^*_{y,l,D}$	1.2602e+001	-1.9827e-001	-2.0148e-001	1.2446e+001
2	$\phi^*_{y,l,U}$	1.2602e+001	-1.9827e-001	-2.0148e-001	1.2446e+001
3	$\sigma_{y,l,D}$	-1.2015e+003	-5.3463e+000	-4.4443e+000	-1.2232e+003
4	$\sigma_{y,l,U}$	-7.8353e+000	-1.0263e+001	-5.0803e+000	-7.8896e+000
5	$\phi^*_{y,r,D}$	-1.6449e+003	-2.5374e+002	-2.4108e+002	-1.7883e+003
6	$\phi^*_{y,r,U}$	-1.6449e+003	-2.5374e+002	-2.4108e+002	-1.7883e+003
7	$\sigma_{y,r,D}$	2.8408e-001	4.9048e-003	4.9760e-003	2.6722e-001

8	$\sigma_{y,r,U}$	3.6123e-003	1.3593e-003	1.2434e-003	3.6795e-003

Table 3-8 Identified values of the second investigated model parameters stored as x_{dyn}

i	$x_{dyn}(i)$	$\theta_0 = 20$ deg	$\theta_0 = 27$ deg	$\theta_0 = 38$ deg	$\theta_0 = 45$ deg
1	a_3	-7.1836e-001	-2.6355e+000	-2.3342e+000	-7.2887e-001
2	b_3	-1.7830e+002	-8.3922e+001	-7.7390e+001	-1.7330e+002
3	c_3	-3.5270e+001	-3.5080e+003	-2.2559e+003	-3.7521e+001
4	a_4	2.7081e+002	9.1614e+002	1.3472e+003	2.4691e+002
5	b_4	-2.2916e+003	-3.0140e+004	-3.5954e+004	-4.2587e+003
6	c_4	-1.6381e+003	-3.5130e+003	-4.8785e+003	-1.7617e+003
7	a_5	-4.8981e+002	-2.5102e+001	-1.9191e+001	-1.3918e+002
8	b_5	-1.9642e+003	-3.3407e+002	-2.2134e+002	-2.3841e+003
9	c_5	-3.2078e+002	-5.9000e+003	-3.8720e+003	-3.3461e+002
10	a_9	6.0626e-002	-1.3660e-010	-1.5806e-010	6.3042e-002
11	b_9	-6.9690e-011	-1.3880e-010	-1.5829e-010	-7.2307e-011
12	c_9	-1.0345e-010	-1.2464e-010	-1.1902e-010	-1.1695e-010
13	a_{10}	-1.8674e+001	-1.2404e-010	-1.4855e-010	-1.9274e+001
14	b_{10}	-1.9758e-011	-6.7498e-011	-9.1097e-011	-1.9740e-011
15	c_{10}	-5.7676e-011	-8.6019e-011	-9.4511e-011	-5.9421e-011
16	a_{11}	6.0378e+001	-1.6238e-010	-1.4520e-010	8.0884e+001
17	b_{11}	-5.5131e-011	-1.0544e-010	-9.6867e-011	-5.5152e-011
18	c_{11}	-8.2905e-011	-1.0210e-010	-1.1436e-010	-9.1052e-011
19	a_{12}	3.4144e-002	-1.3602e-010	-1.7319e-010	3.6664e-002
20	b_{12}	-1.3943e-011	-1.5217e-010	-1.8883e-010	-1.6742e-011

Table 3-9 Continuation of Table 3-8

i	$\boldsymbol{x_{dyn}(i)}$	$\theta_0 = 20$ deg	$\theta_0 = 27$ deg	$\theta_0 = 38$ deg	$\theta_0 = 45$ deg
21	c_{12}	-2.8514e-011	-1.3321e-010	-1.3431e-010	-2.7301e-011
22	$\tau_{1,x}$	2.4910e+001	8.8934e+000	9.4968e+000	3.0446e+001
23	$\tau_{1,y}$	2.4684e+003	4.2317e+001	6.8737e+001	6.1722e+003
24	$\tau_{1,v}$	1.3224e+000	1.0958e+002	1.6284e+002	1.1687e+000
25	$\tau_{2,\alpha}$	3.0909e+001	4.4349e+001	8.7504e+000	1.6491e+001
26	$\tau_{2,\phi}$	1.8651e+000	1.2740e+001	1.1641e+001	1.9255e+000

4 Numerical Simulations in Roll

In this Chapter, the single degree of freedom numerical simulation in roll of the slender delta wing shown on Figure 1-22 is carried out using the second proposed unsteady aerodynamic model, defined in Section 2.2.

We start by reducing the set of six degree of freedom rigid body equations of motion in body axes to the simple single degree of freedom pure roll case. Then, we add to the equations of motion the state and output equations of the unsteady aerodynamic model and perform some simulations. The six degree of freedom rigid body equations of motion in body axes are [57]

$$
\begin{aligned}
&\dot{u} + qw - rv + g\sin\theta = X/m \\
&\dot{v} + ru - pw - g\cos\theta\sin\phi = Y/m \\
&\dot{w} + pv - qu - g\cos\theta\cos\phi = Z/m \\
&I_{xx}\dot{p} + \left(I_{zz} - I_{yy}\right)qr + I_{yz}\left(r^2 - q^2\right) + I_{xy}\left(pr - \dot{q}\right) - I_{xz}\left(\dot{r} + pq\right) = L \\
&I_{yy}\dot{q} + \left(I_{xx} - I_{zz}\right)pr + I_{yz}\left(pq - \dot{r}\right) - I_{xy}\left(\dot{p} + qr\right) + I_{xz}\left(p^2 - r^2\right) = M \\
&I_{zz}\dot{r} + \left(I_{yy} - I_{xx}\right)pq + I_{xy}\left(q^2 - p^2\right) - I_{yz}\left(\dot{q} - pr\right) + I_{xz}\left(qr - \dot{p}\right) = N \\
&p = \dot{\phi} - \dot{\psi}\sin\theta \\
&q = \dot{\theta}\cos\phi + \dot{\psi}\cos\theta\sin\phi \\
&r = \dot{\psi}\cos\theta\cos\phi - \dot{\theta}\sin\phi
\end{aligned}
\qquad \textbf{(4-1)}
$$

4.1 Rigid Body Dynamics

The derivation of the six degree of freedom equations of motion for a rigid body can be found in several references, for example [4], [58] and [59]. When in body axes coordinates, they are written as shown in (4-1).

In the case of sting-mounted wind tunnel tests, only the roll degree of freedom is considered. Then, the body axes components of linear velocity *u, v, w,* of angular velocity

q, r, the Euler angles time rates $\dot{\theta}$, $\dot{\psi}$, and their time derivatives are zero. As a consequence, the general aircraft equations of motion (4-1) are reduced to

$$I_{xx}\dot{p} = L \qquad \textbf{(4-2)}$$
$$p = \dot{\phi}$$

which is a two variable state space system. Here, L stands for the rolling moment component in body axes.

4.2 Complete Dynamic System

To describe the complete dynamic system, the rigid body system of equations must be coupled to the unsteady aerodynamic model equations. The aerodynamic model appears in the rigid body equations (4-1) through the rolling moment coefficient in the system (4-2), that is:

$$\dot{p} = \ddot{\phi} = \frac{\overline{q}Sb}{I_{xx}} C_l$$

As described in Chapter 2 for the second proposed aircraft unsteady aerodynamic model, the moment coefficients are obtained by multiplying left and right wing force coefficients by their arms along the corresponding body axis. The complete description of the functional unsteady aerodynamic formulation (4-2) used is in Section 2.2. In order to determine the delta wing motion, equations (4-2) must be coupled to equations (2-13), (2-14), (2-15). The resulting dynamic system built in this way is given by the eight first-order differential equations (4-3)

$$\dot{\phi} = p$$

$$\dot{p} = \frac{\bar{q}Sb}{I_{xx}} C_l$$

$$\tau_{1x} \frac{d\bar{x}_l}{dt} + \bar{x}_l = U_\alpha \bar{x}_{0,U}\left(\alpha_{eff,l}\right) + D_\alpha \bar{x}_{0,D}\left(\alpha_{eff,l}\right)$$

$$\tau_{1x} \frac{d\bar{x}_r}{dt} + \bar{x}_r = U_\alpha \bar{x}_{0,U}\left(\alpha_{eff,r}\right) + D_\alpha \bar{x}_{0,D}\left(\alpha_{eff,r}\right)$$

$$\tau_{1y} \frac{d\bar{y}_l}{dt} + \bar{y}_l = U_\phi \bar{y}_{0,l,U}\left(\phi_{eff}\right) + D_\phi \bar{y}_{0,l,D}\left(\phi_{eff}\right) \qquad \textbf{(4-3)}$$

$$\tau_{1y} \frac{d\bar{y}_r}{dt} + \bar{y}_r = U_\phi \bar{y}_{0,r,U}\left(\phi_{eff}\right) + D_\phi \bar{y}_{0,r,D}\left(\phi_{eff}\right)$$

$$\tau_{1v} \frac{d\bar{v}_l}{dt} + \bar{v}_l = U_\phi \bar{v}_{0,l,U}\left(\phi_{eff}\right) + D_\phi \bar{v}_{0,l,D}\left(\phi_{eff}\right)$$

$$\tau_{1v} \frac{d\bar{v}_r}{dt} + \bar{v}_r = U_\phi \bar{v}_{0,r,U}\left(\phi_{eff}\right) + D_\phi \bar{v}_{0,r,D}\left(\phi_{eff}\right)$$

The dynamic equations (4-3) must be integrated simultaneously to simulate the slender delta wing single degree-of-freedom roll motion. The internal state variables $\bar{x}_i$, $\bar{y}_i$, $\bar{v}_i$ are coupled to the two first equations of motion through the rolling moment coefficient C_l, which is determined by Eq. (2-12), reproduced below for the convenience of the reader:

$$C_l = C_{Nl}\left|\bar{y}_l(\phi)\right| - C_{Nr}\left|\bar{y}_r(\phi)\right| \qquad \textbf{(4-4)}$$

In that equation, the left and right panel normal force coefficients are multiplied by their arms $\bar{y}_i$. The normal force coefficients are calculated from the remaining internal state variables through Eqs. (2-16), (2-29), (2-30), (2-31), and (2-33).

4.3 Results of the Simulations

The slender delta wing used in the simulations is wing 2 of Table 1-1. Nevertheless, since part of the aerodynamic experimental data used to identify the parameters were originally obtained for wing 1, we took the value of its moment of inertia. Therefore, the mixed characteristics of the wing used in the simulations are span $b =$ 0.150 m, root chord $c_r =$ 0.4285 m, sweep angle at the leading edge 80 degrees, and rolling moment of inertia I_{xx} = 9.18 $\times 10^{-2}$ kg m^2. The air density value adopted for the simulations is $\rho = 1.2$ kg/m^3, and the airspeed is $V_T = 9.27$ m/s. The first simulation is done for the wing starting from rest at $\phi_0 = 5$ deg, $\theta_0 = 30$ deg. At these conditions, the wing is expected to exhibit wing rock, and occurs, as Figures 4-1 and 4-2 show. The roll attractor is not located at null roll angle, as expected from wind tunnel tests like the one whose results are shown on Figure 1-12. Also, the amplitude is much smaller in the present simulations. We attribute this and other differences between these simulations and the classical wing rock behavior to the scarcity of the experimental data available to identify the parameters. Figures 4-4 and 4-5 show the results of the simulation starting at $\theta_0 = 30$ deg, $\phi_0 =$ -5 deg, and $\dot{\phi}_0 = 0$ deg/s, and we can see that the roll attractor at $\phi =$ -12 deg is confirmed. To better compare our results to those shown in Figure 1-12, we simulate wing rock with the wing departing from the roll attractor position. This result shows that the build up time is much shorter in the present case. Finally, a simulation is started at $\theta_0 =$ 25 deg, and the results are presented in Figures 4-7 and 4-8. At this pitch angle, wing rock is not supposed to occur. Results show that it does not in the simulations either, but since the area enclosed by the loop in Figure 3-12 is so small, the lateral stability of the wing is found to be practically neutral, and it slowly diverges from the initial position.

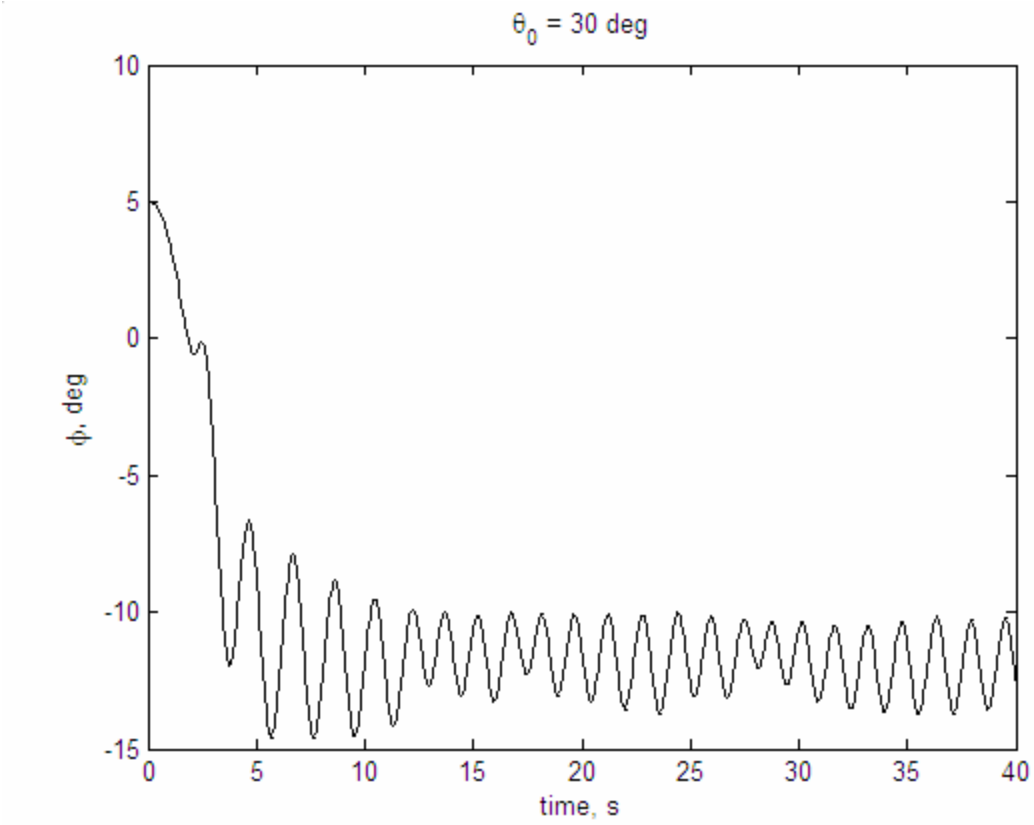

Figure 4-1 Free to roll simulations at wing pitch angle equal 30 deg, starting at roll angle equal 5 degree.

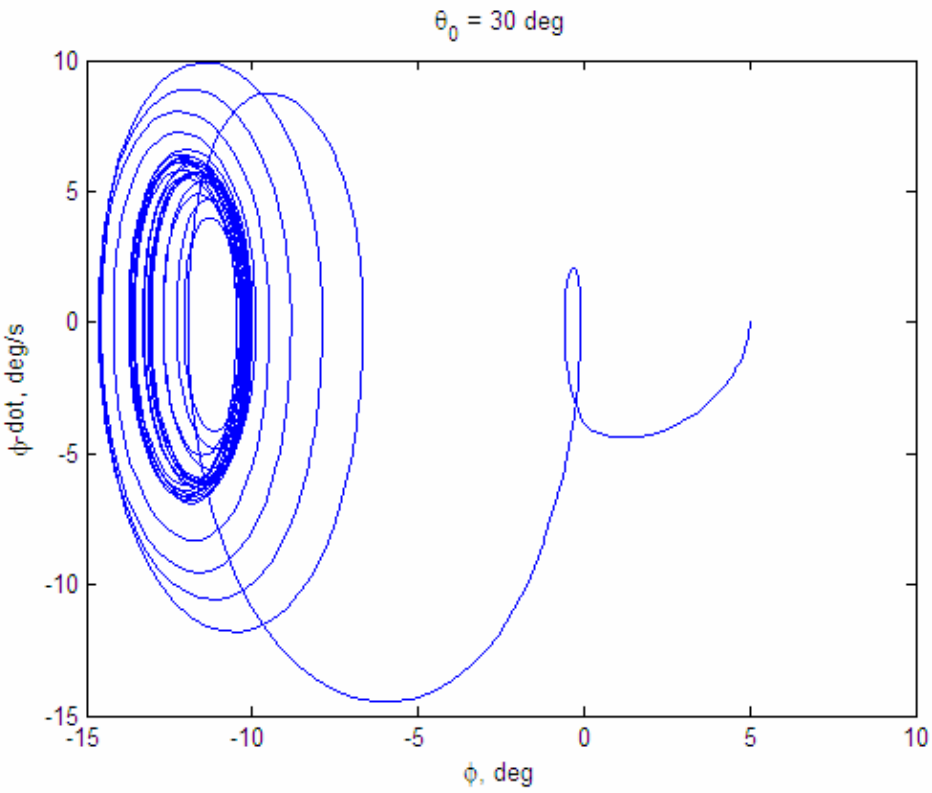

Figure 4-2 Phase-plane of the simulation response at pitch angle equal 30 deg, initial roll angle of 5 degree.

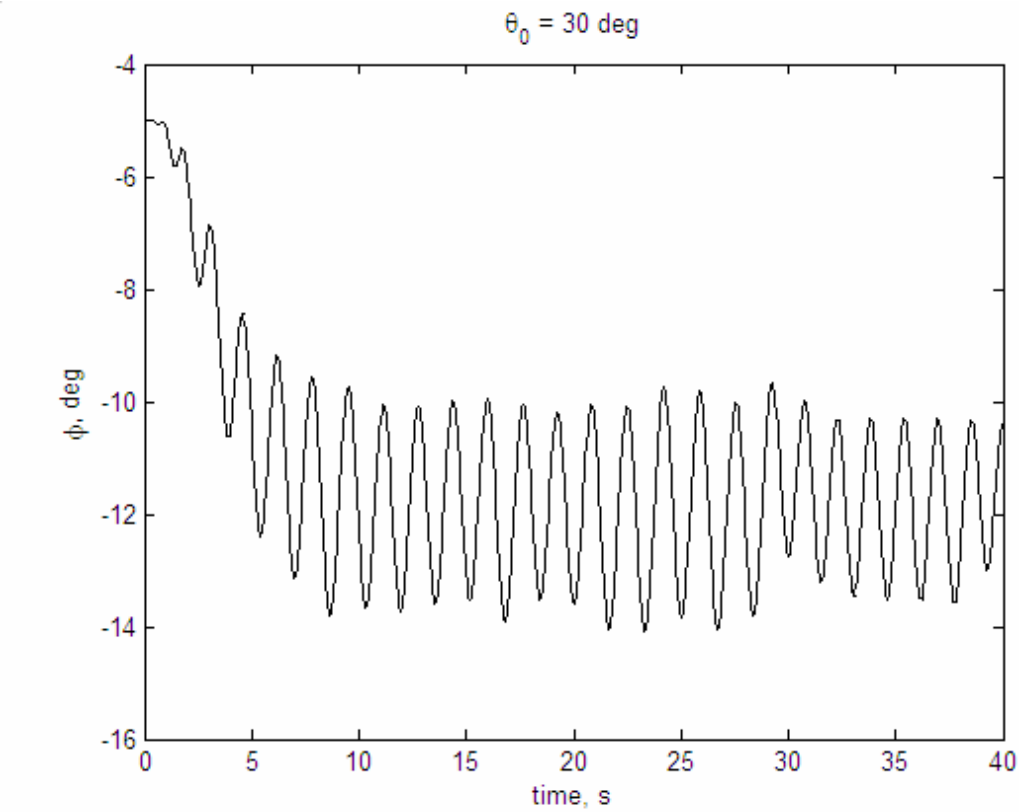

Figure 4-3 Free to roll simulations at wing pitch angle equal 30 deg, starting at roll angle equal -5 degree.

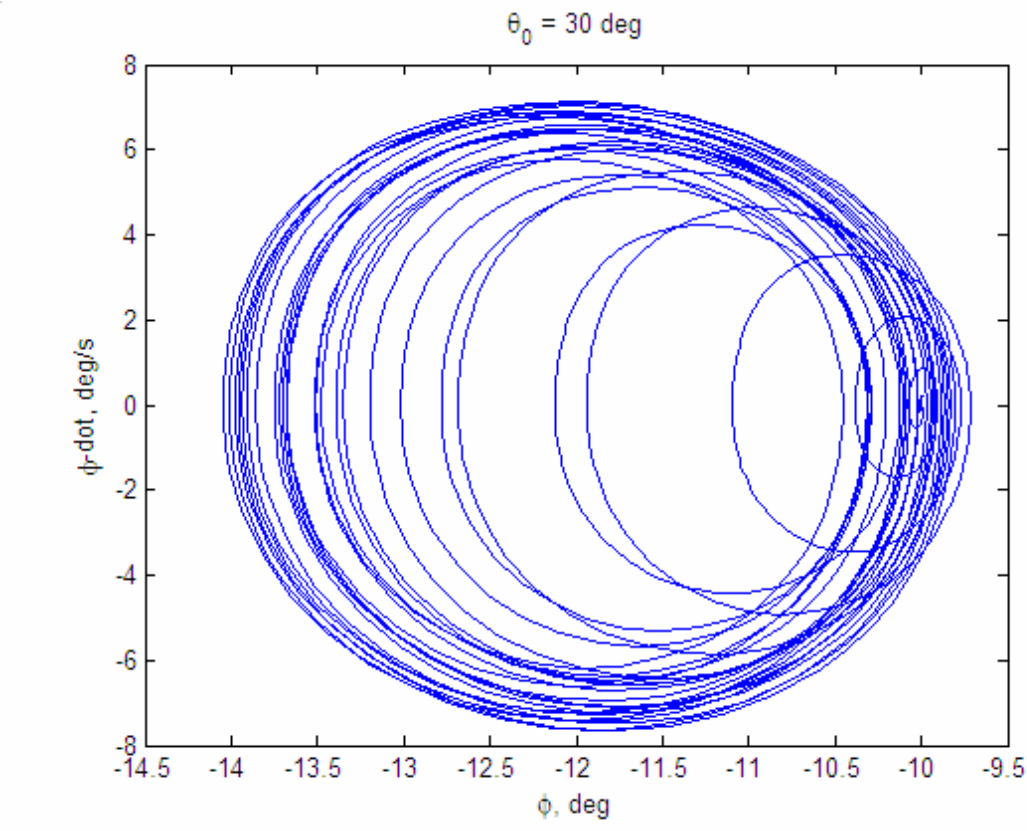

Figure 4-4 Phase-plane of the simulation response at pitch angle equal 30 deg, initial roll angle of -5 degree.

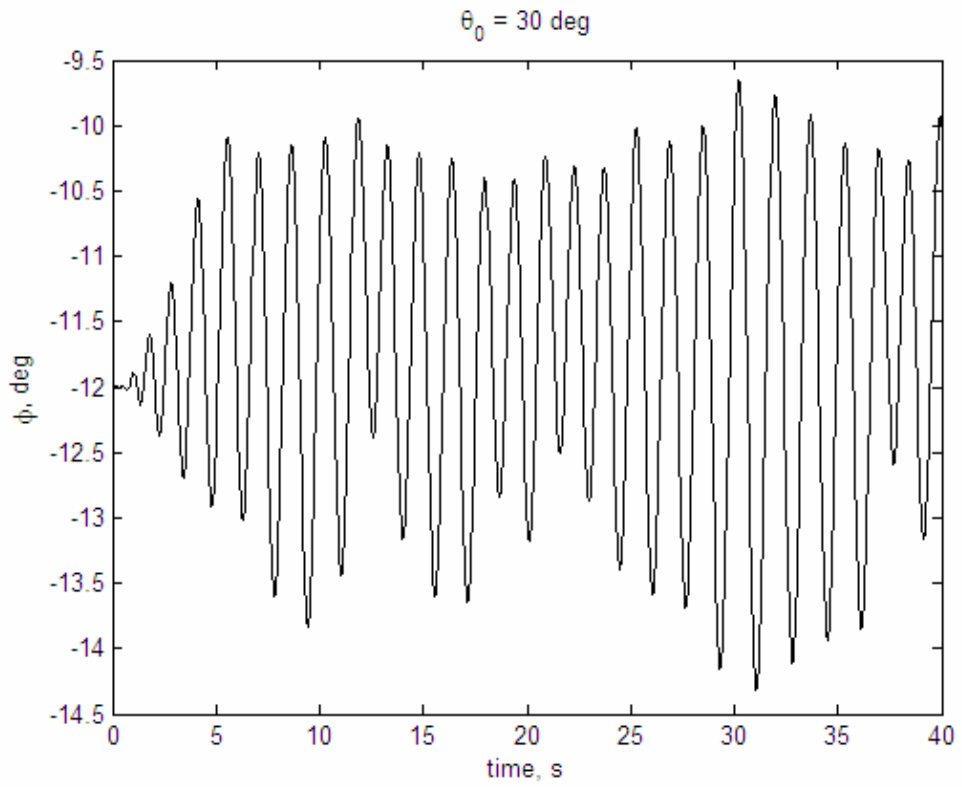

Figure 4-5 Free to roll simulations at wing pitch angle equal 30 deg, starting at roll angle equal -12 degree.

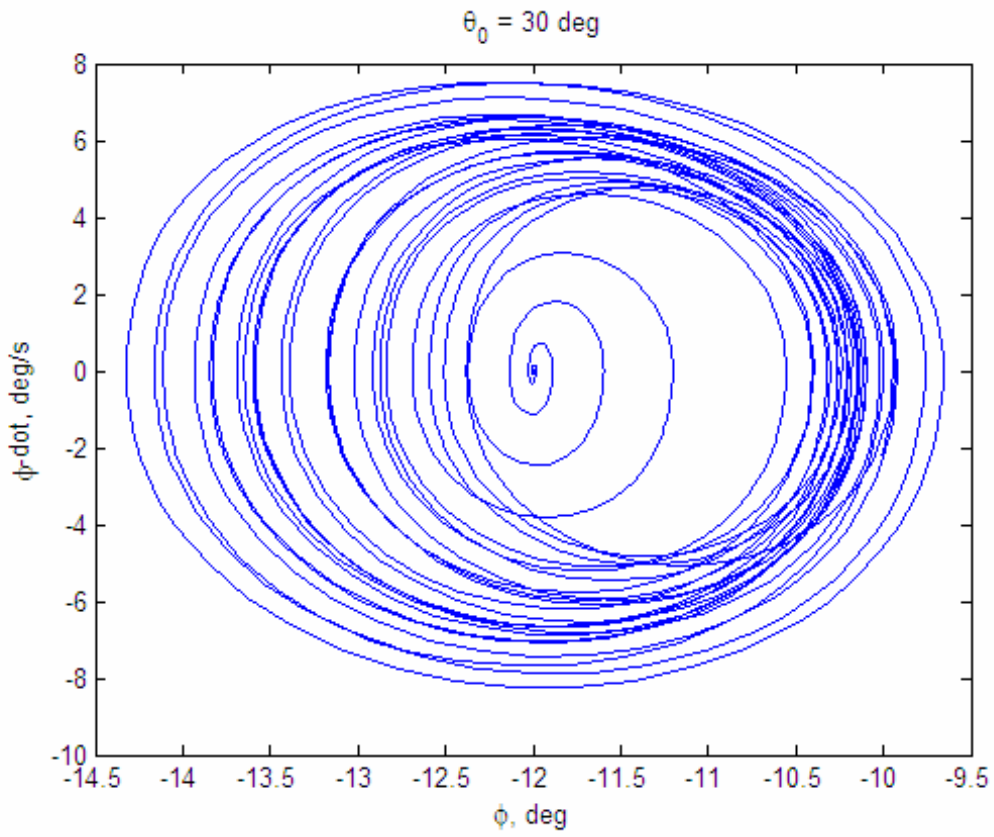

Figure 4-6 Phase-plane of the simulation response at pitch angle equal 30 deg, initial roll angle of -12 degree.

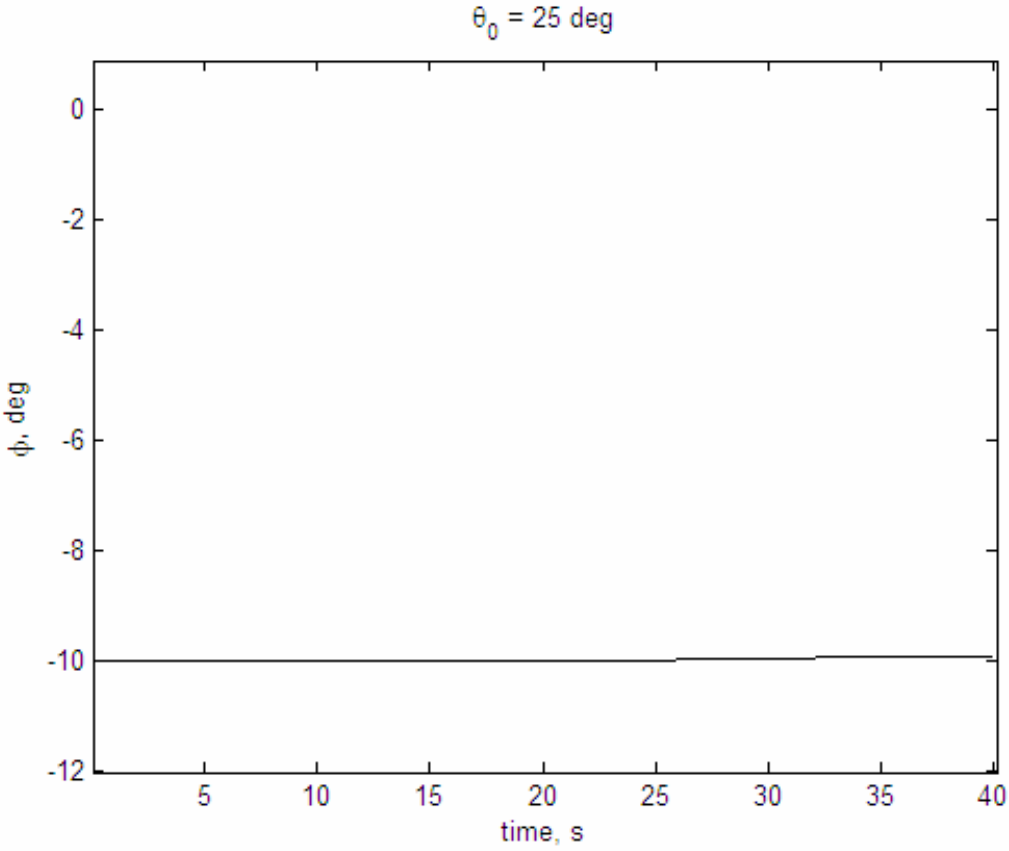

Figure 4-7 Free to roll simulations at wing pitch angle equal 25 deg, starting at roll angle equal -10 degree.

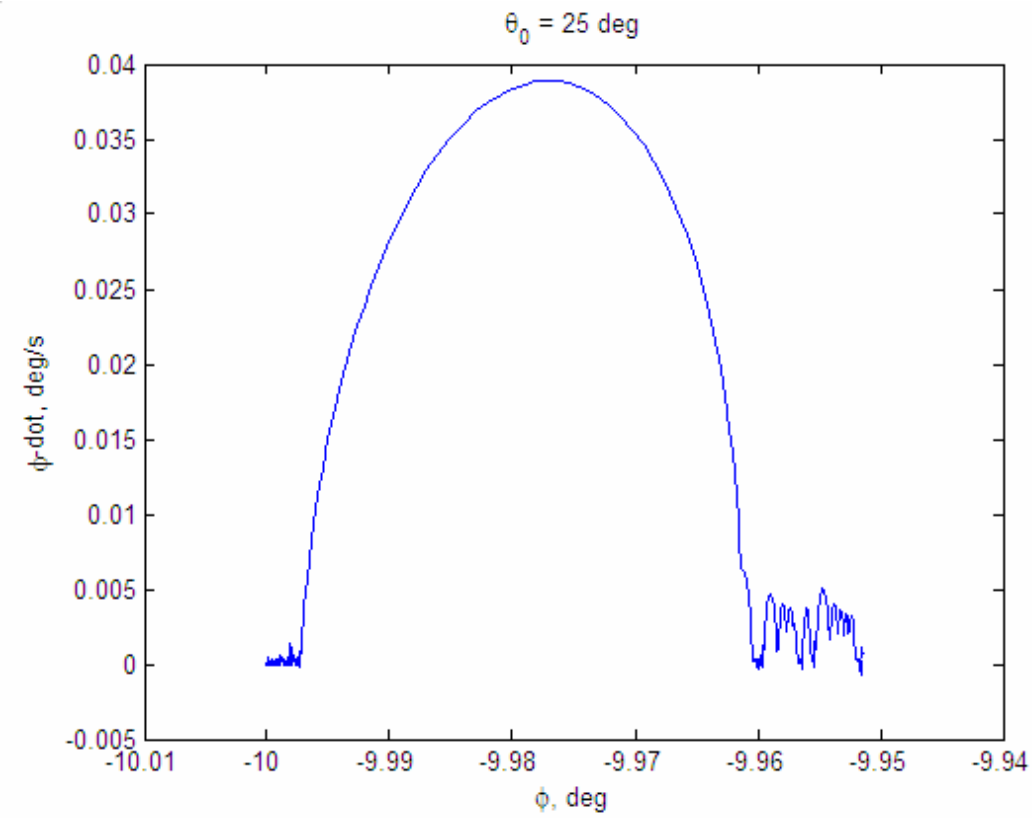

Figure 4-8 Phase-plane of the simulation response at pitch angle equal 25 deg, initial roll angle of -10 degree.

5 Conclusions

Physical models may have a higher computational cost than the functional ones, but their derivation follows a rationale that is dictated by the physical laws that, like a roadmap, lead to a logical result. Otherwise, there are theoretically lots of functional models capable of representing a certain physical phenomenon and this research has shown that the job of figuring out the one that fits can be daunting. Here, the job of finding one dynamic functional model with a state-space formulation that represents wing rock was made a little bit less daunting by following the guidance of physical properties of the flow observed in previous work. As a result, the second proposed and investigated model was shown to be capable of representing wing rock even when used with sparse experimental data. We believe that, with the help of a better set of experimental data, obtained from the wind tunnel or from computational fluid dynamic programs, far better results can be reached.

It is opportune to remember that the slender delta wing configuration simulated here was split into just two panels, and that the simulation is carried out for just one degree of freedom. According to the results shown in Section 4.2, the application of the proposed formulation to this kind of problem gives as a result a dynamic system containing two equations of motion plus six internal state equations for the unsteady aerodynamic model, making a total of eight first-order differential equations to be simultaneously integrated. Notice that, if we had a conventional airplane configuration split into six panels to be simulated in a six degree of freedom motion, the total number of state equations would be thirty.

In system identification, an appropriate model should have the following characteristics:

(a) to reproduce well enough the plant behavior in the range where the data used to identify parameters were gathered;
(b) the parameter identification should be easy;
(c) have good ability for generalization.

Considering these characteristics, the second model investigated can be considered to be promising. Its formulation represents the wing rock phenomenon while allowing good insight into some of the physical properties of the flow. Even though the simultaneous integration of up to thirty state equations can not be considered low-cost computational work, it is lower than the computational cost of any physical method.

As future work in this subject is considered, we suggest the use of a physical numerical method like, for example, the UVLM as a sort of virtual wind tunnel, to get more consistent simulated experimental data to better identify the proposed model.

REFERENCES

[1] Mason, William H., "Stability and Control in Computational Simulations for Conceptual and Preliminary Design: the Past, Today, and Future?", NASA/CP-2004-213028/PT1, *Proceedings of a Symposium held in Hampton, VA*, Sept. 23-25, 2003

[2] Juang, J. N., Kholodar, D., and Dowell, E. H., "System Identification of a Vortex Lattice Aerodynamic Model", NASA TM-2001-211229, October 2001.

[3] Bryan, G. H., *Stability in Aviation*, MacMillan, London, 1911.

[4] Etkin, B., *Dynamics of Flight – Stability and Control*, John Wiley and Sons, Inc., New York, 1959.

[5] Wagner, H., "Uber die Enstehung des dynamishen Auftriebs von Tragflugen, Zangew", *Math. U. Mech*. 5, pp 17-35., 1925

[6] Theodorsen, T., "General Theory of Aerodynamic Instability and the Mechanism of Flutter", NACA TR 496, 1935.

[7] Kussner, H. G., "Zusammenfassender Bericht uber den instationaren Auftrieb von Flugeln", Luftfahrtforschung, Bd. 13, Nr. 12, pp 410-424, Dec. 20, 1936.

[8] Cicala, P., "Sul moto non stazionario di un'ala di alungamento finito", Report No. 107, Laboratorio di Aeronautica, R. Politecnico di Torino, August 1937.

[9] Jones, R. T., "Operational Treatment of the Non-uniform Lift Theory in Airplane Dynamics", NACA TN 667, 1938.

[10] Jones, R. T., “The Unsteady Lift of a Wing of Finite Aspect Ratio”, NACA Rep. 681, June 1939.

[11] Jones, R. T., “The Unsteady Lift of a Finite Wing”, NACA TN 682, Washington, D.C., January 1939.

[12] Jones, R. T., Fehlner, L. F., “Transient Effects of the Wing Wake on the Horizontal Tail”, NACA TN 771, 1940.

[13] Tobak, M., “On the Use of the Indicial Function Concept in the Analysis of Unsteady Motions of Wings and Wing-Tail Combinations”, NACA Report 1188, 1954.

[14] Tobak, M., and Pearson, W. E., “A Study of Nonlinear Longitudinal Dynamic Stability”, NASA TR R-209, September 1964.

[15] Tobak, M., and Schiff, L. B., “On the Formulation of the Aerodynamic Characteristics in Aircraft Dynamics”, NASA TR-R-456, 1976.

[16] Tobak, M., Chapman, G. T., Schiff, L. B., “Mathematical Modeling of the Aerodynamic Characteristics in Flight Dynamics”. NASA TM-85880, Jan. 1984.

[17] Tobak, M., Chapman, G. T., “Nonlinear Problems in Flight Dynamics Involving Aerodynamic Bifurcations”, NASA-TM-86706, March 1985.

[18] Klein, V., and Noderer, K. D., “Modeling of Aircraft Unsteady Aerodynamic Characteristics, Part 1 – Postulated Models”, NASA TM 109120, May 1994.

[19] Klein, V., and Noderer, K. D., "Modeling of Aircraft Unsteady Aerodynamic Characteristics, Part 2 – Parameters Estimated From Wind Tunnel Data", NASA TM 110161, April 1995.

[20] Klein, V., and Noderer, K. D., "Modeling of Aircraft Unsteady Aerodynamic Characteristics, Part 3 – Parameters Estimated From Flight Data", NASA TM 110259, May 1996.

[21] Klein, V., "Modeling of Longitudinal Unsteady Aerodynamics of a Wing-Tail Combination", NASA CR-1999-209547, September 1999.

[22] Reisenthel, P. H., "Development of a Nonlinear Indicial Model for Maneuvering Fighter Aircraft", AIAA Paper 96-0896, 1996.

[23] Reisenthel, P. H., Bettencourt, M. T., "Data-Based Aerodynamic Modeling using Nonlinear Indicial Theory", AIAA Paper 99-0763, 1999.

[24] Reisenthel, P. H., Bettencourt, M. T., "Extraction of Nonlinear Indicial and Critical States Responses from Experimental Data", AIAA Paper 99-0764, 1999.

[25] Levinsky, E. S., "Theory of the Wing Span Loading Instabilities Near Stall", Paper No. 25, AGARD CP 204, *Prediction of Aerodynamic Loading*, 1976.

[26] Hreha, M. A., "A Dynamic Model for Aircraft Post-stall Departure", Ph. D. Dissertation in Aerospace Engineering, *Virginia Polytechnic Institute and State University*, Blacksburg, Virginia, May 1982.

[27] Anderson, M. K., "Aerodynamic Modeling for Global Stability Analysis", AIAA Paper 2002-4805, 2002.

[28] Goman, M. G., Stolyarov, G. I., Tyrtyshnikov, S. L., Usoltev, S. P., and Khrabrov, A. N., "Mathematical Description of Aircraft Longitudinal Aerodynamic Characteristics at High Angles of Attack Accounting for Dynamic Effects of Separated Flow", TsAGI Preprint No. 9, 1990 (in Russian).

[29] Goman, M. and Khrabrov, A., "State-Space Representation of Aerodynamic Characteristics of an Aircraft at High Angles of Attack", *Journal of Aircraft*, Vol. 31, No. 5, pp. 1109-1115, Sept.-Oct., 1994.

[30] Fan, Y., Lutze, F. H., *Identification of an Unsteady Aerodynamic Model at High Angles of Attack*, AIAA Paper 96-3407, 1996.

[31] Abramov, N. B., Goman, M. G., Khrabrov, A. N., Kolinko, K. A., "Simple Wings Unsteady Aerodynamics at High Angles of Attack: Experimental and Modeling Results", AIAA Paper 99-4013, 1999.

[32] De Oliveira Neto, P. J., Lutze, F. H., "First-Order Unsteady Aerodynamic Model that Includes the Static Hysteresis Penomenon", AIAA-2002-4083, Monterey, CA, 2002.

[33] De Oliveira Neto, P. J.; De Almeida, A. R.; Nogueira, S. L.; Verderio, L.; Da Silva, M. G., "G-Jump Simulations for a Fighter Airplane", AIAA-2005-6028, San Francisco, CA, 2005.

[34] Fan, Y., "Identification of an Unsteady Aerodynamic Model up to the High Angle of Attack Regime", *Ph.D. Dissertation in Aerospace Engineering, Virginia Polytechnic Institute and State University*, Blacksburg, VA, 1994.

[35] Myatt, J. H., "Modeling the Rolling 65-Degree Delta Wing with Critical State Encounters", AIAA Paper 97-3646, 1997.

[36] Guicheteau, P., "Bifurcation Theory Applied to the Study of Control Losses on Combat Aircraft", *La Recherche Aerospatiale*, 2, pp. 61-73, 1982.

[37] Durham, W., "AOE 3134 Course Notes and Problems Solutions", Virginia Polytechnic Institute and State University, Blacksburg, VA, 2004.

[38] von Kárman, T., Sears, W. R., "Airfoil Theory for Non-Uniform Motion", *Journal of the Aeronautical Sciences*, 5(10), 1938

[39] Lutze, F. H., Fan, Y. G., Stagg, G., "Multiaxis Unsteady Aerodynamic Characteristcs of an Aircraft", AIAA Paper 99-4011-CP, 1999.

[40] Stagg, G. A., "An Unsteady Aerodynamic Model for Use in the High Angle of Attack Regime", *M. Sc. Thesis in Aerospace and Ocean Engineering, Virginia Polytechnic Institute and State University*, Blacksburg, Virginia, Dec., 1998.

[41] USAF Military Specification, "MIL-S-83691A: Stall/Post-Stall/Spin Flight Test Demonstration Requirements For Airplanes", April 1972

[42] Abzug, M. J., Larrabee, E. E., *Airplane Stability and Control: A History of the Technologies that made Aviation Possible*, Cambridge University Press, New York, NY, 1997

[43] Hwang, C., Pi, W.S., "Some Observations on the Mechanism of Aircraft Wing Rock", *Journal of Aircraft*, 16(6), 1979

[44] Ross, J. A., Beecham, L. J., "An Approximate Analysis of Nonlinear Lateral Motion of a Slender Aircraft (HP115) at Low Speed", ARC&M 3674, 1971.

[45] Nguyen, L. T., Yip L., Chambers J. R., "Self-Induced Wing Rock of Slender Delta Wings", AIAA Paper 81-1883, *AIAA AFM Conference*, Albuquerque, New Mexico, August 1981.

[46] Arena Jr. A., "An Experimental and Computational Investigation of Slender Wings undergoing Wing Rock", *Ph.D. dissertation, University of Notre Dame*, April 1992.

[47] Levin, D., Katz, J., "Dynamic Load Measurements with Delta Wings Undergoing Self-Induced Roll Oscillations", *Journal of Aircraft*, Vol. 21, No. 1, pp. 30-36, 1984.

[48] Ericson, L. E., "The Various Sources or Wing Rock", AIAA Paper 88-4370, August, 1988.

[49] Nguyen, L. T., Whipple, R. D. , and Brandon, J. M., "Recent Experiences of Unsteady Aerodynamic Effects on Aircraft Flight Dynamics at High-Angles-of-Attack", Paper 28, AGARD CP 386, 1985.

[50] Ericson, L. E., "Wing Rock Generated by Forebody Vortices", AIAA Paper 87-0268, 1987.

[51] Arena Jr., A., "An Experimental Study of the Nonlinear Wing Rock Phenomenon", *Master´s Thesis, University of Notre Dame*, April 1990.

[52] Nelson, R. C., Pelletier, A., "The unsteady aerodynamics of slender wings and aircraft undergoing large amplitude maneuvers", *Progress in Aerospace Sciences* 39 (2003) 185-248, Elsevier, 2003.

[53] Konstadinopoulos, P., Mook, D. T., Nayfeh, A. H., "Subsonic Wing Rock of Slender Delta Wings", *Journal of Aircraft*, 22(3), pp. 223-228, March 1985.

[54] Nayfeh, A. H., Elzebda, J. M., Mook, D. T., "Analytical Study of the Subsonic Wing-Rock Phenomenon for Slender Delta Wings", *Journal of Aircraft*, Vol. 6, No. 9, September, 1989.

[55] Saad, A. A., "Simulation and Analysis of Wing Rock Physics for a Generic Fighter Model with Three Degrees-of-Freedom"*, Ph.D. Dissertation, Air Force Institute of Technology*, Dayton, Ohio, 2000.

[56] Lagarias, J.C., J. A. Reeds, M. H. Wright, and P. E. Wright, "Convergence Properties of the Nelder-Mead Simplex Method in Low Dimensions"*, SIAM Journal of Optimization*, Vol. 9 Number 1, pp. 112-147, 1998.

[57] Etkin, B., *Dynamics of Atmospheric Flight*, John Wiley and Sons, Inc. New York, 1972

[58] Gainer, T.G., and Hoffman, S., "Summary of transformation equations and equations of motion used in free flight and wind tunnel data reduction and analysis", NASA-SP-3070, January 1972

[59] Nelson, R. C., *Flight Stability and Automatic Control*, 2nd Edition, Mc Graw-Hill, 1998

[60] Durham, W., "AOE 5214 Course Notes and Problems Solutions", Virginia Polytechnic Institute and State University, Blacksburg, VA, 1997.

Appendices

Appendix A

A.1 The Convolution Integral Theorem

Also called the Superposition Theorem or Duhamel's integral theorem [57].

Let $X_1(s)$ to be the Laplace transform of $x_1(t)$, and $X_2(s)$ be the transform of $x_2(t)$. Then the function $x_3(t)$ whose transform is the product $X_3(s) = X_1(s)X_2(s)$ is

$$x_3(t) = \int_{\tau=0}^{t} x_1(\tau)\, x_2(t-\tau)\, d\tau$$

The theorem of this section helps with the calculation of transient responses of linear systems to complicated forcing functions. The general response appears as the superposition of responses to a sequence of steps or impulses that represent the actual forcing function.

A.2 Angle of attack and sideslip variation during rolling motion at fixed pitch angle

In a wind tunnel working in steady state conditions, the free stream velocity vector is constant and horizontal. We therefore choose the *X* axis of the local horizontal reference system to be coincident with the velocity vector. When the airplane model rolls around the sting, the effective angle of attack $\alpha(t)$ and sideslip $\beta(t)$ in a given time *t* are related to the model roll angle $\phi(t)$ at that moment.

The definitions for the angle of attack and sideslip angle as a function of the body-axes components *u*, *v*, and *w* of the air velocity are [57], [59], [60]:

$$\alpha(t) = \tan^{-1}\frac{w}{u} \tag{A.2-1}$$

$$\beta(t) = sin^{-1}\frac{v}{V} = sin^{-1}\frac{v}{\sqrt{u^2+v^2+w^2}} \tag{A.2-2}$$

The *u*, *v*, and *w* velocity body-axes components can be related to the air velocity through a local horizontal to the body axis reference systems transformation matrix $T_{B,H}$, such that, in the particular case where the heading angle ψ is zero, we have

$$\begin{Bmatrix} u \\ v \\ w \end{Bmatrix} = T_{B,H}\begin{Bmatrix} V \\ 0 \\ 0 \end{Bmatrix} \tag{A.2-3}$$

$$T_{B,H} = \begin{bmatrix} 1 & 0 & 0 \\ 0 & \cos\phi(t) & \sin\phi(t) \\ 0 & -\sin\phi(t) & \cos\phi(t) \end{bmatrix}\begin{bmatrix} \cos\theta_0 & 0 & -\sin\theta_0 \\ 0 & 1 & 0 \\ \sin\theta_0 & 0 & \cos\theta_0 \end{bmatrix}$$

$$= \begin{bmatrix} \cos\theta_0 & 0 & -\sin\theta_0 \\ \sin\theta_0\sin\phi(t) & \cos\phi(t) & \cos\theta_0\sin\phi(t) \\ \sin\theta_0\cos\phi(t) & -\sin\phi(t) & \cos\theta_0\cos\phi(t) \end{bmatrix} \tag{A.2-4}$$

Therefore,

$$u = V\cos\theta_0$$
$$v = V sin\theta_0 sin\phi$$
$$w = V sin\theta_0 \cos\phi \qquad \text{(A.2-5)}$$

Substituting the Eqs. (A.2-5) into the definitions (A.2-1) and (A.2-2), we get

$$\alpha(t) = \tan^{-1}\left[\tan\theta_0 \cos\phi(t)\right]$$
$$\beta(t) = \sin^{-1}\left[\sin\theta_0 \sin\phi(t)\right] \qquad \text{(A.2-6)}$$

Figure A.2-1 shows the variations of $\alpha(t)$ and $\beta(t)$ with $\phi(t)$ for $\theta_0 = 20°$. At $\phi = 0°$, the model sideslip angle is zero, and its angle of attack is equal θ_0. As the roll angle grows from 0 to 90 degree, the model angle of attack is reduced to zero and its sideslip angle grows to the value of the pitch angle.

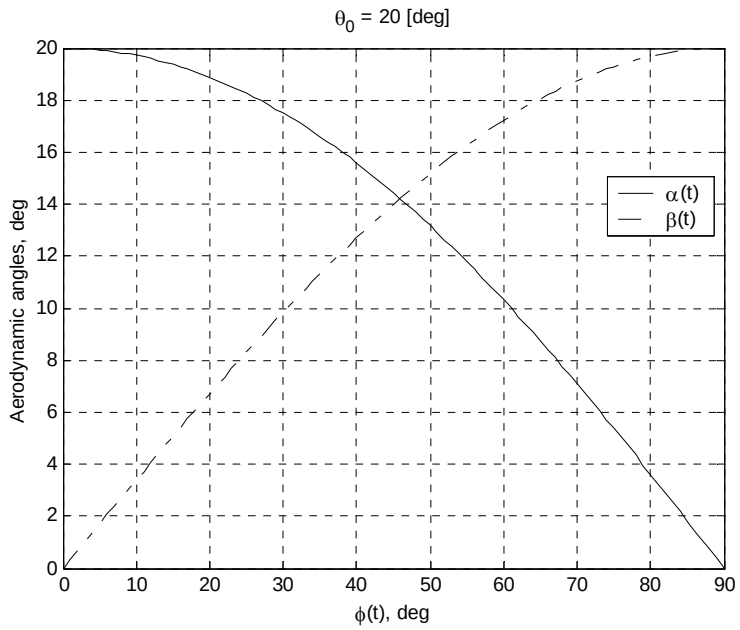

Fig. A.2-1 Variation of the aerodynamic angles with the roll angle for a pure rolling motion in wind tunnel for pitch angle equal 20 deg.

Vita

Pedro Jose de Oliveira Neto was born on February 3rd, 1957 in the small town of Igarapava - SP, in Brazil. He is the oldest of the three children that Adauto and Laudelina de Oliveira brought to this world where they no longer live. Since about that time, he has been fascinated with vehicles, are they traveling in land, sea, air or outer space. This fascination led him to his Mechanical Engineering B.S. graduation at the Sao Paulo State University (UNESP), at the Guaratingueta Campus. It also led him to his airplane and glider pilot licenses. Trying to understand better how these wonderful machines are conceived, in 1981 he got an internship at the Institute of Aeronautics and Space (IAE), in Sao Jose dos Campos – SP. Next year, this internship became a full-time job in which he works since then. As a part of his quest for information, in 1982 he also joined the *Ecole Nationale Superieure de L'Aeronautique et de L'Espace* (ENSAE) in Toulouse, France, where in 1983 he got a Master of Engineering equivalent degree. Trying to understand how better the aircrafts can be operated, in December of 1996 he got his Master of Science degree in Flight Dynamics at the Aeronautics Institute of Technology (ITA), in Sao Jose dos Campos. Trying to know better how to predict and simulate the behavior of the aircrafts, he joined the Flight Dynamics Group at Virginia Tech, where at that time people were concerned about traveling to the "left side of the dog's house". Upon receiving his Ph.D. degree in Aerospace in the Fall term of 2007, he will go back to his work at the Aerodynamics Division of the IAE, in the Aerospace Technology General Command (CTA). At that time, he is married to Maria, has two children and one grandchild.